Interaction Notes

Note 117

SURFACE CURRENT AND SURFACE CHARGE DENSITY INDUCED ON AIRCRAFT MODELS

June 1972

R.R. Lentz, P.H. Pathak and W.D. Burnside
The Ohio State University ElectroScience Laboratory
Department of Electrical Engineering
Columbus, Ohio 43212

Abstract

Geometrical optics, physical optics, the geometrical theory of diffraction and eigenfunction solutions are used to compute the surface charge and surface current densities induced on aircraft-like structures by high frequency incident plane waves. Recent advances in diffraction theory, which are applicable to the problem at hand, are also discussed.

The applicability of these techniques to aircraft-like geometries is demonstrated by comparing calculated with measured results. The use of physical optics alone to calculate the surface charge densities is investigated.

SURFACE CURRENT AND SURFACE CHARGE DENSITY INDUCED ON AIRCRAFT MODELS

I. INTRODUCTION

The purpose of this report is to review some of the recent work done at the ElectroScience Laboratory concerning radiation pattern calculations of antennas mounted on aircraft-like structures, with a view towards using these approaches to find the surface current and charge density induced on an aircraft illuminated by an incident electromagnetic wave, for frequencies above those for which integral equation solutions are applicable. In particular, this work deals with the problem of determining the fields on the surface of perfectly conducting structures such as finite or infinite length cylinders of convex cross sections, convex curved surfaces, finite wedge geometries, and finite plates, since one can model an aircraft approximately by a suitable combination of finite cylinders, cones, plates, etc. Electromagnetic boundary value problems do not lend themselves to exact analytical solutions except in a few cases wherein the geometrical configuration of the problem conforms to one of the six coordinate systems in which the vector wave equation is separable, or for a very limited number of special geometries which can be treated by function theoretic methods. Furthermore, accurate numerical results can be obtained from the numerical solution of the pertinent integral equation if the radiating structure is sufficiently small in terms of wavelength; therefore it is often necessary to employ approximate analytical techniques for aircraft-like geometries at higher frequencies. Some of the well known approximate analytical techniques are those of geometrical optics, geometrical theory of diffraction (GTD), physical optics, variational procedures and perturbation procedures. The GTD is a relatively recent development by Keller and his co-workers[1]. Geometrical optics, when used in conjunction with GTD, constitutes the

ray optical technique; this technique has been found extremely valuable for analyzing many electromagnetic radiation and diffraction problems involving practical structures which are sufficiently large in terms of a wavelength[2,3,4,5]. The ray optical technique allows one to "build-up" a solution to the problem of computing patterns of antennas located on aircraft, using the known solutions to the individual parts of the model approximating the aircraft structure. Furthermore, the ray optical technique complements the modal or numerical techniques of analysis which are useful for geometries sufficiently small in terms of a wavelength. This report concerns itself primarily with the ray optical technique which is chosen for the theoretical analysis involved. Section II of this report summarizes the ray-optical technique and its applications to certain problems of importance to the radiation pattern calculations for on-aircraft antennas.

Section III deals with the analysis for calculating the fields on the surface of aircraft models, and presents calculated results along with the measured patterns for comparison. The measured results are seen to agree well with the calculated results. Section IV indicates some of the latest analytical techniques which constitute extensions to the GTD. These techniques although applicable to the problem discussed in Section III are not incorporated therein, as these latest methods were not available until after the computations and measurements discussed in Section III were completed. In Section III, chiefly the ray-optical procedure and modal analysis are used; however, in at least one instance, the physical optics approximation is applied in conjunction with the ray-optical technique to expedite the analysis.

Since the problem of interest is the determination of surface current and charge density induced on an aircraft illuminated by an incident electromagnetic wave, it is interesting to see the manner in which this problem is related to the radiation pattern calculation

of antennas mounted on the same aircraft. Frequently these patterns are available, and they may be used to deduce the current distribution. The Reciprocity Theorem[6] in electromagnetic theory serves to relate these two problems in the following manner. As a consequence of the reciprocity principle, the electric surface current density induced on the aircraft surface (assumed to be perfectly conducting) may be determined from the radiation patterns of two mutually orthogonal (spatially) infinitesimal magnetic current moments, located tangentially on the aircraft surface, at the point where the induced current density is desired. The field point in the radiation problem is associated with the direction of the given incident electromagnetic wave which illuminates the aircraft (the infinitesimal current moments radiate at the same frequency as that of the incident wave). Employing the reciprocity argument, the electric charge density induced at any point on the aircraft surface is similarly obtained from the radiation pattern of an infinitesimal electric current moment located at the point where the induced charge density is desired; the electric current moment being oriented along the normal to the surface at that point. In practice, such infinitesimal electric and magnetic current moments may be approximated in the following way. The equivalent source for a thin slot whose dimensions are negligible (infinitesimally small) compared to a wavelength and to the dimensions of the structure which contains the slot, is an infinitesimal magnetic current moment oriented along the slot axis. The equivalent source is assumed to be located at the geometric center of the small, thin slot. Similarly, a short monopole on a conducting surface may be replaced by an equivalent source consisting of an infinitesimal electric current moment normal to the surface at the same location.*

*Alternately, any of the probes described elsewhere in the interaction notes would represent either electric or magnetic current moments which are designed for the explicit purpose of monitoring the surface charge or current density respectively.

Hence, the type of on-aircraft antennas that we will be concerned with are primarily the thin slot of a sufficiently small size, and the short monopole.

Furthermore experience has shown that the value of the electric current density in the illuminated region for a plane wave normally incident on a cylinder is approximately $2\hat{n} \times \overline{H}^i$ to a high degree of accuracy for the range of radii for which optical approximations are applicable ($\frac{a}{\lambda} > 1$). The magnitude of the ripple present in the pattern is indicative of the magnitude of the error in the physical optics assumption. A thin longitudinal slot responds to the longitudinal component of the magnetic field intensity and the corresponding surface current density $\overline{J}$ is given by $\overline{J} = \hat{n} \times \overline{H}^t$ where $\overline{H}^t$ is the total magnetic field intensity. Thus given the pattern of such a slot on the surface, the value at the pattern maximum is approximately $\overline{J} = 2\hat{n} \times \overline{H}^i$ and the value for any other angle of incidence is directly proportional to the pattern level of that slot. The approximation improves as frequency increases. Similarly the axial slot pattern can be used to obtain the longitudinal component of current density. A similar, assertion can be made relating the "physical optics response" ($\rho = 2\varepsilon_0 \hat{n} \cdot E^i$) to the surface charge density.

II. A SUMMARY OF THE RAY-OPTICAL METHOD

The ray optical technique for analyzing antenna and scattering problems consists of describing the radiated or scattered fields in terms of the conventional geometrical optics rays together with the diffracted rays predicted by the Geometrical Theory of Diffraction (GTD). GTD was introduced by Keller[1] as a systematic extension of classical geometrical optics to describe the diffraction phenomenon in terms of rays. GTD postulates the existence of diffracted rays to describe the diffracted fields in a manner similar to that of classical geometrical optics, in which the geometrical optics rays

are utilized to describe the incident, reflected, and refracted fields. The ray optical technique is valid at high frequencies[7], so that the radiated and scattered fields at sufficiently high frequencies can be adequately described in terms of rays. However, in a number of cases the ray optical solution is surprisingly accurate even for lower frequencies. The main advantages of the ray-optical technique are that:

a) it is simple to use, and yields accurate results;
b) it provides some physical insight into the radiation and scattering mechanisms involved; and
c) it can be used to treat problems for which exact analytical solutions are not available.

The discussion to follow outlines the methods of geometrical optics, and the geometrical theory of diffraction. These are also referred to as asymptotic high-frequency methods. Kouyoumjian[7] reviews these ray techniques in the context of asymptotic high frequency approximations. In this report, Reference [7] serves as a guideline for describing the geometrical optics and GTD techniques.

A. Geometrical Optics

In the geometrical optics description of electromagnetic wave propagation, the energy travels along paths defined by rays. The ray paths obey Fermat's Principle which states that the energy flux propagates from point A to point B along a ray, in a medium of refractive index, n such that

$$\int_A^B n\,ds \qquad (ds = \text{incremental path length})$$

is an extremum. In variational notation, Fermat's Principle is stated as

$$(1) \qquad \delta \int_A^B n(s)\, ds = 0.$$

Thus, in a lossless, homogeneous, isotropic medium the energy travels along ray paths which are straight lines. The field intensity along the ray is governed by the conservation of energy flux in an astigmatic ray bundle indicated in Fig. 1. A^2 and A_o^2 respectively represent

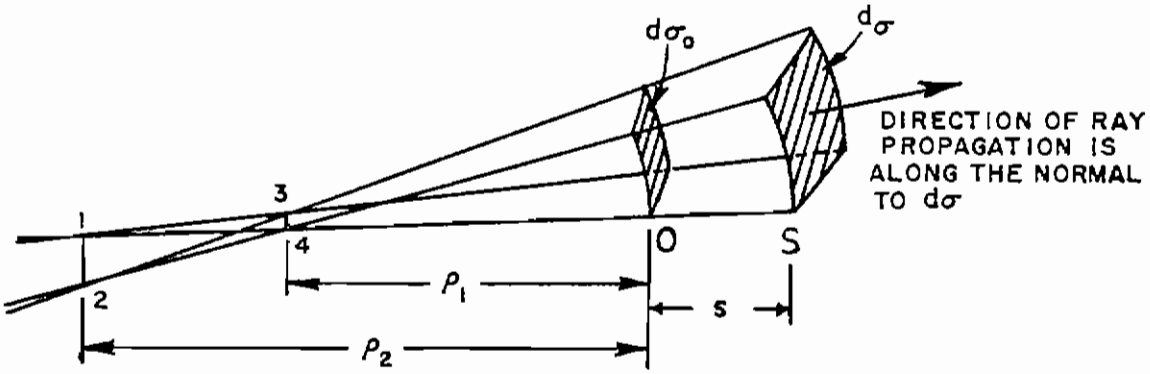

Fig. 1. Ray tube geometry.

the field intensity at S and 0; $d\sigma$ and $d\sigma_o$ are the cross sectional areas of the ray bundle at S and 0 respectively. Conservation of energy in the ray bundle requires that $A^2\, d\sigma = A_o^2\, d\sigma_o$, so that,

$$(2) \qquad \frac{A}{A_o} = \sqrt{\frac{\rho_1\, \rho_2}{(\rho_1+s)(\rho_2+s)}} \equiv F(s)$$

F(s) is viewed as an energy spreading factor associated with the ray path from 0 to S.

According to the geometrical optics description, the electric field intensity along the ray path may be expressed as

(3) $$\bar{E}(S) \sim \bar{E}(0)\, e^{-jk\phi}\, F(s)\, e^{-jks},$$

where $\bar{E}(0)\, e^{-jk\phi}$

is the field intensity at the reference plane at 0, F(s) is the spatial attenuation of the field along the ray path from 0 to S as indicated earlier, and e^{-jks} is the phase variation along the ray path (for an $e^{j\omega t}$ time dependence), where k is the wave number of the medium. $\bar{E}(S)$ is polarized normal to the ray path in the ray optics approximation. Reference [7] indicates that Eq. (3) corresponds to the wave equation, thereby directly implying the high frequency nature of the geometrical optics approximation. When $s = -\rho_1$ or $s = -\rho_2$, the electric field becomes infinite and the geometrical optics description breaks down; these positions $s = -\rho_1$, and $s = -\rho_2$ are the caustic locations. The caustics are shown by lines 1-2 and 3-4 respectively; these caustics occur whenever a congruence of rays is present. Upon propagating through a caustic the sign of $(\rho+s)$ changes and a phase jump of $e^{j\pi/2}$ results.

(4) $$\frac{1}{\sqrt{\rho+s}} = \left|\frac{1}{\sqrt{\rho+s}}\right| e^{+j\pi/2}$$

The geometrical optics description is valid on either side of the caustic, and the field at the caustic may be deduced from separate considerations[8,9].

When a ray is incident on a boundary surface, it is transformed into reflected and transmitted (refracted) rays, and the reflected and transmitted rays may be found according to laws of reflection and refraction . For a perfectly conducting boundary

there is no transmission involved, and only reflected rays are present. Consider a point source at P' near a smooth, perfectly conducting obstacle as shown in Fig. 2. An incident ray from P' reaches a point

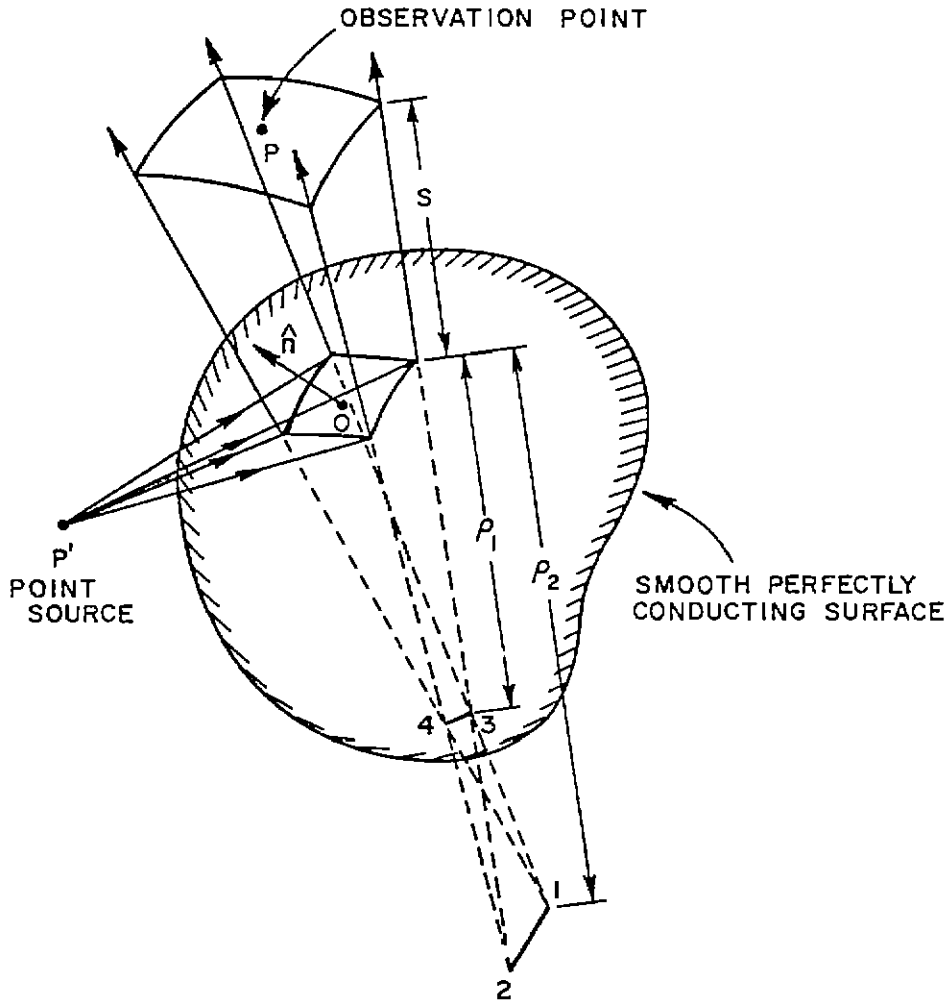

Fig. 2. Reflection from a smooth perfectly conducting surface.

O on the obstacle wherefrom it is reflected. The reflected ray reaches an observation point P along the path P'OP. Let $\hat{n}$ be a unit normal vector to the surface at O, and let $\hat{I}$ and $\hat{S}$" represent the incident

ray direction along P'O, and the direction of the reflected ray along OP, respectively. The path P'OP is governed by Fermat's principle which implies that the following condition is true

$$(5) \qquad -\hat{n} \cdot \hat{I} = \hat{n} \cdot \hat{S}'' \quad \text{(law of reflection)}.$$

Next, one may define the plane of incidence as one which contains the unit vectors $\hat{I}$ and $\hat{n}$. Let $\hat{\beta}_i$ and $\hat{\phi}_i$ be unit vectors shown in Fig. 3 which lie in the plane of incidence and perpendicular to the

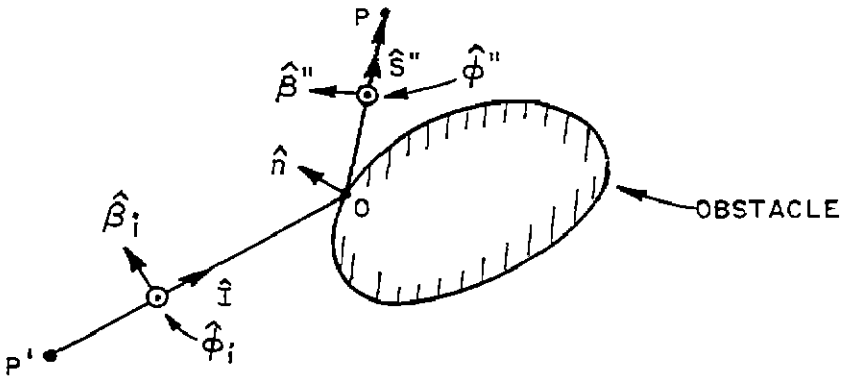

Fig. 3. Unit vectors for scattering by perfectly conducting body.

plane of incidence, respectively. These unit vectors satisfy the following relationships

$$(6) \qquad \hat{\beta}_i \cdot \hat{I} = 0 \quad , \quad \text{and} \quad \hat{\phi}_i = \hat{I} \times \hat{\beta}_i \ .$$

One may similarly define the plane of reflection as one which contains $\hat{n}$ and $\hat{S}''$. The planes of incidence and reflection are the same (also a consequence of Fermat's principle). Thus,

$$(7) \qquad \hat{\phi}_i = \hat{I} \times \hat{\beta}_i = \hat{S}'' \times \hat{\beta}'',$$

where $\hat{\beta}''$ is a unit vector in the plane of reflection such that

(8) $\hat{S}'' \cdot \hat{\beta}'' = 0.$

The unit vector $\hat{\phi}''$ is identical to $\hat{\phi}_i$ defined in Eq. (6). In particular,

(9) $\hat{\phi}'' = \hat{S}'' \times \hat{\beta}'' \ (= \hat{\phi}_i).$

All of the unit vectors discussed above are indicated in Fig. 3. The rays at P may be projected backwards till they intersect; this results in the formation of the virtual caustics indicated by the lines 1-2 and 3-4 in Fig. 2. Thus, the field at P appears to emanate from the virtual caustics at 1-2, and 3-4; this description provides the familiar astigmatic ray bundle whose geometry was indicated in Fig. 1. Following Eq. (3), the geometrical optics representation for $\bar{E}^r(P)$ which is the reflected at P is,

(10) $\bar{E}^r(P) \sim \bar{E}^i(0) \cdot \bar{\bar{R}}\, F(s)\, e^{-jks}$

where $\bar{E}^r(0)$ is the reflected field at 0 (corresponding to $\bar{E}(0)\, e^{jk\phi}$ of Eq. (3)) and equals $\bar{E}^i(0) \cdot \bar{\bar{R}}$, where $\bar{E}^i(0)$ is the field incident at 0 from the source at P', and $\bar{\bar{R}}$ is the dyadic reflection coefficient which serves as a transfer function relating the reflected field to the incident field. One may decompose $\bar{E}^i(0)$ into components along $\hat{\beta}_i$ and $\hat{\phi}_i$ (since $\bar{E}^i \cdot \hat{I} = 0$ in the ray optical approximation). Hence,

(11) $\bar{E}^i(0) = (\hat{\beta}_i\, \hat{\beta}_i + \hat{\phi}_i\, \hat{\phi}_i) \cdot \bar{E}^i(0).$

Similarly, one may decompose the reflected field along $\hat{\beta}''$ and $\hat{\phi}''$. Therefore,

(12) $\bar{E}^r(P) = (\hat{\beta}''\, \hat{\beta}'' + \hat{\phi}''\, \hat{\phi}'') \cdot \bar{E}^r(P).$

It follows from Eq. (11) and Eq. (12) that the dyadic reflection coefficient may be written as

$$(13) \qquad \bar{\bar{R}} = R_1\, \hat{\beta}_i\, \hat{\beta}'' + R_2\, \hat{\beta}_i\, \hat{\phi}'' + R_3\, \hat{\phi}_i\, \hat{\beta}'' + R_4\, \hat{\phi}_i\, \hat{\phi}''.$$

The components R_1, R_2, R_3 and R_4 are determined by enforcing the proper boundary condition on $(\bar{E}^i + \bar{E}^r)$ at 0. For a perfectly conducting scatterer, $\hat{n} \times (\bar{E}^i + \bar{E}^r)\big|_{\text{at } 0} = 0$ so that $R_2 = 0$, $R_3 = 0$, and $R_1 = 1$, whereas $R_4 = -1$. The reflected field $\bar{E}^r(P)$ can thus be explicitly written in terms of the field incident on the perfectly conducting surface at 0 as

$$(14) \qquad \bar{E}^r(P) \sim \bar{E}^i(0) \cdot \{\hat{\beta}_i\hat{\beta}'' - \hat{\phi}_i\hat{\phi}''\} \sqrt{\frac{\rho_1\rho_2}{(\rho_1+s)(\rho_2+s)}}\, e^{-jks}$$

The distances ρ_1 and ρ_2 in the expression for F(S) are given by the following relations

$$(15) \qquad \frac{1}{\rho_1} = \frac{1}{P'0} \pm \frac{2}{R_1 \cos\psi_0} \qquad \text{+ sign for convex surfaces}$$

$$(16) \qquad \frac{1}{\rho_2} = \frac{1}{P'0} \pm \frac{2\cos\psi_0}{R_2} \qquad \text{- sign for concave surfaces.}$$

$$(\cos\psi_0 = -\hat{n} \cdot \hat{I})$$

R_1 and R_2 are the radii of curvatures of the surface at 0. The above formulas are valid only in the principal planes. R_1 is the radius of curvature in the plane of incidence (or reflection), whereas R_2 is the radius of curvature in the plane orthogonal to the plane of incidence (or reflection). Let us define the following quantities:

$$(17) \qquad \hat{\beta}_i \cdot \bar{E}^i(0) \equiv E^i_{\parallel}(0)$$

(18) $$\hat{\phi}_i \cdot \bar{E}^i(0) \equiv E^i(0)$$

(19) $$\hat{\beta}'' \cdot \bar{E}^r(P) \equiv E_{\parallel}^r(P)$$

(20) $$\hat{\phi}'' \cdot \bar{E}^r(P) \equiv E_{\perp}^r(P)$$

With the help of the quantities defined above, Eq. (14) may be expressed in a convenient matrix form as:

(21) $$\begin{bmatrix} E_{\parallel}^r(P) \\ \hline E_{\perp}^r(P) \end{bmatrix} \sim \begin{bmatrix} 1 & \vdots & 0 \\ \cdots & \vdots & \cdots \\ 0 & \vdots & -1 \end{bmatrix} \begin{bmatrix} E_{\parallel}^i(0) \\ \hline E_{\perp}^i(0) \end{bmatrix} \sqrt{\frac{\rho_1 \rho_2}{(\rho_1+s)(\rho_2+s)}}\, e^{-jks}$$

The above representation for the geometrical optics reflected field is valid at all angles of incidence except near grazing incidence. At grazing incidence the incident ray becomes tangent to the surface of the scatterer, and phenomenon of surface diffraction occurs. The geometrical optics reflected field contributes to the scattered field only in the specular direction. The techniques of geometrical optics discussed above are next extended to account for the phenomenon of diffraction.

B. Geometrical Theory of Diffraction

The Geometrical Theory of Diffraction (GTD) was introduced by Keller[1] as a systematic extension of geometrical optics to describe the diffraction phenomenon in terms of rays. The regions which form the geometrical shadow constitute the regions for which the geometrical optics fields are zero. The field in the shadow region is due to diffraction and cannot be accounted for by ordinary geometrical optics. Thus, GTD postulates the existence of diffracted rays to describe the diffracted fields in a manner analogous to that of the geometrical optics rays which successfully describe high frequency incident, re-

flected and transmitted (refracted) fields outside the shadow regions. Diffracted rays are produced whenever an incident ray strikes a smooth surface at grazing incidence, or strikes an edge, corner, or a tip of a scattering object. Figures 4(a), 4(b), 4(c) and 4(d) show

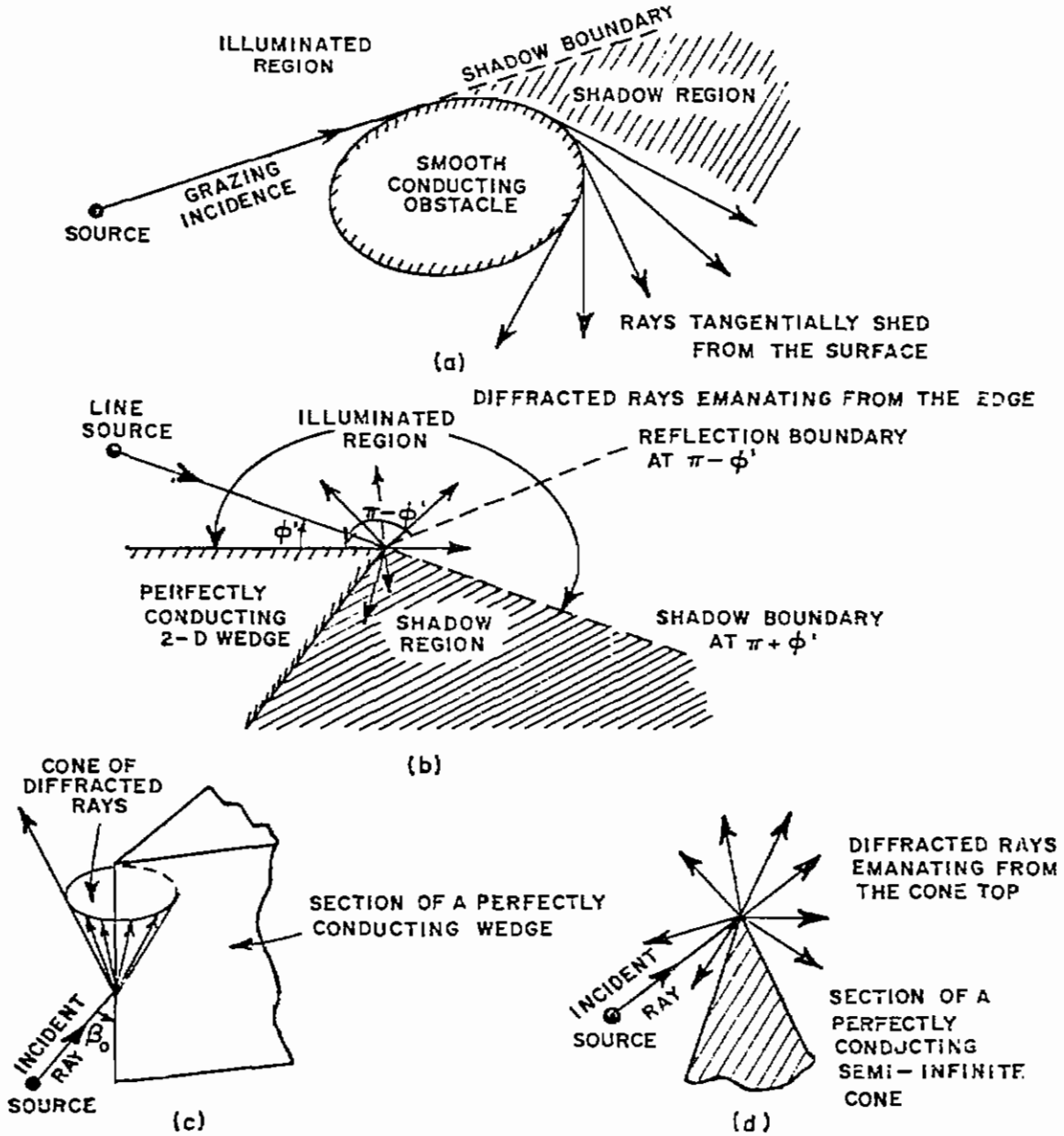

Fig. 4. Examples of diffracted rays.

some examples of diffracted rays; the regions of geometrical shadow (shadow regions) are also indicated in Figs. 4(a) and 4(b). Although diffracted rays primarily account for the fields in the shadow region, they are also generally present in the illuminated region. Thus, according to geometrical optics, the region of space surrounding a scatterer is divided into the illuminated and shadow regions. The shadow boundary delineates these two regions. The illuminated region contains the incident field and generally the diffracted field (which, depending on the particular situation involved, may or may not constitute a significant contribution to the total field); a portion of the illuminated region may also contain the reflected field. According to geometrical optics, the reflection boundary bounds the domain of the reflected field. Fig. 4(b) illustrates the shadow and reflection boundaries. The shadow region, more precisely the shadow region associated with the incident field, contains only the diffracted field. The shadow region associated with reflected field is not shown in Fig. 4(b) for clarity but it would exist from the reflection boundary to the back surface of the wedge. Fig. 4(a) indicates that a ray from the source which strikes the surface at grazing incidence (i.e., at the shadow boundary) produces fields diffracted into the shadow region. According to GTD, the diffraction mechanism consists of a tangential shedding of surface rays which creep around the smooth convex scatterer as shown in Fig. 4(a). In Figs. 4(b) and 4(c), the diffracted rays are produced when the incident rays from the source strike the sharp edge of a wedge. In Fig. 4(d), the diffracted rays are produced when the incident ray strikes the cone tip. Diffraction and reflection are local phenomenon at sufficiently high frequencies so that in the ray optical description, the total scattered field is made up of contributions from certain localized portions of the scatterer such as the points of reflection and diffraction. The total field at the observation point is obtained via a superposition of the contributions from all the different rays (incident, reflected and diffracted rays; whichever are present) which pass through the

observation point. In the GTD representation, the diffracted field $\bar{E}^d$ may be written in the ray optic form of Eq. (3) as

$$\bar{E}^d(P) \sim \left\{\bar{E}^i(Q) \cdot \bar{\bar{D}}\right\} F(s)\, e^{-jks}, \tag{22}$$

P and Q are points of observation and diffraction, respectively. $\bar{E}^i(Q)$ represents the field incident at the point of diffraction. $\bar{\bar{D}}$, the dyadic diffraction coefficient may be viewed as a transfer function which relates the diffracted field to the field incident at the point of diffraction. $\bar{\bar{D}}$ depends on the local properties of the scatterer in the immediate vicinity of the point of diffraction. The explicit form of $\bar{\bar{D}}$ is generally deduced from an asymptotic high frequency solution to a pertinent canonical problem; the asymptotic solution must be cast in the form of Eq. (22) before $\bar{\bar{D}}$ is identifiable.

The geometrical optics reflected ray obeys Fermat's principle with a constraint. In particular, the path from P' to P (Fig. 2) is an extremum subject to the constraint that a point (point of reflection) on the ray path touches the surface for the reflected ray (if the constraint is not incorporated, the straight line path P'P corresponding to the incident or direct ray from the source is obtained). Such a generalization of Fermat's principle which works for reflected rays may be systematically extended to define the ray paths for the class of diffracted rays[1]. The diffraction phenomenon associated with an edge structure is discussed next, and is followed by a discussion on the diffraction by curved surfaces. The wedge and the curved surface form two very basic and important geometries in the study of diffraction theory. Fig. 5(a) illustrates a point source at P' illuminating a perfectly conducting wedge of internal angle $(2-n)\pi$. The observation point is at P, and Q is the point of edge diffraction. For a given set of points P and P' there is a unique point of diffraction, Q'. The path P'QP is an extremum as a consequence of extending Fermat's principle for edge diffracted rays. Thus, if the

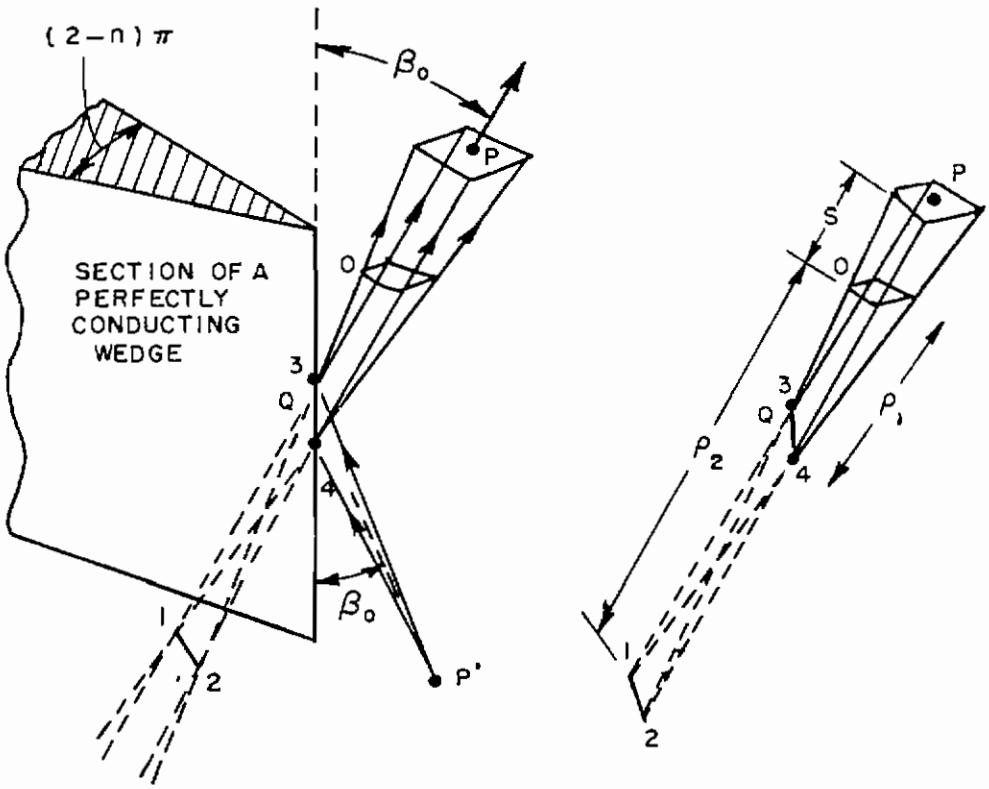

Fig. 5. Diffraction by a wedge.

incident ray P'Q makes an angle β_0 with the edge, the diffracted rays must lie on a cone of half angle β_0 as indicated in Fig. 4(c). If the rays at P are extended backwards, an astigmatic ray bundle emerges as shown in Fig. 5(b). The caustic 3-4 is an edge caustic. According to the geometry in Fig. 5(b), the diffracted field at P may be written in terms of the reference field at O as

$$\bar{E}^d(P) \sim \bar{E}^d(O) \sqrt{\frac{\rho_1 \rho_2}{(\rho_1+s)(\rho_2+s)}}\, e^{-jks} \tag{23}$$

It is convenient to move the reference point O to the edge at Q, so that $\rho_1 \to 0$. The value of the field at Q is unbounded since 3-4 is a caustic ; however, $\bar{E}^d(S)$ is independent of the location of the reference point O so that

$$\lim_{\substack{\rho_1 \to 0 \\ (O \to Q)}} \bar{E}^d(O)\sqrt{\rho_1}$$

exists and is denoted by $\bar{E}^i(Q) \cdot \bar{\bar{D}}_E$, where $\bar{E}^i(Q)$ is the field from P' incident on the edge at Q. $\bar{\bar{D}}_E$ is the "dyadic wedge diffraction coefficient." Let $\rho_2 \equiv \rho_c$, then

$$(24) \qquad \bar{E}^d(P) \sim \bar{E}^i(Q) \cdot \bar{\bar{D}}_E \sqrt{\frac{\rho_c}{s(\rho_c+s)}}\, e^{-jks}$$

Note that the distance s now corresponds to the length QP , and

$$F(s) = \sqrt{\frac{\rho_c}{s(\rho_c+s)}}$$

The form of $\bar{\bar{D}}_E$ simplifies considerably if one expresses the fields $\bar{E}^d(P)$ and $\bar{E}^i(Q)$ in their respective ray coordinate systems[10] instead of the edge-fixed coordinate system at Q[11].

Let the plane containing the incident ray and the edge be the plane of incidence. Let us define unit vectors $\hat{\beta}_0'$ and $\hat{\phi}_0'$ such that $\hat{\beta}_0'$ lies in the plane of incidence with $\hat{\beta}_0' \cdot \hat{I}_0 = 0$ ($\hat{I}_0$ being the direction of incidence) and $\hat{I}_0 = \hat{\beta}_0' \times \hat{\phi}_0'$, so that $\hat{\phi}_0'$ lies normal to the plane of incidence. Similarly, we define the unit vectors $\hat{\beta}_0$ and $\hat{\phi}$ such that $\hat{\beta}_0$ lies in the plane of diffraction, and $\hat{\phi}$ lies normal to the plane of diffraction. The plane of diffraction is the plane containing the diffracted ray and the edge. If $\hat{S}$ is the direction of diffraction, then $\hat{\beta}_0$ and $\hat{\phi}$ satisfy $\hat{\beta}_0 \cdot \hat{S} = 0$ and

$\hat{S} = \hat{\beta}_o \times \hat{\phi}$. Fig. 6 indicates the wedge diffraction geometry, and the unit vectors. It can be shown[10] that in terms of the unit vectors

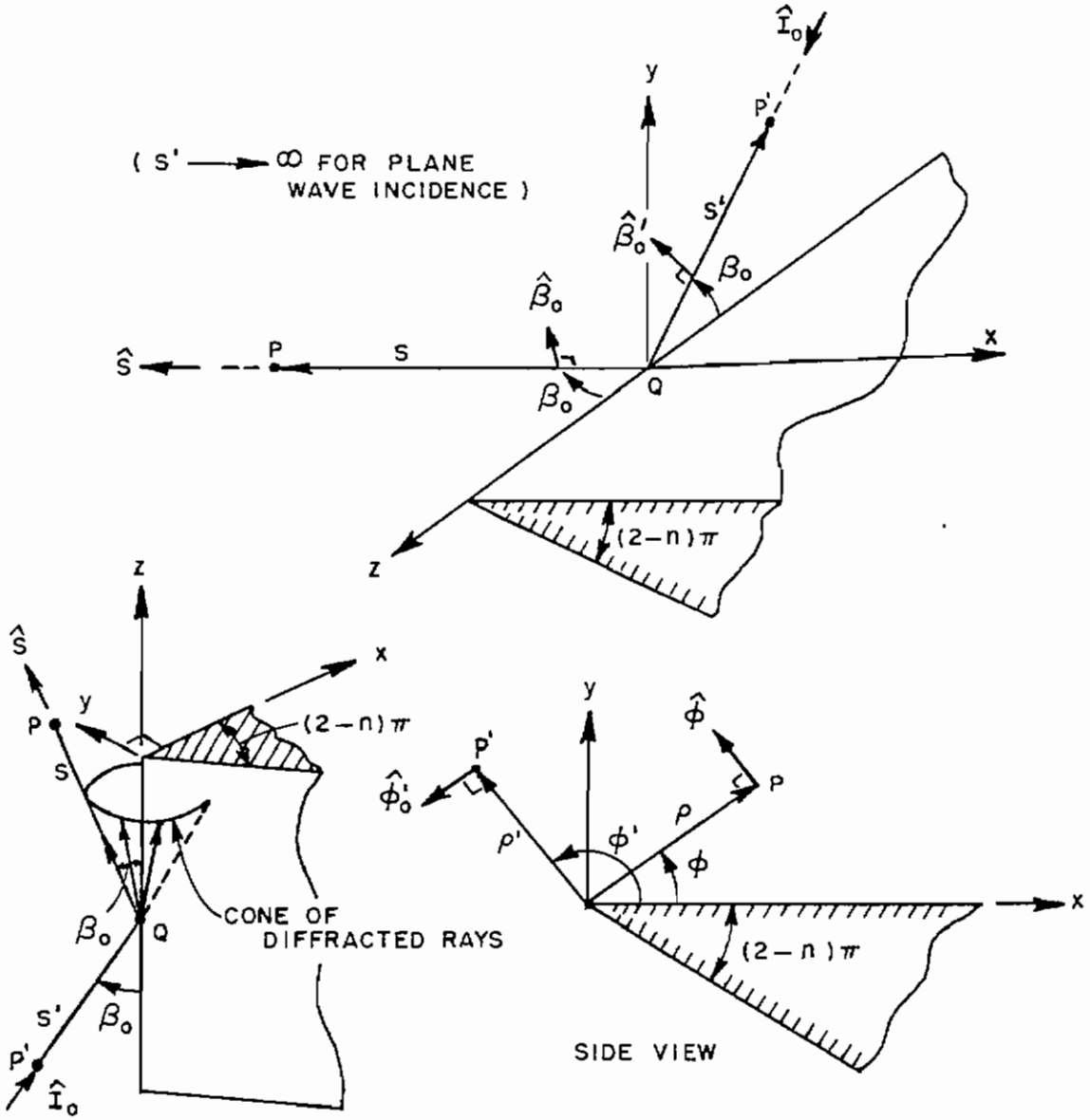

$\hat{I}_o = \hat{\beta}_o' \times \hat{\phi}_o'$ AND $\hat{S} = \hat{\beta}_o \times \hat{\phi}$ DEFINE $\hat{\beta}_o'$ AND $\hat{\beta}_o$ RESPECTIVELY

Fig. 6. Wedge diffraction geometry.

of the coordinate systems fixed in the incident and diffracted rays, $\overline{\overline{D}}_E$ is given by

$$(25a) \qquad \overline{\overline{D}}_E = - \hat{\beta}_o' \, \hat{\beta}_o \, D_s - \hat{\phi}_o' \, \hat{\phi} \, D_h \quad .$$

The specific functional form of $\overline{\overline{D}}$ in terms of D_s and D_h is obtained from an asymptotic solution to the canonical problem of electromagnetic scattering by a perfectly conducting wedge[10]. D_s and D_h correspond to the scaler wedge diffraction coefficients for the acoustic soft (homogeneous Dirichlet boundary condition on the wedge) case and the acoustic hard (homogeneous Neuman boundary condition on the wedge) case, respectively.

$$(25b) \qquad D_{\substack{s \\ h}} = \frac{1}{\sin \beta_o} \left[\{ d^+(\beta^-,n) F[\kappa a^+(\beta^-)] + d^-(\beta^-,n) F[\kappa a^-(\beta^-)] \} \right.$$

$$\mp \{ d^+(\beta^+,n) F[\kappa a^+(\beta^+)] +$$

$$\left. + \, d^-(\beta^+,n) F[\kappa a^-(\beta^+)] \} \right],$$

where

$$(26) \qquad d^{\pm}(\beta,n) = - \frac{e^{-j\frac{\pi}{4}}}{n\sqrt{2\pi k}} \cdot \frac{1}{2} \cot \frac{\pi \pm \beta}{2n} \quad , \text{ in which } \beta = \beta^{\mp} \equiv (\phi^{\mp} \phi')$$

and

$$(27) \qquad F[\kappa a^{\pm}(\beta)] = 2j \left| \sqrt{\kappa a^{\pm}(\beta)} \cdot \right| e^{j\kappa a^{\pm}(\beta)} \int_{\left| \sqrt{\kappa a^{\pm}(\beta)} \right|}^{\infty} e^{-j\tau^2} \, d\tau$$

The parameters which appear in $F[\kappa a^{\pm}(\beta)]$ are defined below

$$(28) \qquad a^{\pm}(\beta) = 1 + \cos(-\beta + 2nN^{\pm}\pi)$$

in which $N^{\pm}$ is the positive or negative integer or zero, which most nearly satisfies the equations

$$(29) \qquad \begin{cases} 2n\pi N^{-} - \beta = -\pi, \\ 2n\pi N^{+} - \beta = \pi. \end{cases}$$

$\kappa = kL$ is the largeness parameter in the asymptotic evaluation of the pertinent integrals involved in the formulation of the dyadic diffraction coefficient. The quantity L (appearing in $\kappa = kL$) may be viewed as a distance parameter which depends upon the type of edge illumination; it is given by

$$(30) \qquad L = \begin{cases} s \sin^2\beta_o & \text{for plane waves,} \\ \dfrac{\rho'\rho}{\rho+\rho'} & \text{for cylindrical waves,} \\ \dfrac{s's \sin^2\beta_o}{s + s'} & \text{for conical and spherical waves.} \end{cases}$$

The distances s, s', ρ, ρ' and the angles ϕ, ϕ' are indicated in Fig. 6. For grazing incidence ($\phi' = 0, n\pi$), D_h is multiplied by $\frac{1}{2}$ whereas $D_s = 0$. It is worth emphasizing that if an edge-fixed coordinate-system at Q was used instead of the ray-fixed coordinate system, $\overline{\overline{D}}_E$ would contain a sum of seven dyads instead of the sum of only two dyads as indicated in Eq. (24). The function $F[ka^{\pm}(\beta)]$ is referred to as the Transition Function; it ensures that the total field surrounding the wedge is everywhere finite and continuous. In Fig. 4(b) it is seen that, in the geometrical optics description, the reflected and incident fields vanish abruptly beyond the reflection and shadow boundaries, respectively. The Transition Function for the diffracted field properly compensates for the discontinuities in the geometrical optics field to yield a total field which is smooth everyplace. The regions adjacent to the shadow and reflection boundaries

are called the transition regions and hence $F[ka^{\pm}(\beta)]$ is referred to as the transition function. Away from the transition region, $F[ka^{\pm}(\beta)] \to 1$, and D_s reduce to the ordinary wedge diffraction coefficient obtained by Keller[1]. The wedge diffraction coefficient given in Reference [1] is not valid in the transition regions of the shadow and reflection boundaries. A plot of $F[ka^{\pm}(\beta)]$ as a function of $ka^{\pm}(\beta) \equiv kLa$ is shown in Fig. 7. The result in Eq. (24) when used in conjunction with Eq. (25)

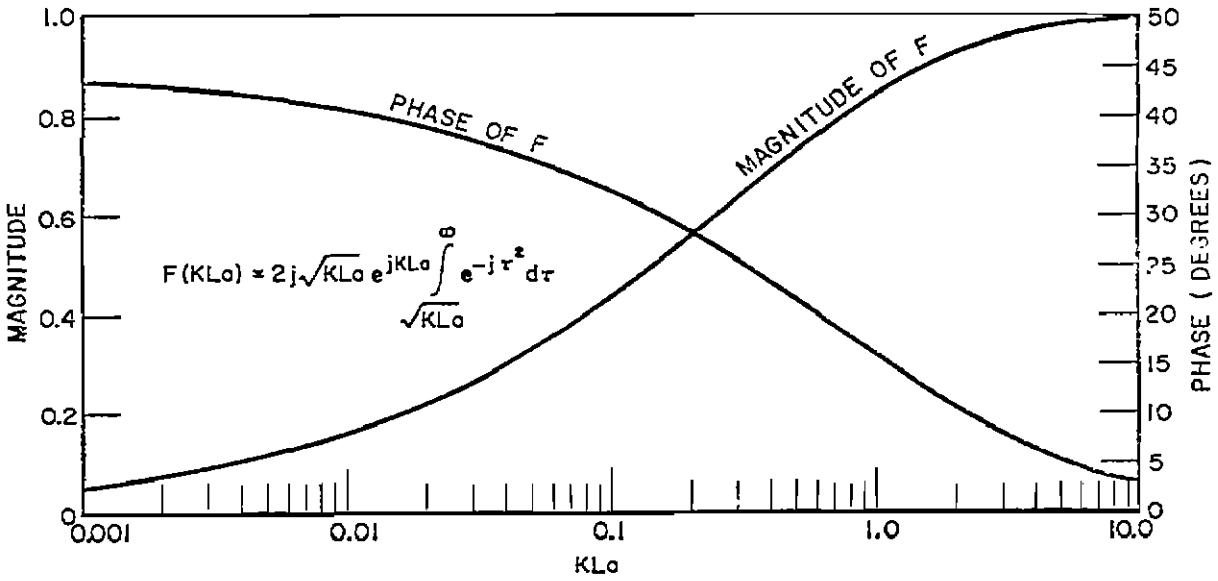

Fig. 7. Transition function.

yields a diffracted field which matches the reflected field and incident field discontinuities at the reflection and shadow boundaries, respectively, in amplitude as well as polarization. The form for the wedge diffracted field $\bar{E}^d$ in Eq. (24) reduces to the less general V_B representation used in some of the ElectroScience Laboratory technical reports which will be alluded to later in our discussions. The radiation patterns of slots or monopoles on perfectly conducting wedges can be easily obtained via the results outlined above. Note that in these cases, $\phi' = 0$, or $n\pi$, so that D_h is replaced by $D_h/2$ and $D_s = 0$.

If $\hat{\beta}_o' \cdot \bar{E}^i(Q) \equiv E_{\parallel}^i(Q)$, $\hat{\phi}_o' \cdot \bar{E}^i(Q) \equiv E_{\perp}^i(Q)$ and similarly, if $\hat{\beta} \cdot \bar{E}^d(P) \equiv E_{\parallel}^d(P)$ and $\hat{\phi} \cdot \bar{E}^d(P) \equiv E_{\perp}^d(P)$ then we may rewrite $\bar{E}^d(P)$ as:

$$(31) \qquad \begin{bmatrix} E_{\parallel}^d(P) \\ \hline E_{\perp}^d(P) \end{bmatrix} \sim \begin{bmatrix} -D_s & 0 \\ \hline 0 & -D_h \end{bmatrix} \begin{bmatrix} E_{\parallel}^i(Q) \\ \hline E_{\perp}^i(Q) \end{bmatrix} \quad F(s)\, e^{-jks}$$

where

$$F(s) = \sqrt{\frac{\rho_c}{s(\rho_c+s)}} \quad ;$$

and the caustic distance ρ_c is identical to s' for the configuration in Fig. 5.

We next consider the diffraction by a smooth, perfectly conducting curved surface. Figure 8(a) indicates a ray from the source at P' incident at Q' on the curved surface. P'Q' is a tangent to the surface at Q'; hence the field at Q' is incident at the grazing angle so that a shadow boundary is formed as shown by the dotted line. In the illuminated region, the fields may be described in terms of the geometrical optics components which propagate along the incident and reflected rays, whereas, the diffracted field in the shadow region may be expressed in terms of the surface ray modes of Keller (GTD). The incident field at Q' launches an infinite set of surface ray modes which traverse a geodesic path on the surface. The field of the surface ray modes attenuates along the geodesic path via a tangential shedding of rays, so that the diffracted ray arriving at P is shed tangentially from Q. The path from P' to P is an extremum subject to the constraint that a portion of it lies on the curved surface in accordance with the generalized Fermat's principle for rays diffracted by a curved impenetrable surface. Consequently, Q'Q is a geodesic and, P'Q' and PQ are tangents to Q' and Q, respectively. In addition to the attenuation due to a tangential shedding of rays, the field also attenuates due to a spreading of the rays along Q'Q resulting from

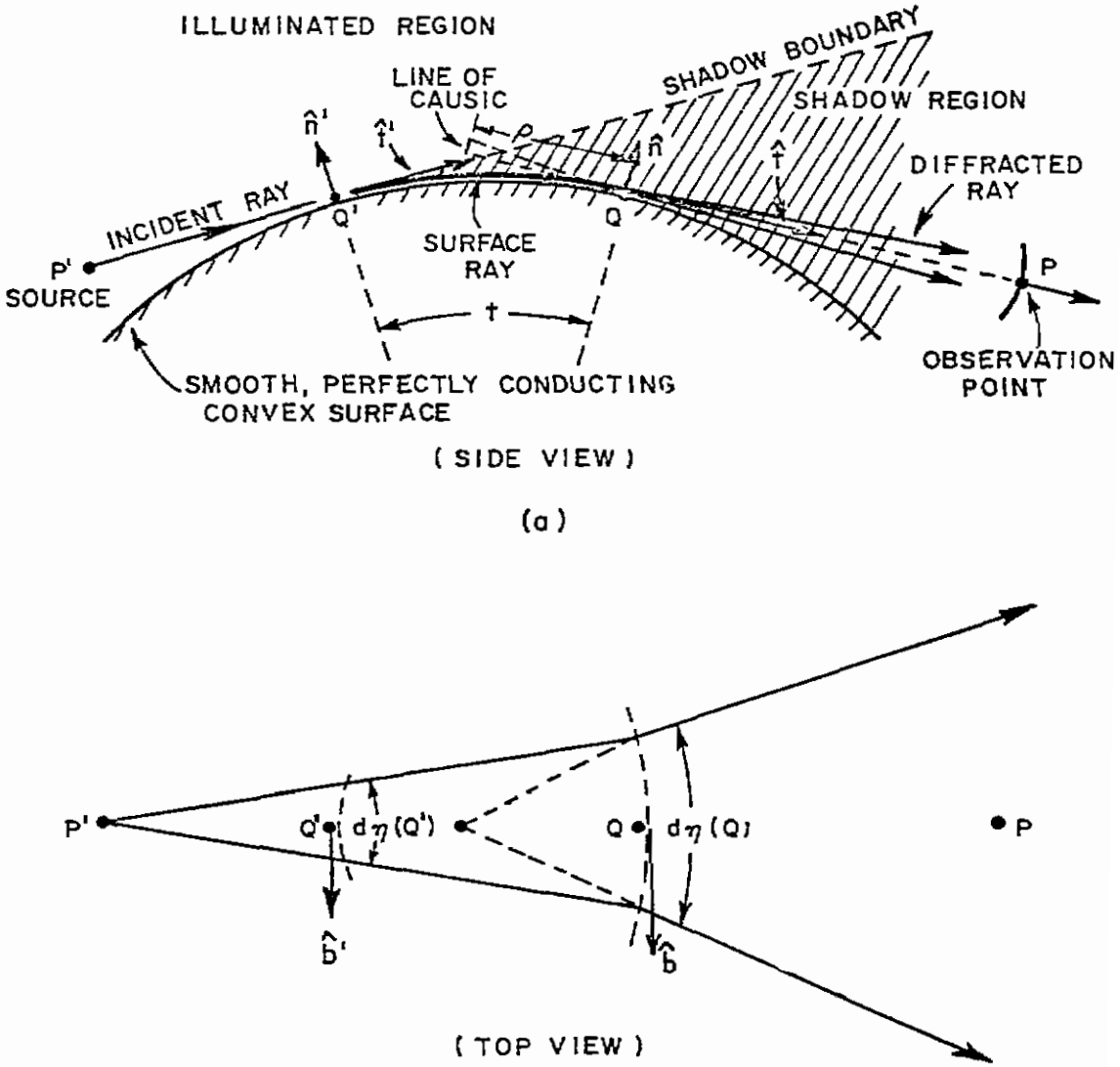

Fig. 8. Surface wave diffraction ray geometry.

the effects of curvature in the plane transverse to the path Q'Q. This spreading is responsible for producing a caustic off the surface as shown in Fig. 8(a). The caustic distance ρ is obtained by projecting the rays from Q to P backwards until they intersect (see Fig. 8(b)). The unit vectors $\hat{t}$, $\hat{n}$ and $\hat{b}$ in Fig. 8(a) denote the tangent, normal, and binormal directions to the ray path at Q, respectively. Similarly, $\hat{t}'$, $\hat{n}'$ and $\hat{b}'$ represent the corresponding triad of unit vectors at Q'. In particular, $\hat{b} = \hat{t} \times \hat{n}$ and $\hat{b}' = \hat{t}' \times \hat{n}'$. The field of the incident ray is assumed to be polarized transverse to the ray path in the ray optic approximation so that the incident electric field at Q' may be decomposed into components along $\hat{b}'$ and $\hat{n}'$, respectively. Let $\bar{E}^i(Q')$ represent the incident electric field intensity at Q'. Then

$$\bar{E}^i(Q') = (\hat{n}'\,\hat{n}' + \hat{b}'\,\hat{b}') \cdot \bar{E}^i(Q') \quad . \tag{32}$$

The diffracted field at P can be expressed as

$$\bar{E}^d(P) \sim \bar{E}(Q) \cdot \bar{\bar{D}}_p(Q) \sqrt{\frac{\rho}{s(\rho+s)}}\; e^{-jks} \tag{33}$$

where $\bar{E}(Q) \cdot \bar{\bar{D}}_p(Q)$ is the value of the reference field at Q which is a line caustic on the surface. $\bar{E}(Q)$ is the field incident at Q along the path P'Q'Q, and $\bar{\bar{D}}_p(Q)$ is the dyadic curved surface diffraction coefficient at Q which relates the diffracted field at P due to a field incident at Q.

$$\bar{\bar{D}}_p(Q) = \hat{b}\,\hat{b}\,D_p^s(Q) + \hat{n}\,\hat{n}\,D_p^h(Q). \tag{34}$$

D_p^s and D_p^h are the acoustic soft and acoustic hard diffraction coefficients for a smooth, convex impenetrable surface. More specifically, the field $\bar{E}(Q)$ may be expressed in terms of the field incident at Q' as:

$$(35)\qquad \bar{E}(Q) \sim \bar{E}^{i}(Q') \cdot \left[\sqrt{\frac{d\eta(Q')}{d\eta(Q)}} \left\{ \sum_{p=1}^{\infty} \hat{n}'\hat{n}\, D_p^h(Q')\, e^{-\int_{Q'}^{Q} \alpha_p^h\, ds} \right.\right.$$

$$\left.\left. + \sum_{p=1}^{\infty} \hat{b}'\hat{b}\, D_p^s(Q')\, e^{-\int_{Q'}^{Q} \alpha_p^s\, ds} \right\} \cdot e^{-jk(Q'Q)} \right]$$

ds = incremental arc length along Q'Q. The arc length Q'Q = t. α_p^s and α_p^h are the acoustic soft and acoustic hard attenuation constants, respectively; they describe the rate at which energy is shed tangentially along the path Q'Q. The factor

$$\sqrt{\frac{d\eta(Q')}{d\eta(Q)}}$$

yields the attenuation due to a spreading of rays on the surface, along the path Q'Q. Each surface ray mode has it's own attenuation and diffraction coefficient as is evidenced by the mode index p used as a subscript on D_p^s and $\hat{n}_p^s$. In Eq. (35) it is assumed that the surface ray is a curve of zero torsion. However, it should be possible to remove this restriction and obtain a more general result. The result of Eq. (34) is used in Eq. (33) to give the complete result for $\bar{E}^d(P)$. Reciprocity requires that $D_p^s(Q)$ and $D_p^s(Q')$ have the same functional forms. The values of $(D_p^h)^2$, $(D_p^s)^2$, and α_p^h, α_p^s are given in Tables A and B from Voltmer[12,13]. The values of D_p^h and D_p^s may be obtained by taking the principal branch of the square root of the product of column A and column B. The summation on p is rapidly convergent in the shadow and usually only a few modes suffice. In case the curved surface is a closed surface, the surface rays undergo multiple encirclements around the closed convex body. However, for large objects,

TABLE A

GENERALIZED DIFFRACTION COEFFICIENTS AND ATTENUATION CONSTANTS

Surface	SQUARE OF DIFFRACTION COEFFICIENT D_p^2 - (Column A) · (Column B)		ATTENUATION CONSTANT α_p - (Column C) · (Column D)	
	A. Keller's Result	B. Correction Terms	C. Keller's Result	D. Correction Terms
Soft Acoustic and Soft EM	$\frac{\pi^{-1/2}2^{-5/6}\rho_g^{1/3}e^{-j\pi/12}}{k^{1/6}(Ai'(-q_p))^2}$	$1+\left(\frac{2}{k\rho_g}\right)^{2/3}q_p\left(\frac{1}{30}+\frac{\rho_g}{4\rho_{tn}}+\frac{\rho_g\beta_g}{180}\right)e^{-j\pi/3}$	$\frac{q_p}{\rho_g}e^{j\pi/6}\left(\frac{k\rho_g}{2}\right)^{1/3}$	$1+\left(\frac{2}{k\rho_g}\right)^{2/3}q_p\left(\frac{1}{60}-\frac{2}{45}\rho_g\beta_g+\frac{4}{135}\beta_g^2\right)e^{-j\pi/3}$
Hard Acoustic	$\frac{\pi^{-1/2}2^{-5/6}\rho_g^{1/3}e^{-j\pi/12}}{k^{1/6}\bar{q}_p(Ai(-\bar{q}_p))^2}$	$1+\left(\frac{2}{k\rho_g}\right)^{2/3}\left(\bar{q}_p\left(\frac{1}{30}+\frac{\rho_g}{4\rho_{tn}}+\frac{\rho_g\beta_g}{180}\right)-\frac{1}{\bar{q}_p^2}\left(\frac{1}{10}+\frac{\rho_g}{4\rho_{tn}}-\frac{\rho_g\beta_g}{60}\right)\right)e^{-j\pi/3}$	$\frac{\bar{q}_p}{\rho_g}e^{j\pi/6}\left(\frac{k\rho_g}{2}\right)^{1/3}$	$1+\left(\frac{2}{k\rho_g}\right)^{2/3}\left(\bar{q}_p\left(\frac{1}{60}-\frac{2}{45}\rho_g\beta_g+\frac{4}{135}\dot{\rho}_g^2\right)+\frac{1}{\bar{q}_p^2}\left(\frac{1}{10}+\frac{\rho_g}{4\rho_{tn}}-\frac{\rho_g\beta_g}{60}+\frac{\dot{\rho}_g^2}{90}\right)\right)e^{-j\pi/3}$
Hard EM		$1+\left(\frac{2}{k\rho_g}\right)^{2/3}\left(\bar{q}_p\left(\frac{1}{30}+\frac{\rho_g}{4\rho_{tn}}+\frac{\rho_g\beta_g}{180}\right)-\frac{1}{\bar{q}_p^2}\left(\frac{1}{10}-\frac{\rho_g}{4\rho_{tn}}-\frac{\rho_g\beta_g}{60}\right)\right)e^{-j\pi/3}$		$1+\left(\frac{2}{k\rho_g}\right)^{2/3}\bar{q}_p\left(\frac{1}{60}-\frac{2}{45}\rho_g\beta_g+\frac{4}{135}\dot{\rho}_g^2\right)+\frac{1}{\bar{q}_p^2}\left(\frac{1}{10}-\frac{\rho_g}{4\rho_{tn}}-\frac{\rho_g\beta_g}{60}+\frac{\dot{\rho}_g^2}{90}\right)e^{-j\pi/3}$

ρ_g = radius of curvature along the geodesic

ρ_{tn} = radius of curvature perpendicular to the geodesic (transverse curve)

Dots indicate differentiation with respect to arc length variable

TABLE B

DIFFRACTION COEFFICIENTS AND ATTENUATION CONSTANTS FOR CIRCULAR CYLINDERS AND SPHERES

Surface	SQUARE OF DIFFRACTION COEFFICIENT D_p^2 = (Column A) · (Column B)		ATTENUATION CONSTANT α_p = (Column C) · (Column D)		ZEROES OF THE AIRY FUNCTION
	A. Keller's Result	B. Correction Terms	C. Keller's Result	D. Correction Terms	
Soft Cylinder	$\frac{\pi^{-1/2}2^{-5/6}a^{1/3}e^{-j\pi/12}}{k^{1/6}(Ai'(-q_p))^2}$	$1 + \left(\frac{2}{ka}\right)^{2/3} q_p \frac{1}{30} e^{-j\pi/3}$	$\frac{q_p}{a} e^{j\pi/6} \left(\frac{ka}{2}\right)^{1/3}$	$1 + \left(\frac{2}{ka}\right)^{2/3} \frac{q_p}{60} e^{-j\pi/3}$	$Ai(-q_p) = 0$ $q_1 = 2.33811$ $q_2 = 4.08795$ $Ai'(-q_1) = .70121$ $Ai'(-q_2) = -.80311$
Soft Acoustic and Soft EM Sphere		$1 + \left(\frac{2}{ka}\right)^{2/3} q_p \left(\frac{1}{30} + \frac{1}{4}\right) e^{-j\pi/3}$			
Hard Cylinder	$\frac{\pi^{-1/2}2^{-5/6}a^{1/3}e^{-j\pi/12}}{k^{1/6}\bar{q}_p(Ai(-\bar{q}_p))^2}$	$1 + \left(\frac{2}{ka}\right)^{2/3} \left(\frac{\bar{q}_p}{30} - \frac{1}{\bar{q}_p^2} \frac{1}{10}\right) e^{-j\pi/3}$	$\frac{\bar{q}_p}{a} e^{j\pi/6} \left(\frac{ka}{2}\right)^{1/3}$	$1 + \left(\frac{2}{ka}\right)^{2/3} \left(\frac{\bar{q}_p}{60} + \frac{1}{\bar{q}_p^2} \frac{1}{10}\right) e^{-j\pi/3}$	ZEROES OF THE DERIVATIVE OF THE AIRY FUNCTION $Ai'(-\bar{q}_p) = 0$ $\bar{q}_1 = 1.01879$ $\bar{q}_2 = 3.24820$ $Ai(-\bar{q}_1) = .53566$ $Ai(-\bar{q}_2) = -.41902$
Hard Acoustic Sphere		$1 + \left(\frac{2}{ka}\right)^{2/3} \left(\bar{q}_p\left(\frac{1}{30} + \frac{1}{4}\right) - \frac{1}{\bar{q}_p^2}\left(\frac{1}{10} + \frac{1}{4}\right)\right) e^{-j\pi/3}$		$1 + \left(\frac{2}{ka}\right)^{2/3} \left(\frac{\bar{q}_p}{60} + \frac{1}{\bar{q}_p^2}\left(\frac{1}{10} + \frac{1}{4}\right)\right) e^{-j\pi/3}$	
Hard Em Sphere		$1 + \left(\frac{2}{ka}\right)^{2/3} \bar{q}_p \left(\frac{1}{30} + \frac{1}{4}\right) - \frac{1}{\bar{q}_p^2}\left(\frac{1}{10} - \frac{1}{4}\right)\right) e^{-j\pi/3}$		$1 + \left(\frac{2}{ka}\right)^{2/3} \left(\frac{\bar{q}_p}{60} + \frac{1}{\bar{q}_p^2}\left(\frac{1}{10} - \frac{1}{4}\right)\right) e^{-j\pi/3}$	

these rays are sufficiently attenuated so that one may neglect the contribution due to a shedding from the multiply encircling surface rays. For such closed convex surfaces, a caustic of the diffracted rays may be formed along a particular direction of observation. The GTD solution breaks down at and near the caustics of diffracted rays. However, the GTD representation may be used indirectly to correct the fields through the caustic region[12,13].

C. Applications of Ray Optics

In this section the results of the application of diffraction theory to certain basic problems which have some bearing on the aircraft surface current and charge density problem will be reviewed. The first of these is the source located on a 90° wedge as shown in Fig. 9. The radiated field is calculated using GTD and compared with the solution obtained by an eigenfunction expansion. The pattern may be successfully computed using GTD as long as the source and 90° edge are separated by a quarter of a wavelength or more. This shows that the diffraction effects are localized. The pattern of Fig. 9 can be interpreted as the current density at the position of the slot and perpendicular to it by use of the following procedure. The slot can be represented by a magnetic line source and the reciprocity theorem gives

$$(36) \qquad \langle M^1, H^2 \rangle = \langle M^2, H^1 \rangle$$

where $\bar{M}^1$ is the magnetic current density representing the slot density of the source and is set equal to unity.

$\bar{H}^1$ is its far field magnetic field intensity.

$\bar{M}^2$ is a magnetic current density of a distant source far removed from the slot and the edge of the wedge.

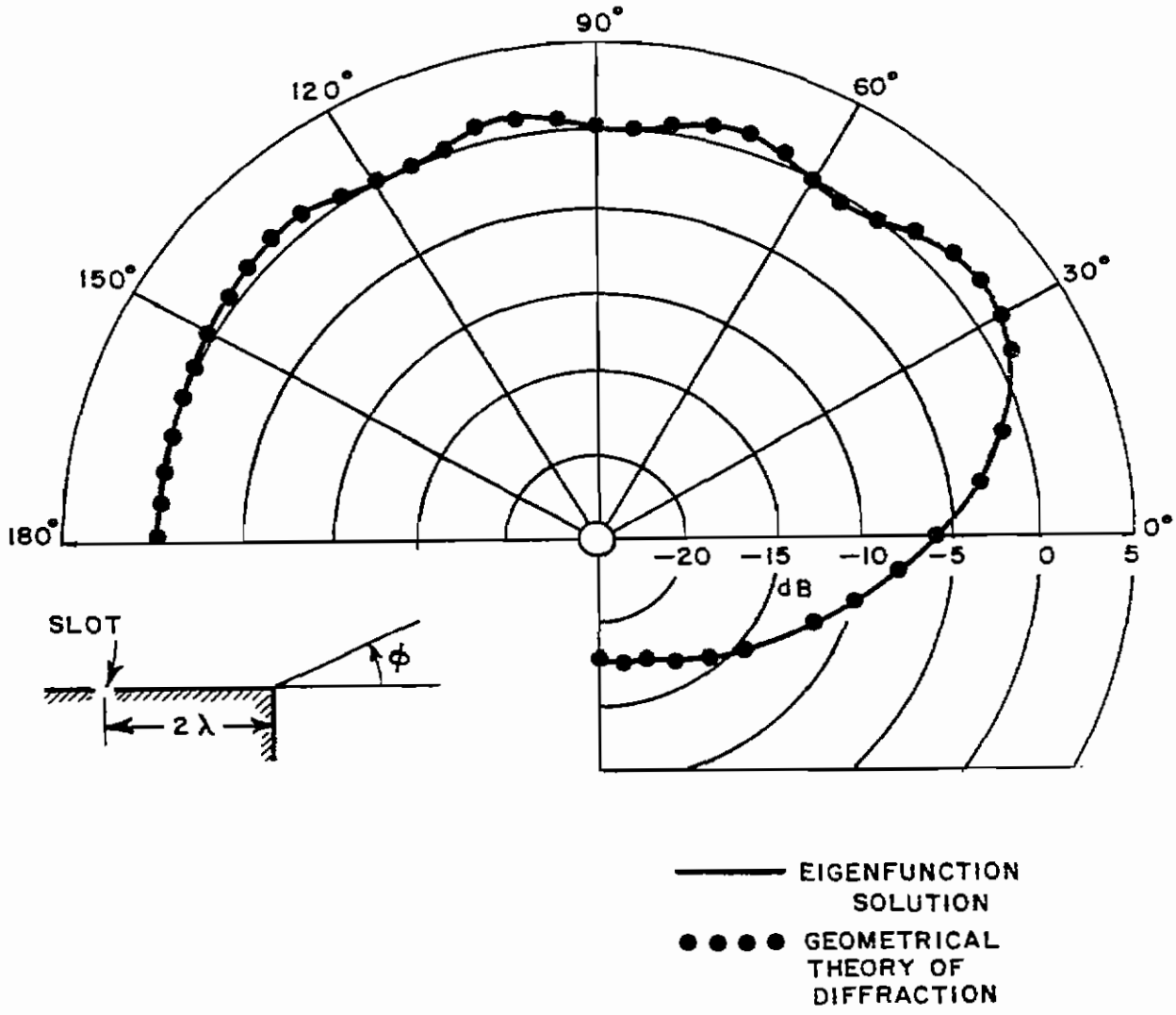

Fig. 9. Radiation pattern of an infinitesimal slot on a perfectly conducting right-angle wedge.

H^2 is the magnetic field intensity at the slot and is parallel to $\overline{M}^1$. For line sources, the reaction of Eq. (36) gives

$$(37) \qquad \overline{M}^1 \cdot \overline{H}^2 = \overline{M}^2 \cdot H^1$$

or

$$M^1 H^2 = M^2 H^1$$

where M^2 is a constant. Thus if the second magnetic line source M^2 is moved on a radius about the wedge, the magnetic field intensity induced by it at the position of the slot is proportional to the pattern of the slot-wedge geometry. Furthermore, physical optics predicts the current density $\overline{J} = 2\hat{n} \times \overline{H}^i$ and for an incident field from $\phi = 90°$, $|J| = |2H^i|$. This is a good approximation for large smooth conducting bodies. For example, the physical optics current density on an infinitely long perfectly conducting cylinder is about 30% in error for a cylinder whose radius is as small as 0.159λ, and less than 10% in error for end on incidence of 1.5λ long rod with a spherical cap whose radius is 0.2λ. This approximation is further substantiated in the next section where actual calculations of the magnetic field intensity are given for plane wave incidence.

Thus Eq. (37) can be calibrated to give the magnetic field intensity at the slot position of Fig. 9 from a plane wave whose incident magnetic field intensity is H^i or

$$(38) \qquad \overline{H}^2 = \hat{a}_\ell \, 2 \, H^i \, \frac{F(\phi)}{F(90)}$$

where $\hat{a}_\ell$ is unit vector parallel to the slot.

$F(\phi)$ is the antenna radiation pattern of the slot on the conducting body. Finally the electric current density for plane wave incidence on this slot wedge geometry is

(39) $$\bar{J} = \hat{a}_T \, 2 \, H^i \, \frac{F(\phi)}{F(90)}$$

where $\hat{a}_T$ is unit vector on the surface perpendicular to the slot.

The ripple on the pattern $F(\phi)$ is caused by the edge diffraction effect and its magnitude represents a measure of the inaccuracy of the assumption that $\bar{J} = 2\hat{n} \times \bar{H}^i$. However a smooth curve through the actual pattern should reduce this error to a fraction of a dB. A second calibration point is available in this case. For incidence at $\phi = 0$, the magnetic field intensity is $\frac{1}{2}(H^i+H^2)$ where $H^2 = H^i$ thus giving

(40) $$\bar{J} = \hat{a}_T \, H^i \, \frac{F(\phi)}{F(0)} \quad .$$

A similar approximate evaluation can be made of the electric current density for any thin linear slot on a conducting surface. Usually the calibration should be taken near the pattern maximum. A similar analysis will be made of a stub or monopole antenna mounted on a conducting surface. In this case, the calibration will be more difficult to obtain but it still appears to be practical.

The preceding discussion involves only infinitesimal antenna elements. There is a vast body of data available for finite antennas. This data can be calibrated in the manner discussed above to obtain a crude estimate of the surface current density and charge, the principle source of error being the directivity of the antenna. These results are also useful for the introduction of the techniques to be used. Later, a comparison is to be made of the actual surface current and charge density and values obtained with the finite antenna.

The problem of a source on a strip has been examined by Burnside[14]. The pattern is calculated by summing the direct ray

from the source for aspects where the source is visible with the diffracted rays from the two edges. The computed results are shown in Fig. 10.

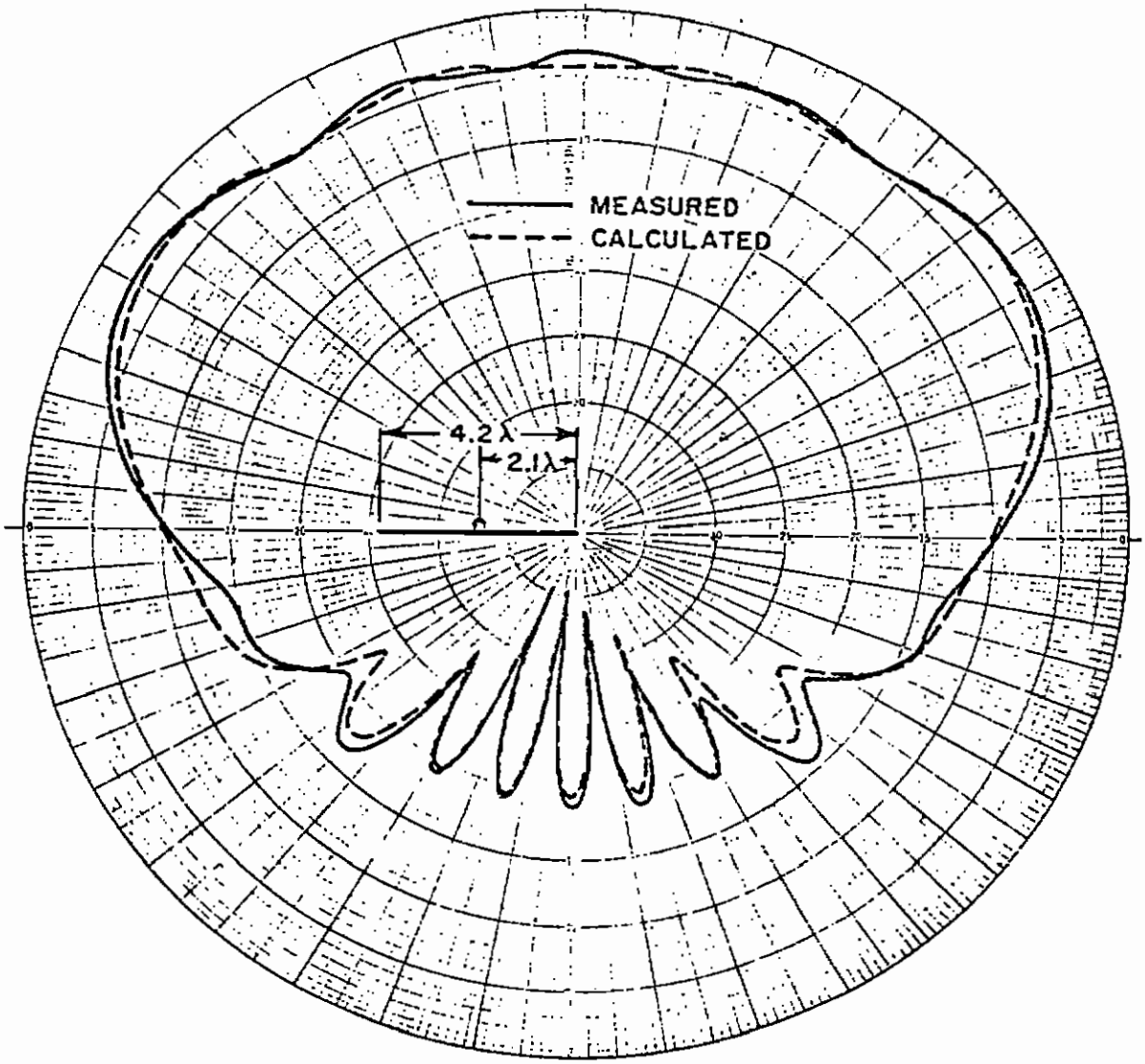

Fig. 10. Radiation pattern of a slot mounted on a finite ground plane.

Using diffraction theory Balanis and Peters[15] have calculated the radiation patterns of axial and circumferential slots in cylinders. One is tempted to relate these results to the surface current density merely by setting the pattern value at $\phi = 0°$ to $2\hat{n} \times \overline{H}^i$ as discussed previously. However, these are thick slots in terms of wavelength and this would be a crude approximation. These results are to be discussed, however, to demonstrate the techniques which can be applied to other geometries. Note that the coordinate system has now been selected so that $\phi = 0$ corresponds to the angle of maximum radiation. The geometry for the TEM excited axial slot is shown in Fig. 11. In

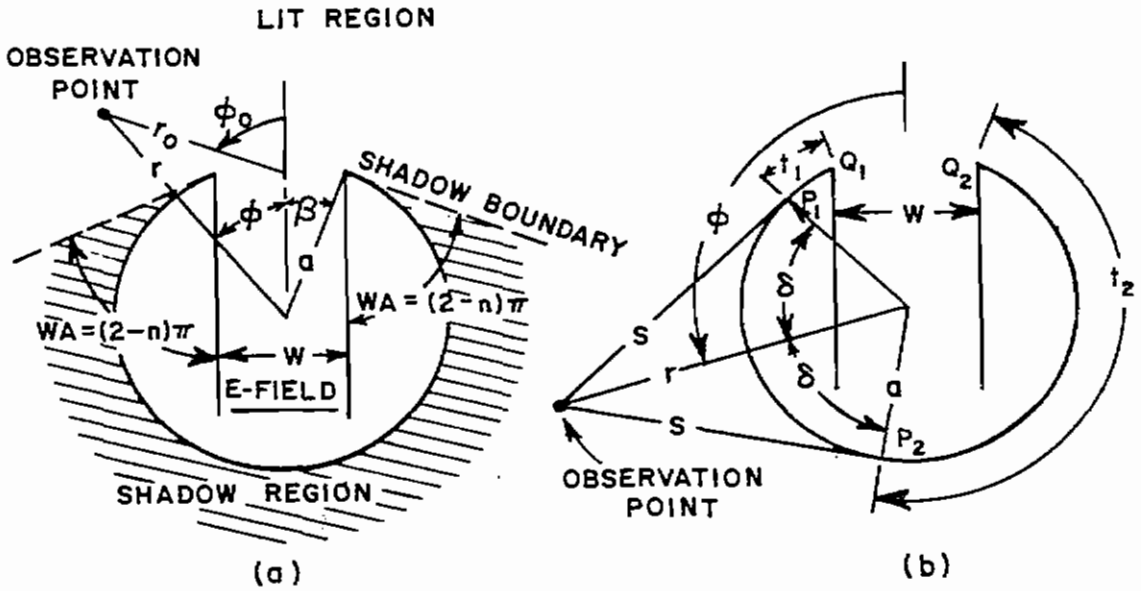

Fig. 11. Axial slot in a circular cylinder.

the lit region, $\sim 90 < \phi > \sim -90°$, the total radiated field is obtained by combining the waves diffracted from the wedges (Q_1 and Q_2) with the creeping waves which encircle the cylinder; while in the shadow region only the creeping waves launched at Q_1 and Q_2 contribute to the radiated field. The results for circular cylinders are compared with the exact solution in Figs. 12 and 13. The advantage of the GTD

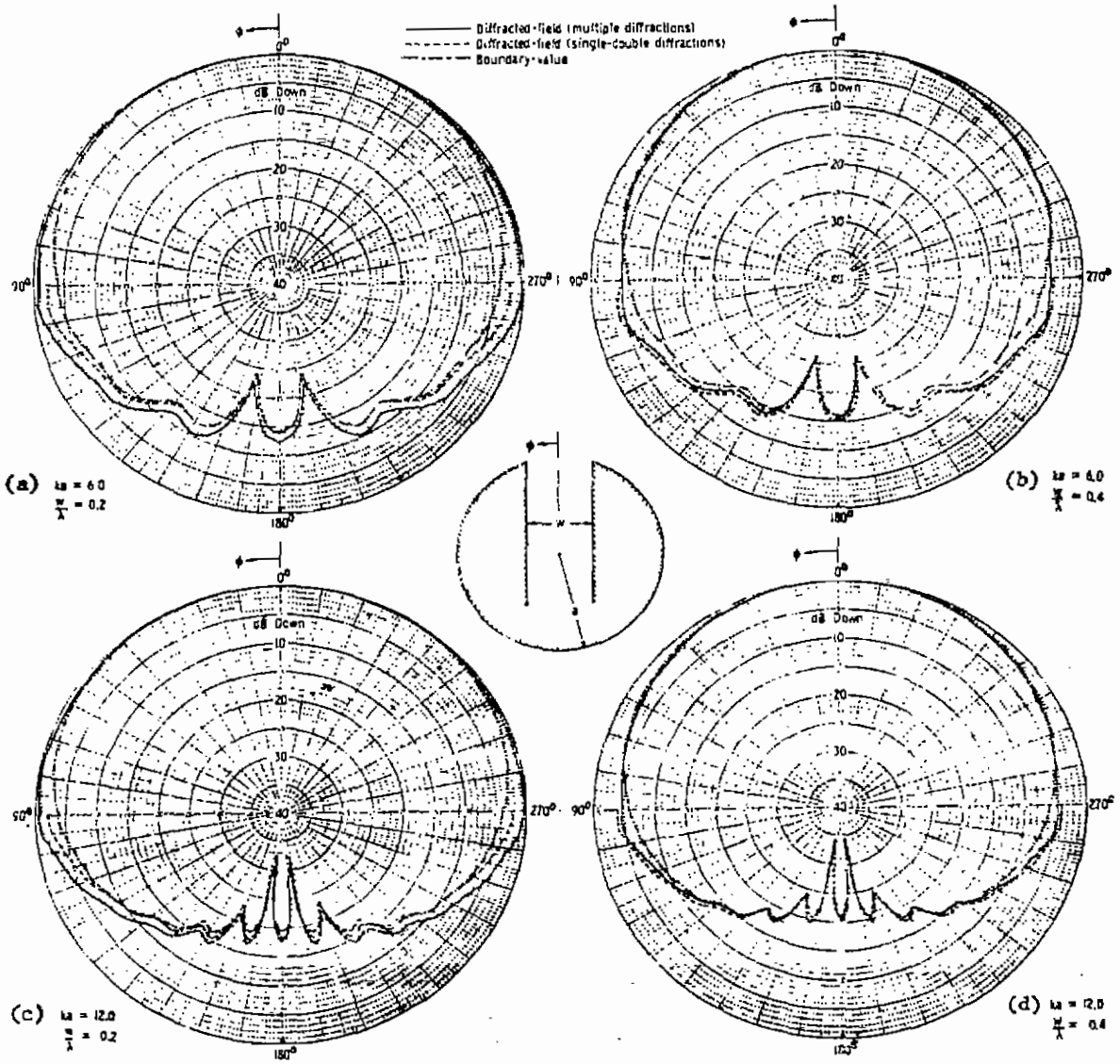

Fig. 12. Radiation patterns of axial infinite slot on circular conducting cylinder (TEM-mode).

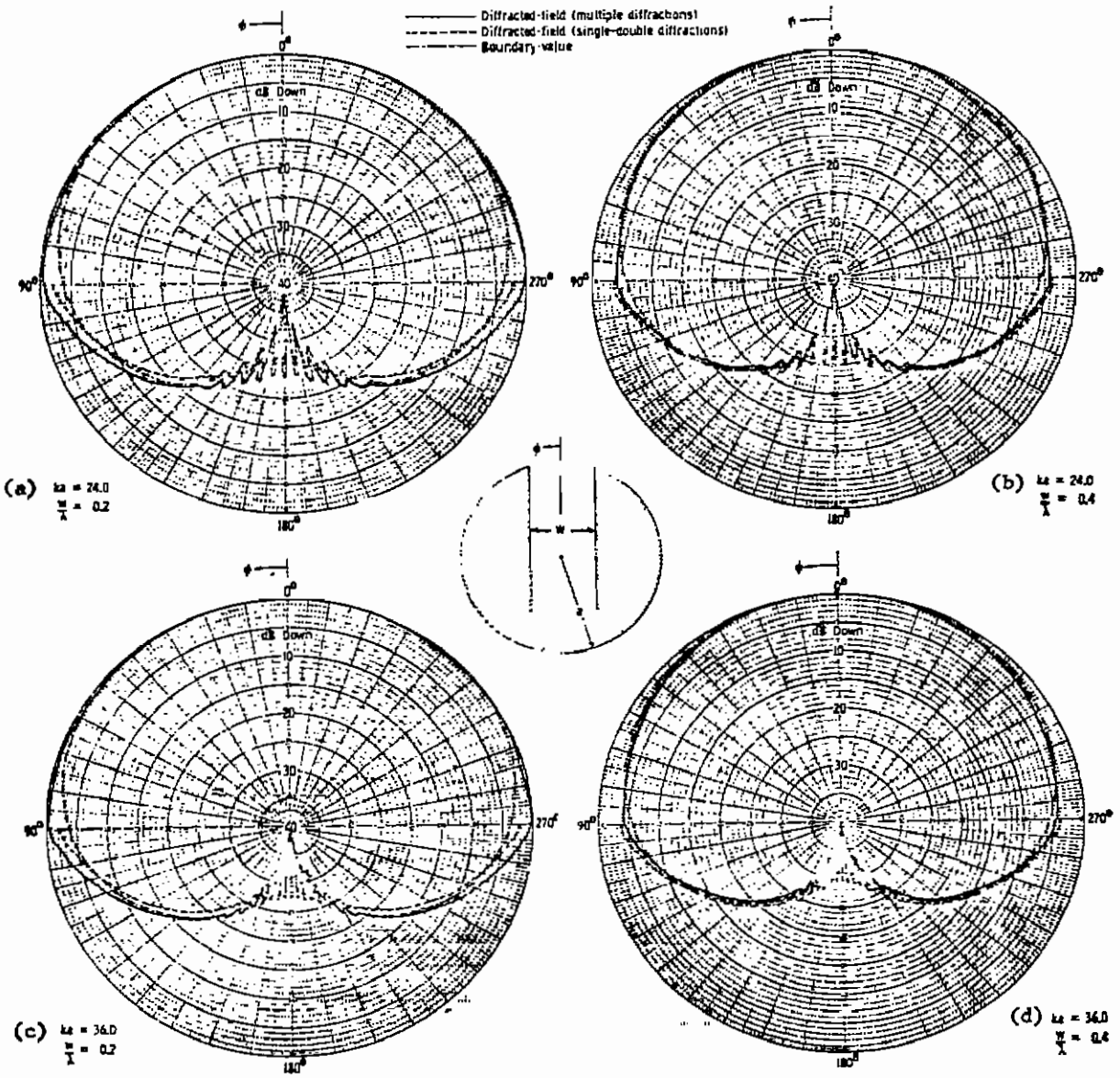

Fig. 13. Radiation patterns of axial infinite slot on circular conducting cylinder (TEM-mode).

solution is that as the body becomes larger the computation time using GTD is far shorter than that required for the exact solution and the GTD solution may be extended to shapes for which no exact solution is available. The approximation used by Balanis and Peters give good results except near the shadow boundary where the solution which includes only the first and second order diffracted fields has a discontinuity. Even when the multiple diffractions (wedge-wedge interactions) are accounted for, there is still some error near the shadow boundary but the fields are continuous. A recent advance by Pathak and Kouyoumjian to be discussed later eliminates this small region of descrepancy. In addition to slots on circular cylinders, Balanis and Peters have also investigated axial slots in eliptical cylinders, Fig. 14, using methods very similar to the analysis for

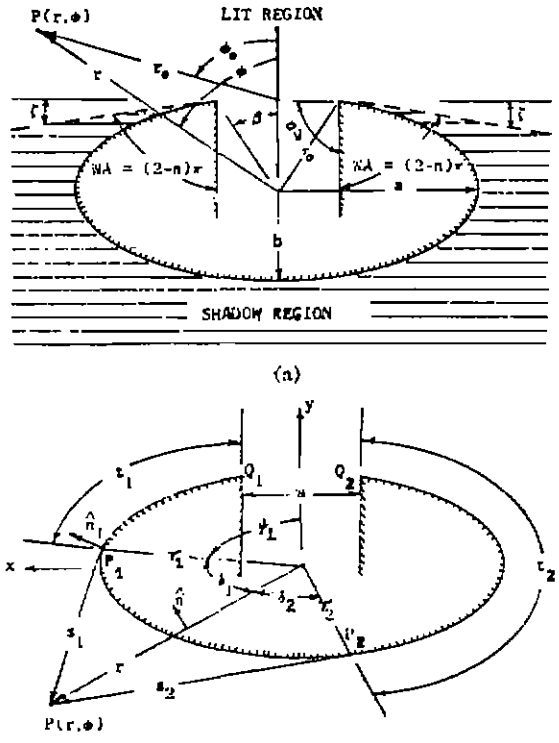

Fig. 14. (a) Elliptical cylinder geometry.
(b) Creeping-wave radiation mechanism.

the circular cylinders. The main difference is that the creeping wave components are harder to evaluate since the propagation constant varies with position on the body and hence an integration is required over the arclength of the creeping wave paths, such as the paths Q_1, P_1, P and Q_2, P_2, P shown in Fig. 14(b). The results of the analysis are shown in Figs. 15 and 16 along with measured data.

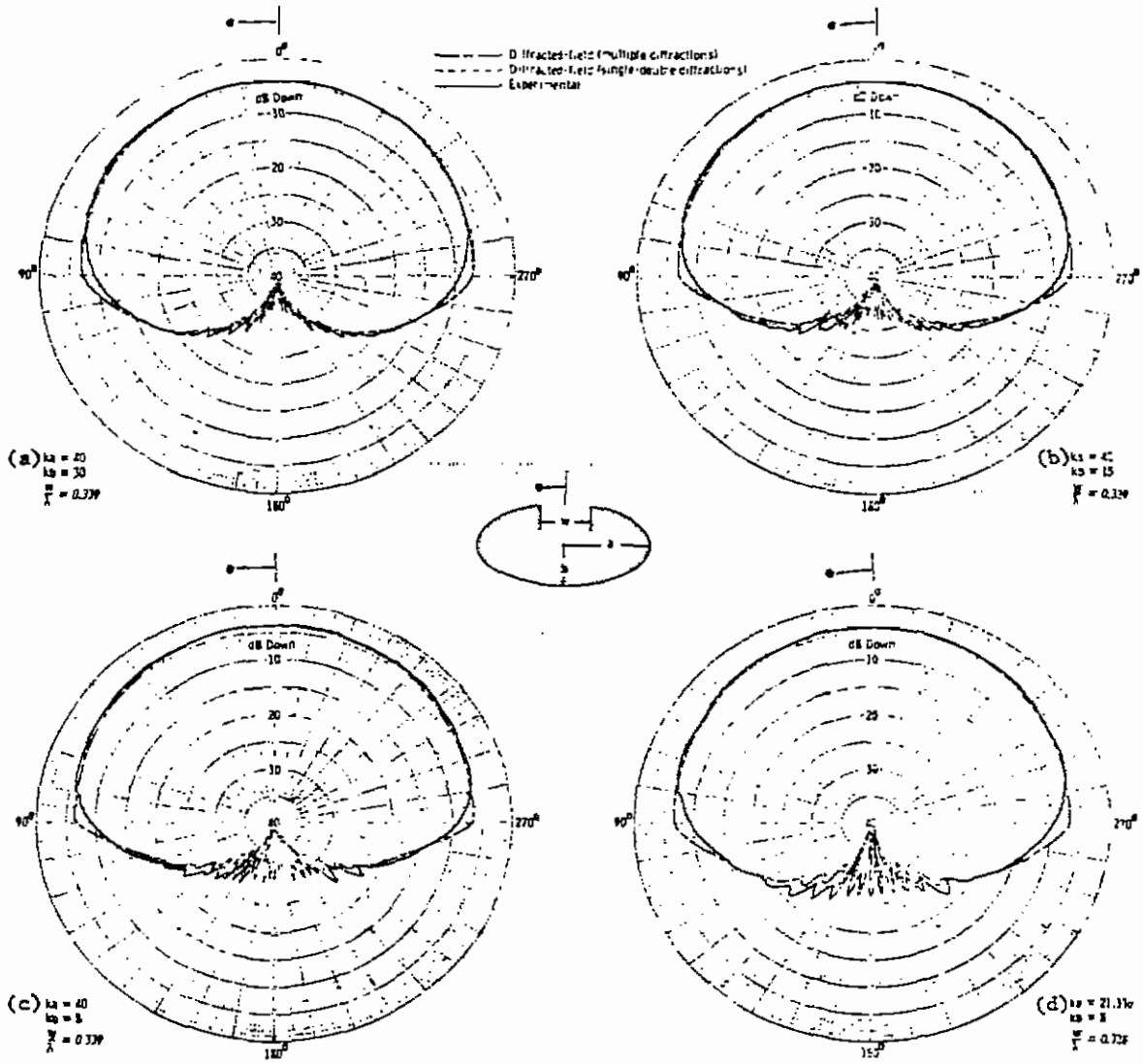

Fig. 15. Radiation patterns of axial slot on elliptical conducting cylinder (TEM mode).

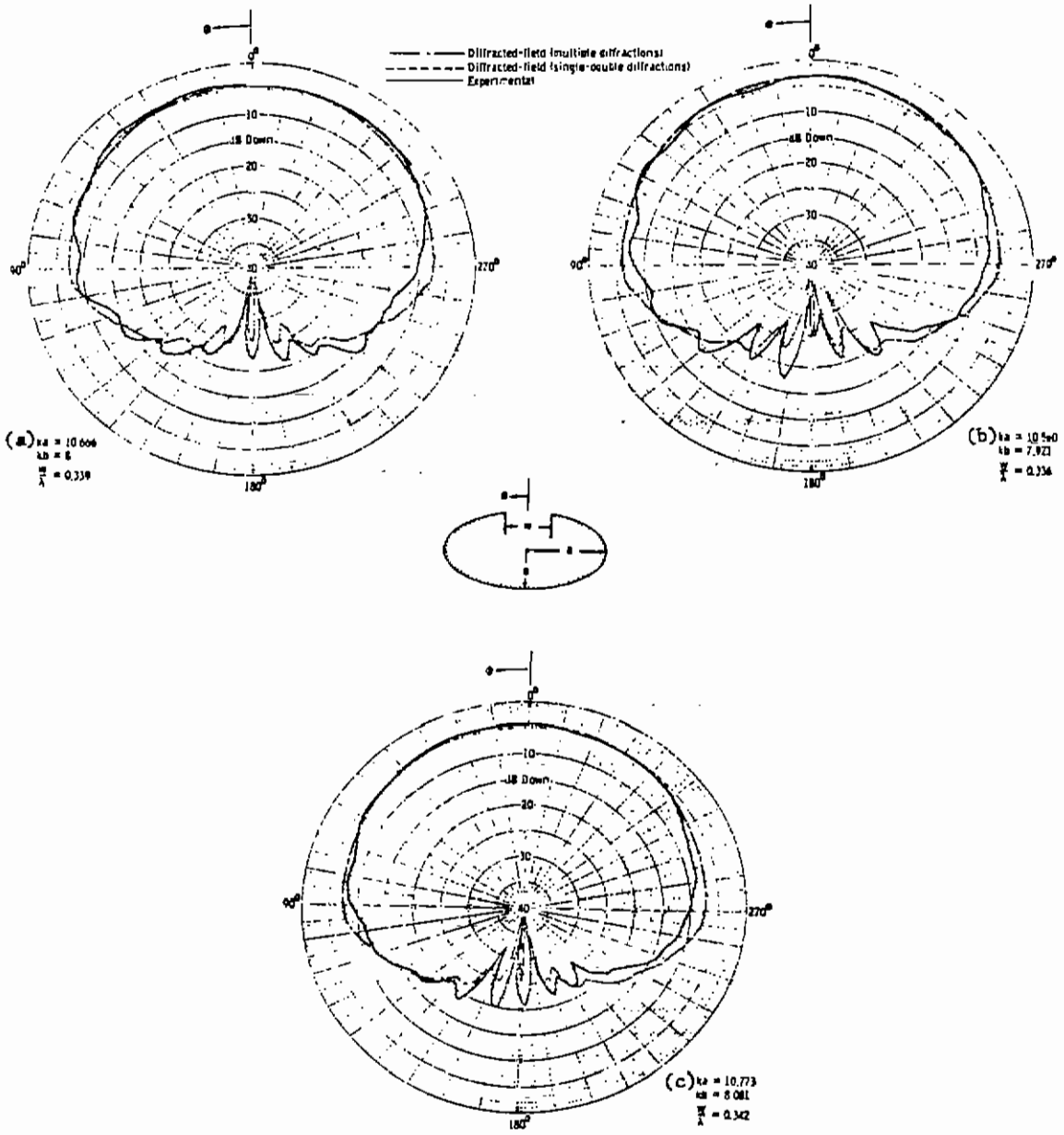

Fig. 16. Comparison of radiation patterns for smaller size elliptical cylinders (TEM mode).

Overall agreement is good especially when the cylinder is large in terms of wavelengths but near the shadow boundaries, $\sim \pm 90$, the fields differ by about 3 dB.

Balanis[16] and Balanis and Peters[17] have also investigated circumferential slots on cylinders of finite length using a two dimensional model as shown in Fig. 17. This is called the "square

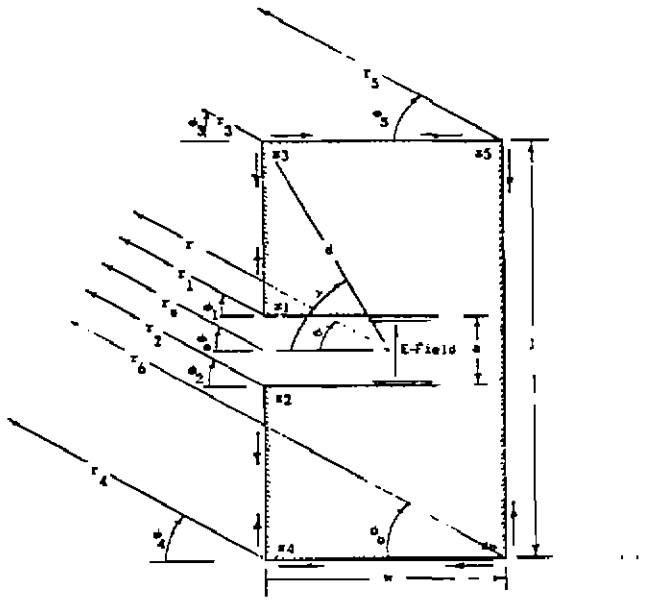

Fig. 17. Diffraction mechanism geometry for finite width and length ground plane.

cylinder approximation." A TEM wave in the guide impinges upon the 90° wedges formed by the guide wall and the surface of the block. Wedges 1, 2, 3 and 4 are the strongest scatterers while 5 and 6 have a very minor effect on the radiated field if the length and width of the body are greater than a few wavelengths. The multiple interactions between the wedges can be accounted for but once again are negligible if the body is large in terms of wavelengths.

The measurements were made on a slotted finite width ground plane which is the cross section of a slotted cylinder. Fig. 18 shows the calculated and measured patterns for several different guide widths. Note that when the guide is one wavelength wide ($a/\lambda = 1.0$) the pattern has very low backlobes and is ripple free in

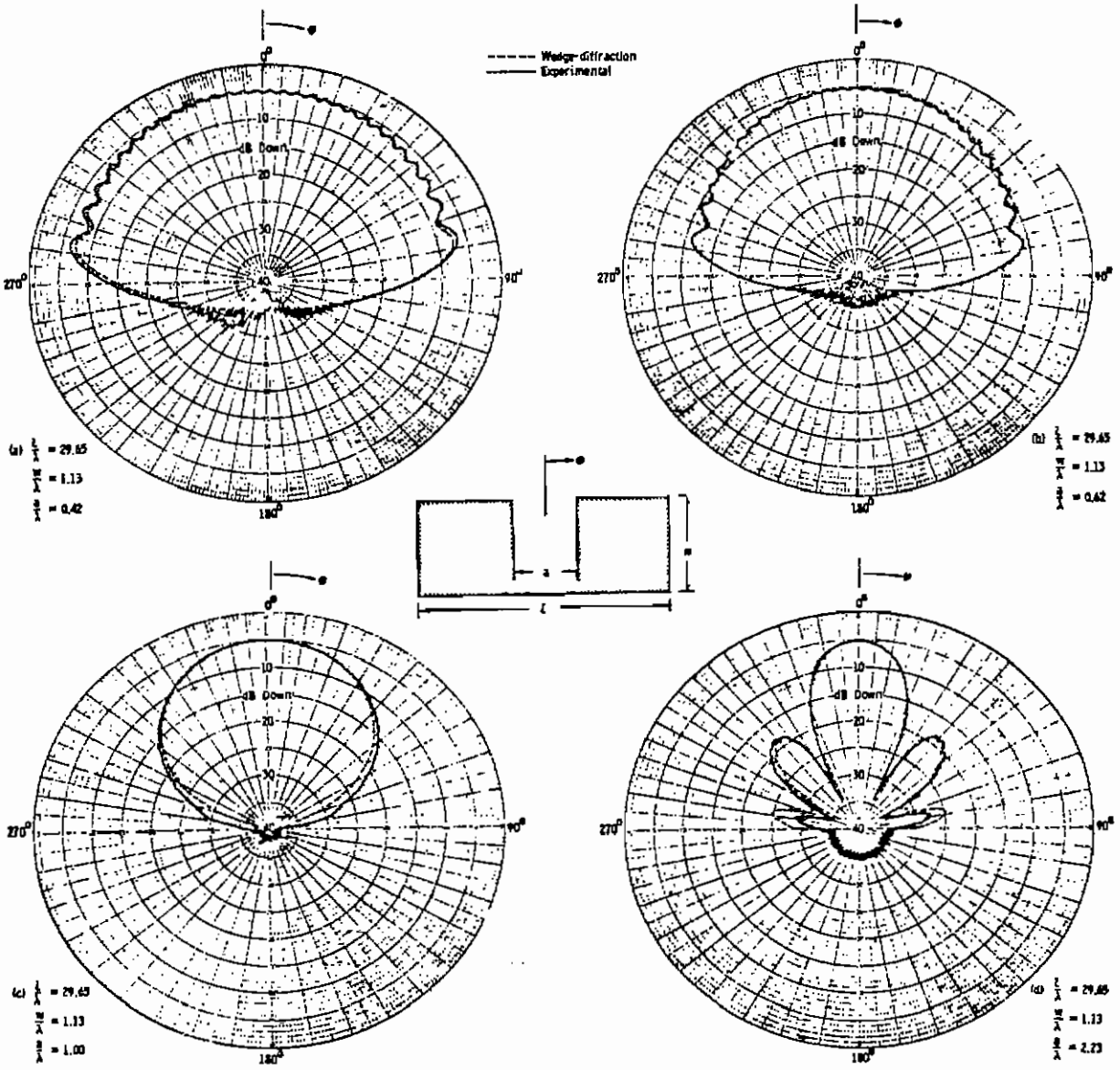

Fig. 18. Radiation patterns of axially slotted ground plane (TEM mode).

the forward direction since the fields diffracted from wedges 1 and 2 (Fig. 17) cancel in the $\theta = \pm 90°$ directions so that wedges 3, 4 are not illuminated

Ryan[18] has extended the analysis of Balanis and Peters[17] by considering a true circular cylinder instead of a "square cylinder" and allowing arbitrary location of either monopoles or slots. The curved edges of the cylinder ends contribute to the radiated field in the following way: A creeping wave is launched from the source along a geodesic path (helical for cylinders) to a point on the edge, where it is diffracted into a cone of rays. Fig. 19 illustrates such a path and cone. When an observer lies on the surface

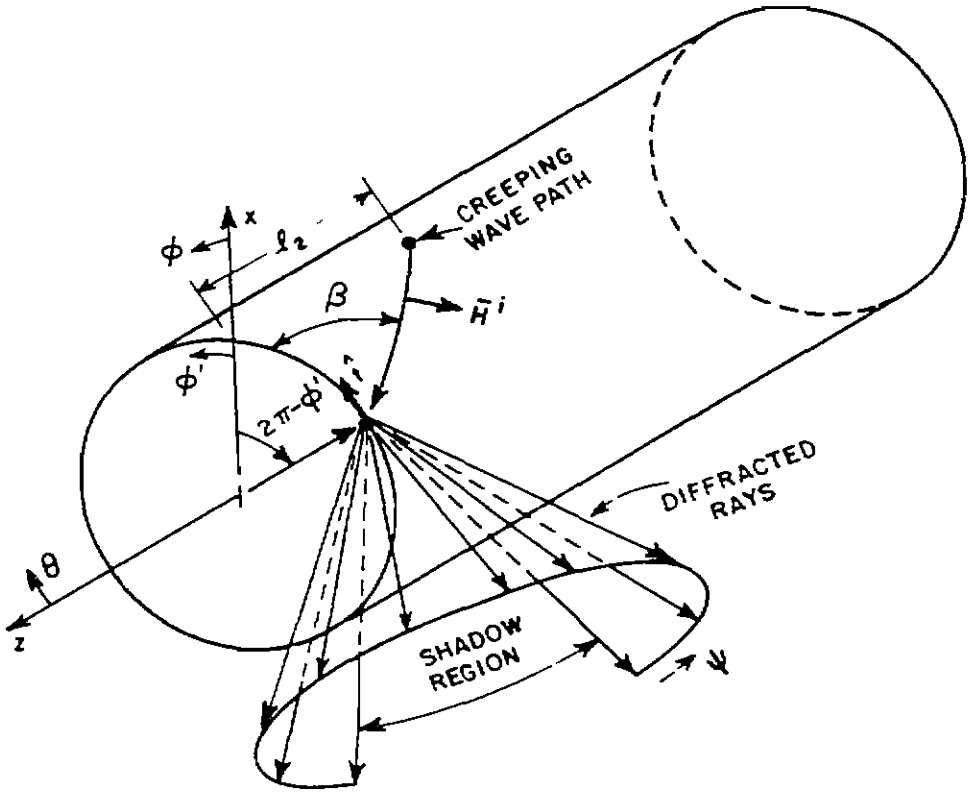

Fig. 19. Diffraction of a creeping wave by the end of a finite circular cylinder.

of one of these cones then Fermat's principle is satisfied and the contribution of that edge diffracted ray must be computed. For an

observer in the XZ-plane (far-field) and at an angle $\theta > 0$ only two points (one on each end of the cylinder) contribute to the diffracted field. For $\theta < 0$ it is possible that a continuum of points on the edge satisfy Fermat's principle as illustrated in Fig. 20. For a

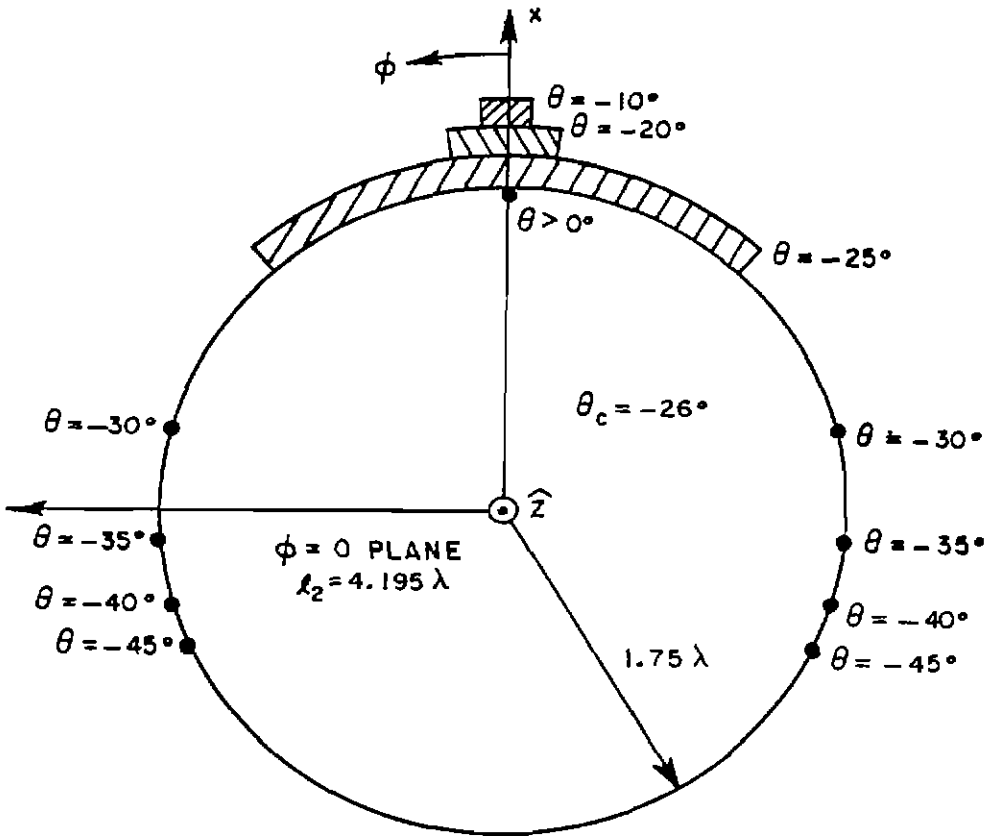

Fig. 20. Points on the end of a finite cylinder which satisfy Fermat's principle.

cylinder of radius 1.75λ, this continuum of points occurs for angles $0 > \theta > \theta_c = -26°$, when such a continuum of points occurs it is necessary to use an equivalent current concept to calculate the diffracted field.

Ryan[18] approximated the value of the creeping wave field as

(41) $$H^{cw} = H_o\, e^{-\gamma S}$$

where H^{cw} is the creeping wave amplitude and phase

H_o is the source strength

$\gamma^2 = (jk\cos\xi)^2 + (jk + \alpha)^2 \sin^2\xi$

$\alpha = 0.84\, a^{-2/3}\, \lambda^{-1/3}\, e^{j\pi/6}$

a = radius of the cylinder

S = arclength from source to diffracting point on edge

and the square root of γ^2 is taken to lie in the first quadrant of the complex plane, when only discrete points on the edge contribute the diffraction from the curved edge may be computed using Reference [19]. When a continum of points contribute to the diffracted field the equivalent current concept[18] is used. Figs. 21 and 22 show the calculated and measured radiation patterns for a $\lambda/4$ monopole mounted on a finite cylinder using the "square cylinder" approach and the equivalent current method. If the source is visible to the observer either method is satisfactory but when the source is not visible to the observer, and hence the radiated field is due entirely to the diffracted fields, the equivalent current method is more accurate. Unfortunately, the computation times for the equivalent current formulation are considerably longer due to the integration which the method requires.

Ryan[18] also calculated the radiation patterns of antennas mounted on conically capped cylinders using the equivalent line current on the cylinder base edge and the cone-cylinder junction. Ryan found that the diffraction due to the cone tip could be approximated (in the elevation plane) by the diffraction from a wedge having the same included angle as the cone. Figures 23 and 24 show the measured

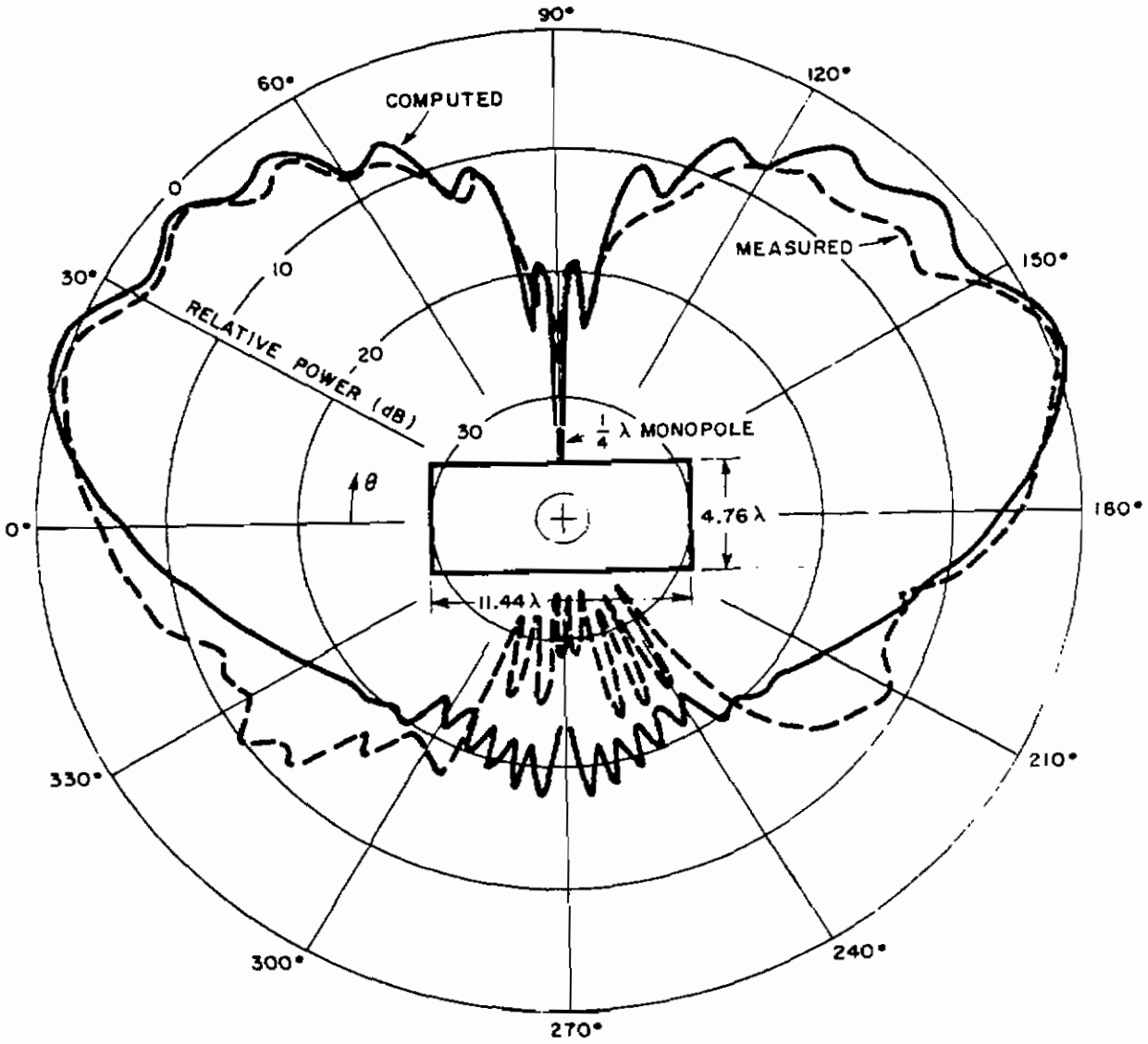

Fig. 21. Calculated and measured patterns for a 1/4 wave monopole at the midpoint of a circular cylinder. (Square cylinder approximation.)

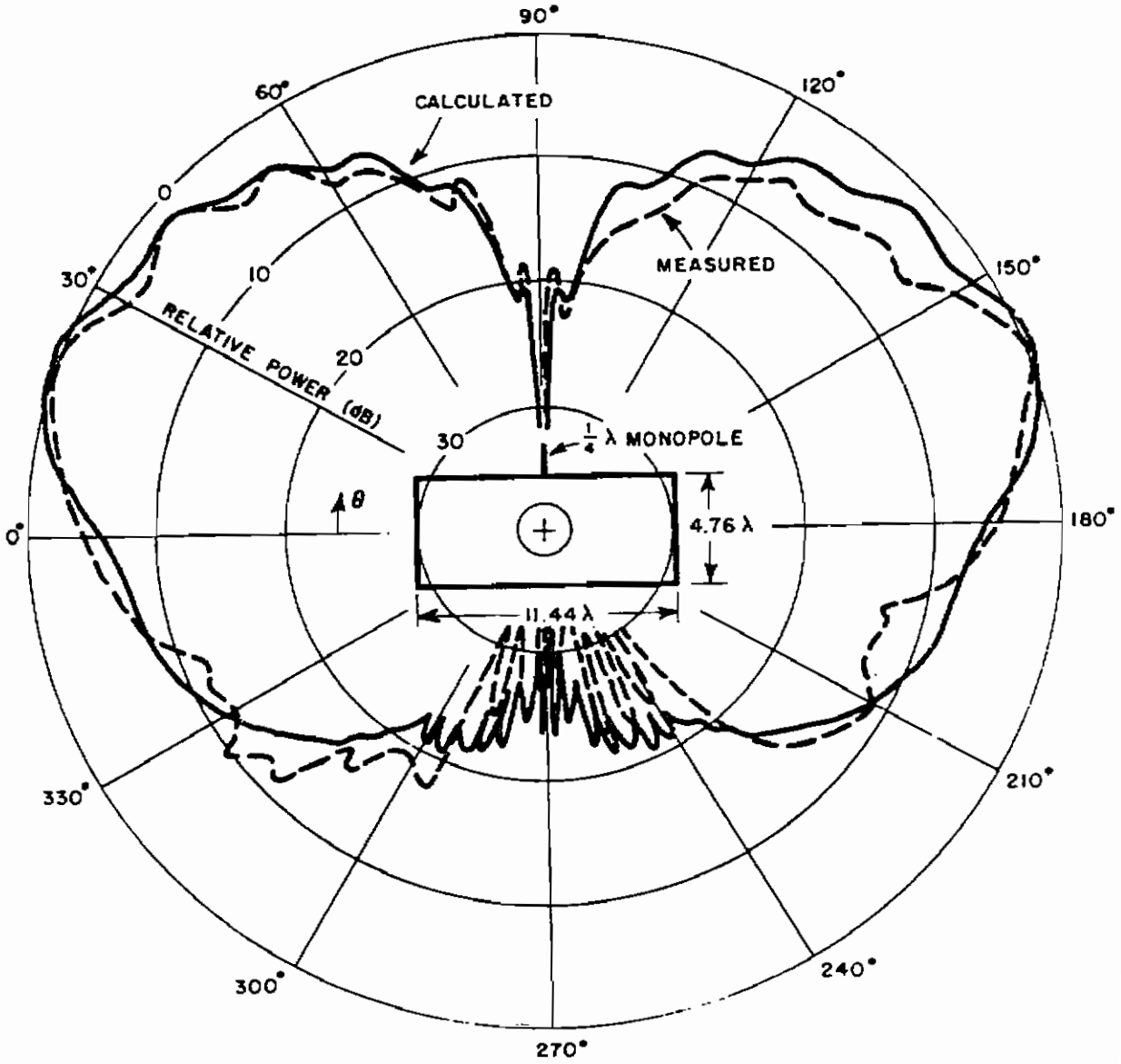

Fig. 22. Monopole at the midpoint of a finite circular cylinder. Equivalent current method.

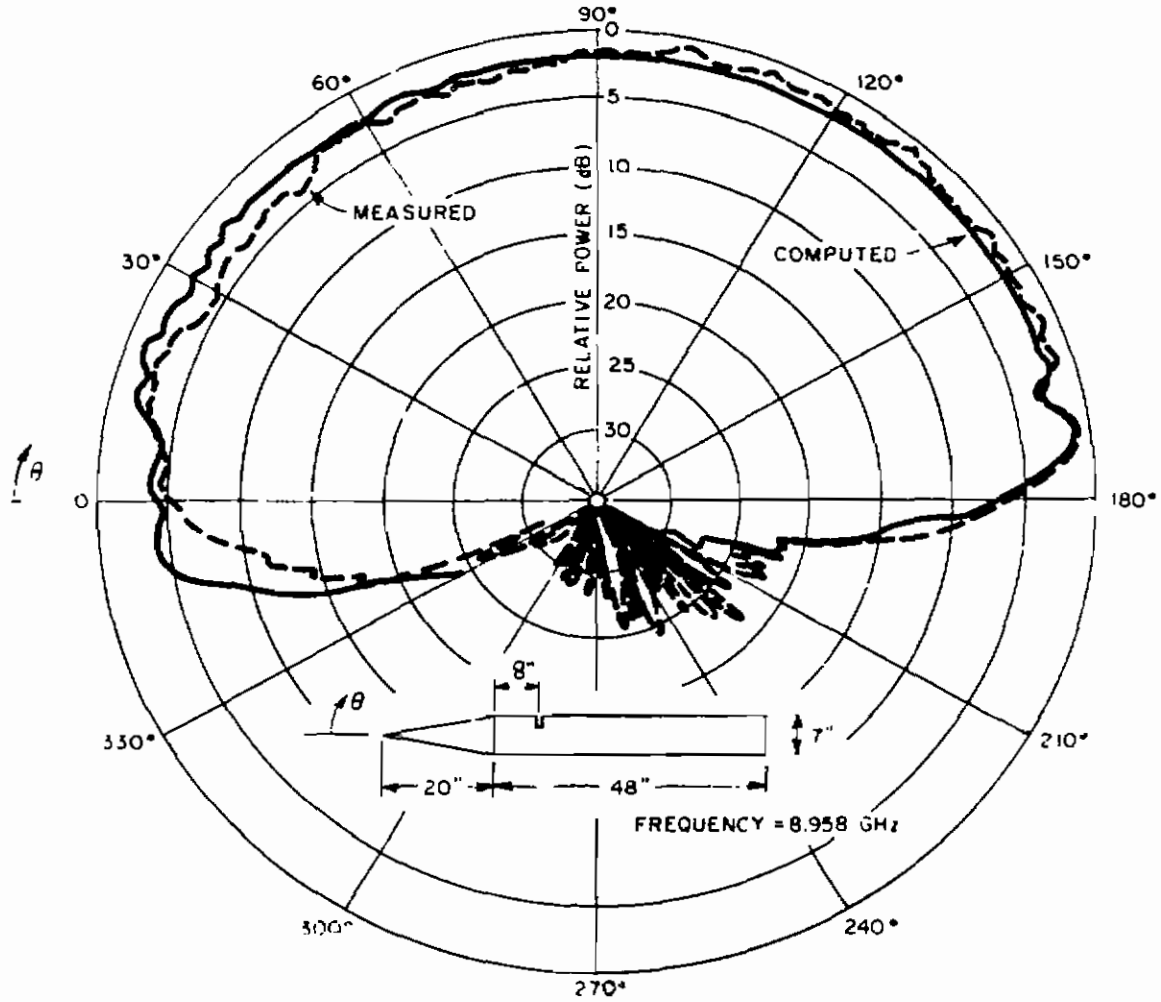

Fig. 23. Radiation pattern of a circumferential slot on a conically-capped finite circular cylinder. Tip neglected cone-cylinder junction included where visible.

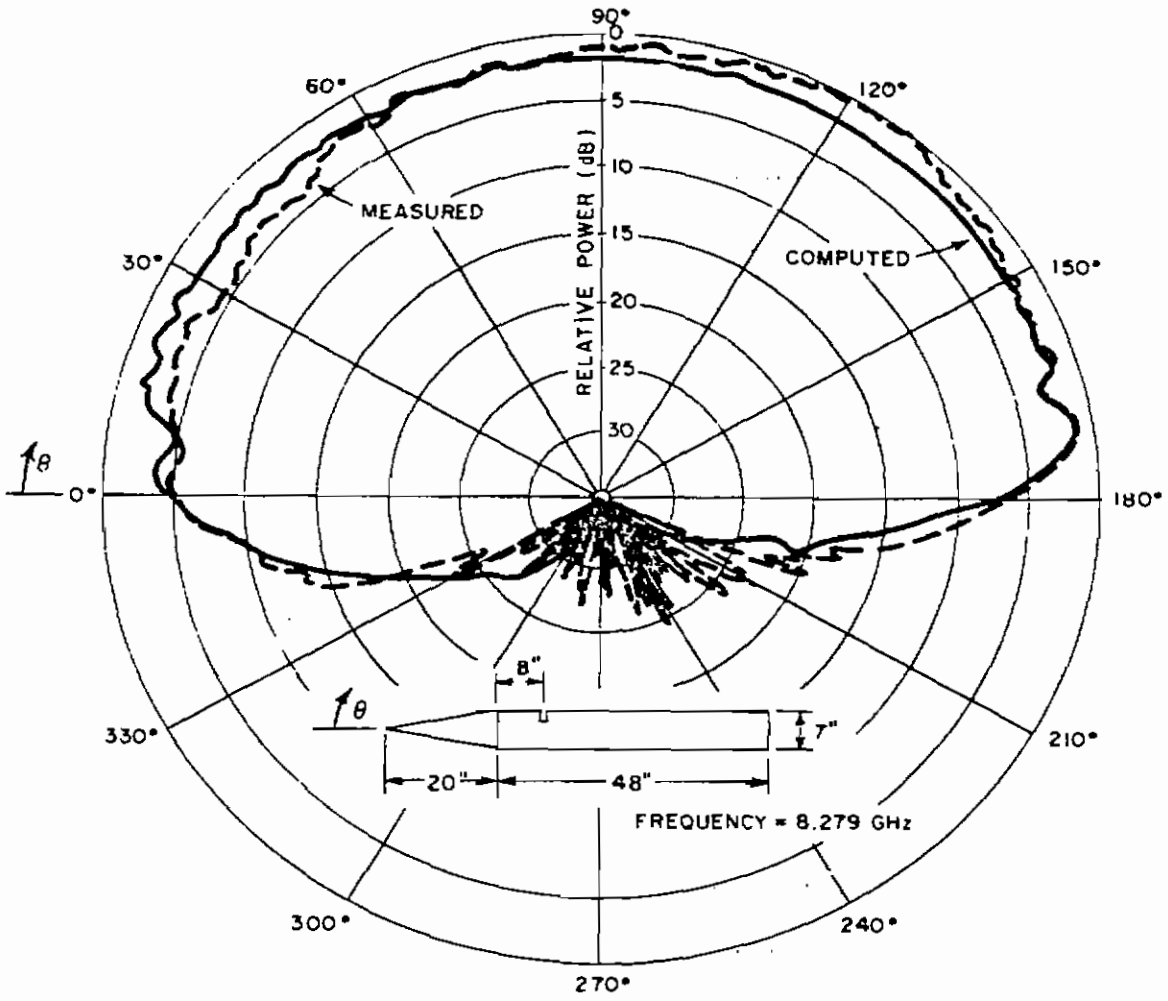

Fig. 24. Radiation pattern of a circumferential slot on a conically-capped finite circular cylinder. Tip diffraction included by using a wedge of same included angle.

pattern of a slot on a conically tipped cylinder and the computed patterns both with and without the tip diffraction component of the radiated field. Improved agreement occurs in the aspect range 330°-360° where the tip diffraction is most important and not swamped out by other strong contributors.

Kouyoumjian and Burnside[20] have recently refined the analysis of another problem of interest, the cylinder tipped half-plane, by including the additional rays shown in Fig. 25(b). Using the attenuation constants and diffraction coefficients given by Voltmer[12] to calculate the contributions of the four ray paths shown in Fig. 25,

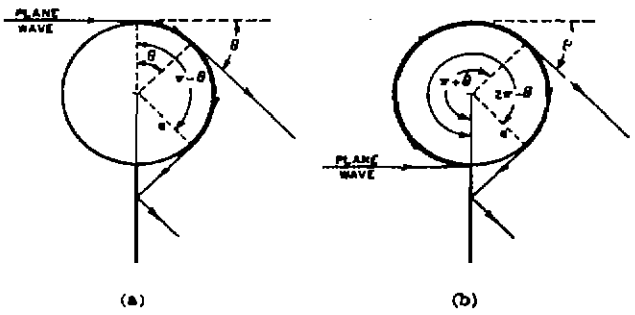

Fig. 25. Cross section of a half-plane tipped with a cylinder of radius a upon which a plane wave is normally incident. (a) Keller's two diffracted ray terms. (b) Our additional diffracted ray terms.

it was found that the ray paths shown in Fig. 25(b) are significant contributors to the diffracted field. The improvement over Keller's solution[21] can be seen in Fig. 26 where the two approximate solutions are plotted along with the exact solution. Having considered the elements of Ray Optical Theory and its application to canonical problems, in the next section we turn to computations involving aircraft like structures.

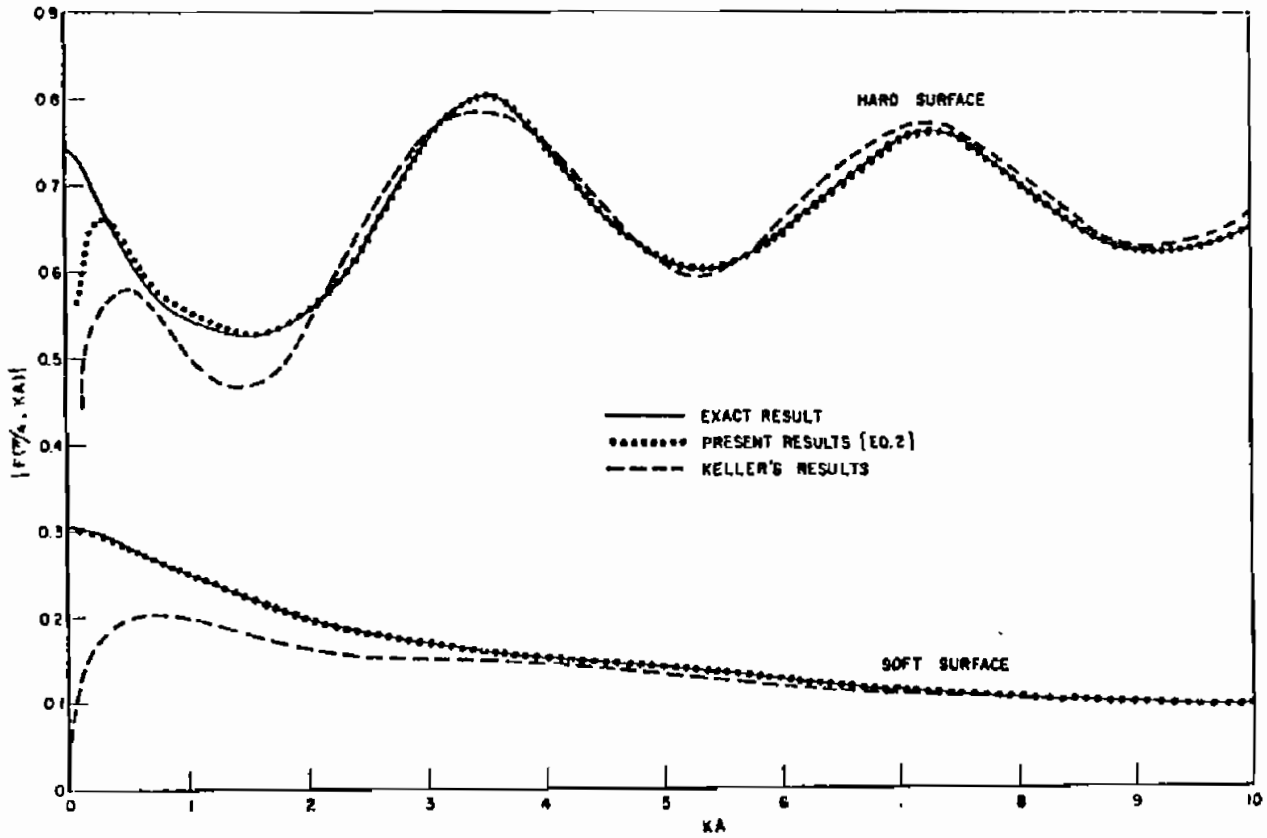

Fig. 26. Magnitude of the diffraction pattern function in the $\theta = \pi/4$ direction from a cylinder-tipped half-plane versus cylinder radius.

III. SURFACE CURRENT AND CHARGE DENSITIES INDUCED ON AIRCRAFT-LIKE BODIES

Most of the results shown in this section are obtained from calculated values of the normal electric and tangential magnetic fields intensities computed at the observation point for plane wave illumination. The surface current density and charge ($\overline{J} = \hat{n} \times \overline{H}$ and $\rho = \varepsilon\ (\hat{n} \cdot \overline{E})$ can readily be obtained from these fields. The patterns to follow have been obtained from these field quantities by forming

$$\int_{Q}^{L} \overline{E} \cdot \overline{I}(\ell)\, d\ell$$

or

$$\int_{O}^{W} \overline{H} \cdot \overline{M}(\omega)\, d\omega$$

where $I(\ell)$ and $M(\omega)$ are the source distribution of the antenna. This last step now makes comparison between theory and experiment practical but makes the interpretation as surface charge and current density approximate. Computations have also been made that do not include this last step to give the surface current and charge density but these results cannot be compared with experiment. The results in general show that accurate evaluation of the surface charge and surface current density computations are possible using the GTD approach.

Yu and Burnside[22] and Marhefka[23] have made measurements of the signal levels received by antennas mounted on an aircraft fuselage in the plane of symmetry containing the vertical stabilizer and compared these measurements with the predictions obtained using diffraction theory combined with modal analyses of References [24] and [25]. The simplified model of the aircraft is shown in Fig. 27 and

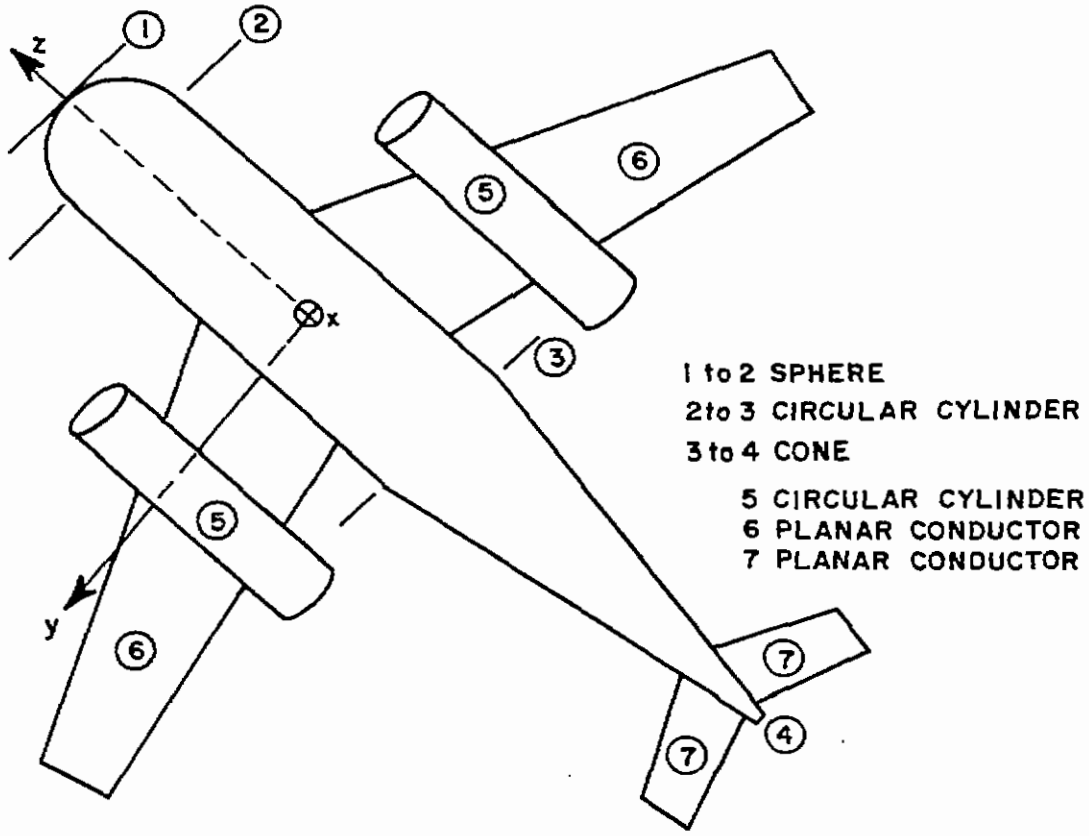

Fig. 27. Simplified aircraft model.

is made up of hemispheres, truncated cones, circular cylinders and planar conductors. The receiving patterns have been confined to the principal planes and the computations made using diffraction methods presume that the structure is large in terms of electrical wavelength. In the following sections, the computational methods used will be discussed and compared to measurements. The measurements are of the antenna patterns for slots and monopoles at the observation point.

A. Roll Plane Analysis

The solution for the pattern in the roll plane of the simplified aircraft model shown in Fig. 28 was obtained using the

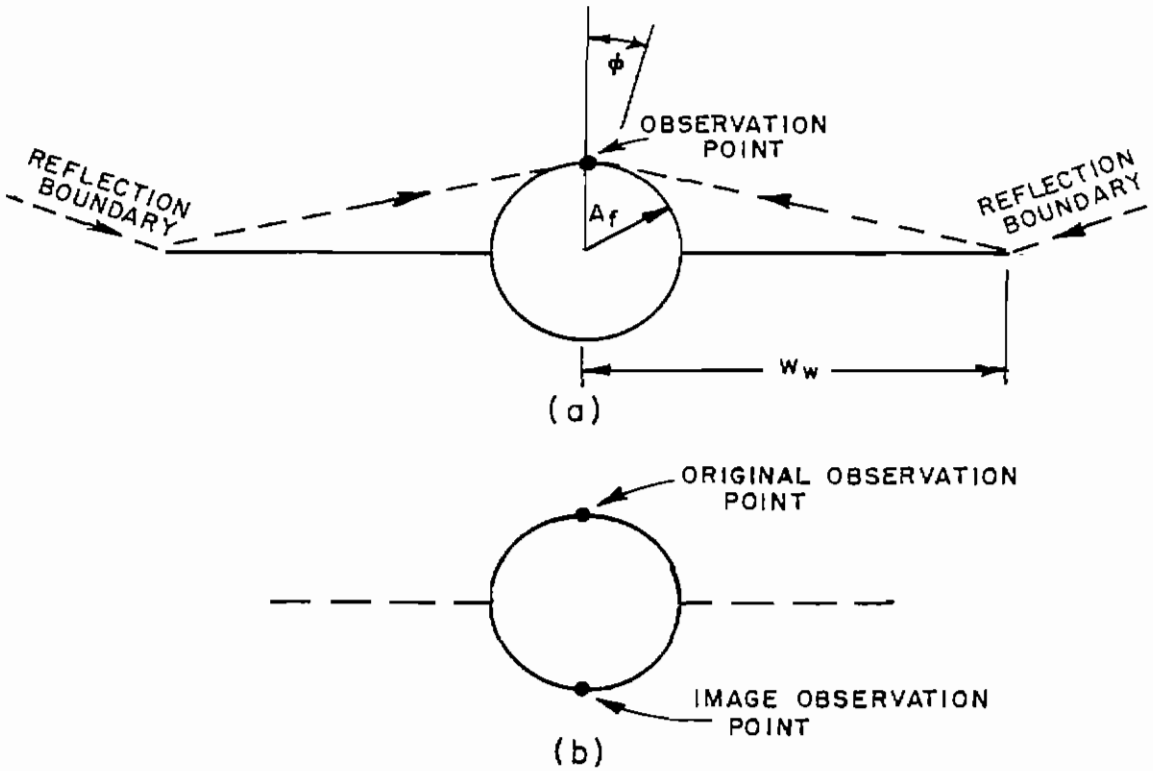

Fig. 28. Roll plane aircraft model.

modal solutions for the scattered fields from infinite cylinders given in Reference [26] and the geometrical theory of diffraction. For roll plane aircraft geometry all aspects out to the reflection boundary (Fig. 28(a)) image theory is used to calculate the received fields. The fields incident upon the observation point and its image are calculated using the appropriate modal solution from Reference [26]. The fields diffracted from the wingtips to the observation point on the surface are also included for these aspect angles (between the

reflection boundaries) even though they are relatively small. The computations for the wingtip diffracted rays proceed as follows: the geometry of Fig. 28 is replaced by that of Fig. 29. The amplitude

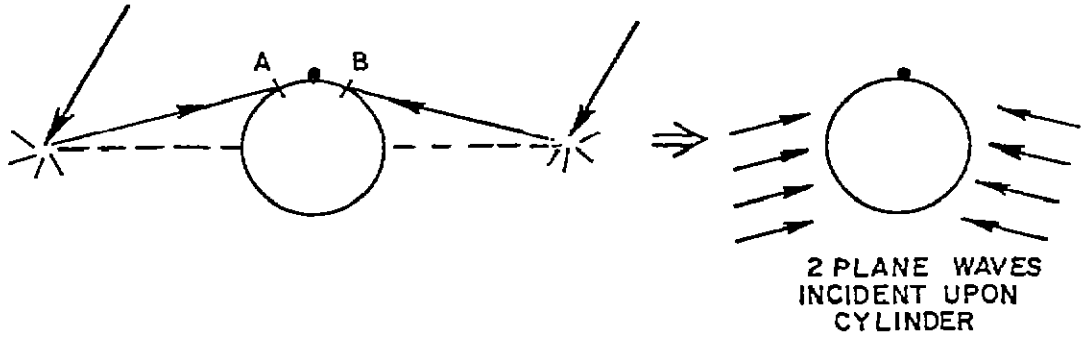

Fig. 29. Wing tip diffracted rays.

and phase of the incident plane waves are taken to be that predicted by diffraction theory at the points of tangency to the cylinder (marked A and B in Fig. 29). Once the amplitude and phase of the incident plane waves are known the modal solutions of Reference [26] are used to calculate the field at the observation point.

For aspects outside the reflection boundaries the major contributors to the received field strength come from a direct ray (when such a path exists) and two wingtip diffracted rays as shown in Fig. 30. The calculated and measured patterns for the three types

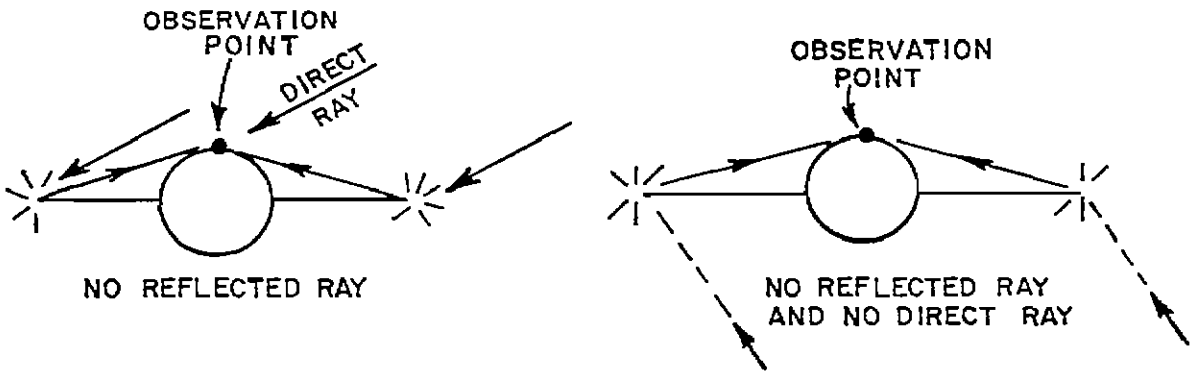

Fig. 30. Receiving mechanisms for various aspects.

of antennas are displayed in Figs. 31-33. The monopole is $\lambda/4$ long and the slots are standard X-band guide.

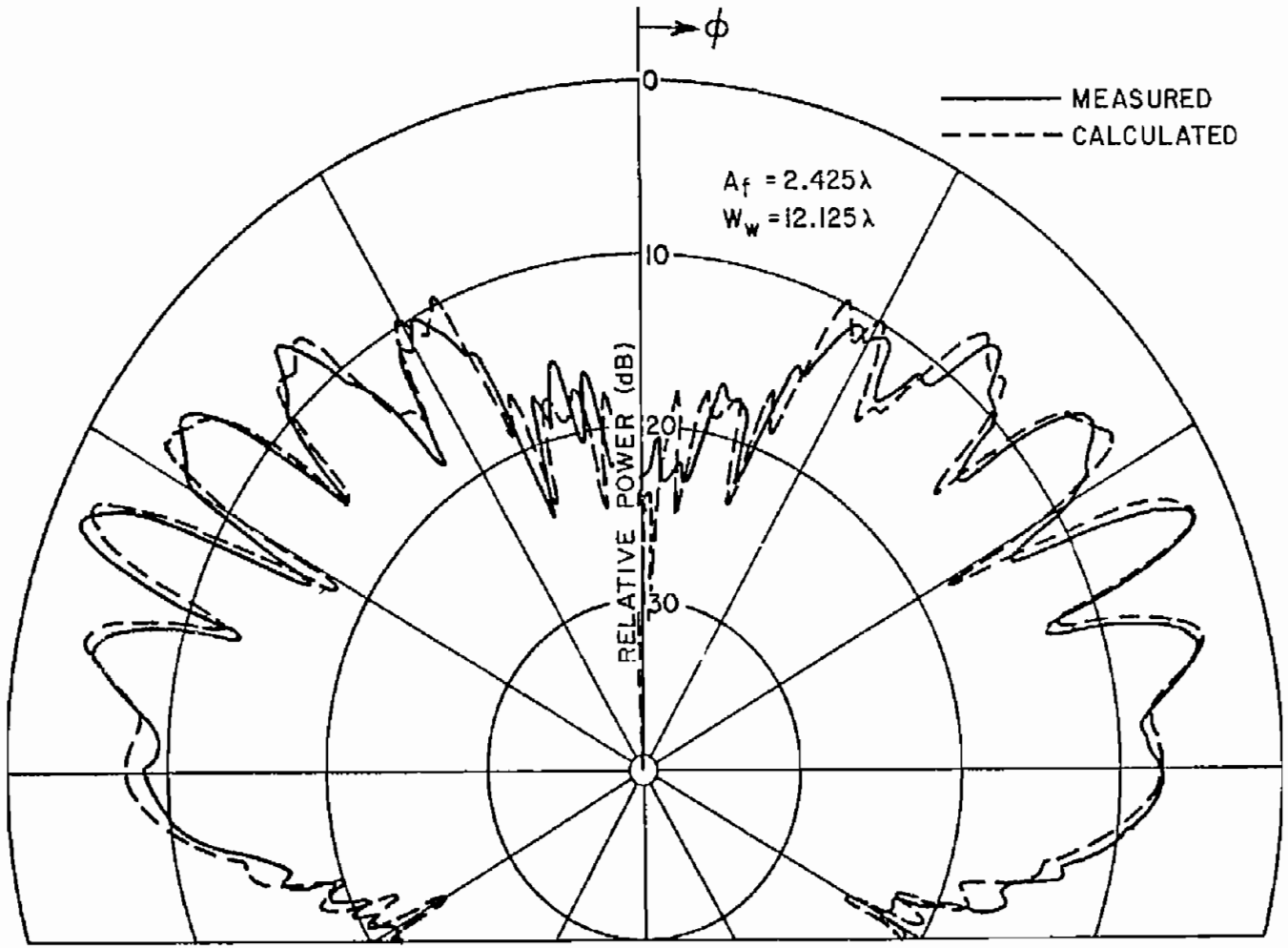

Fig. 31. Roll plane patterns.

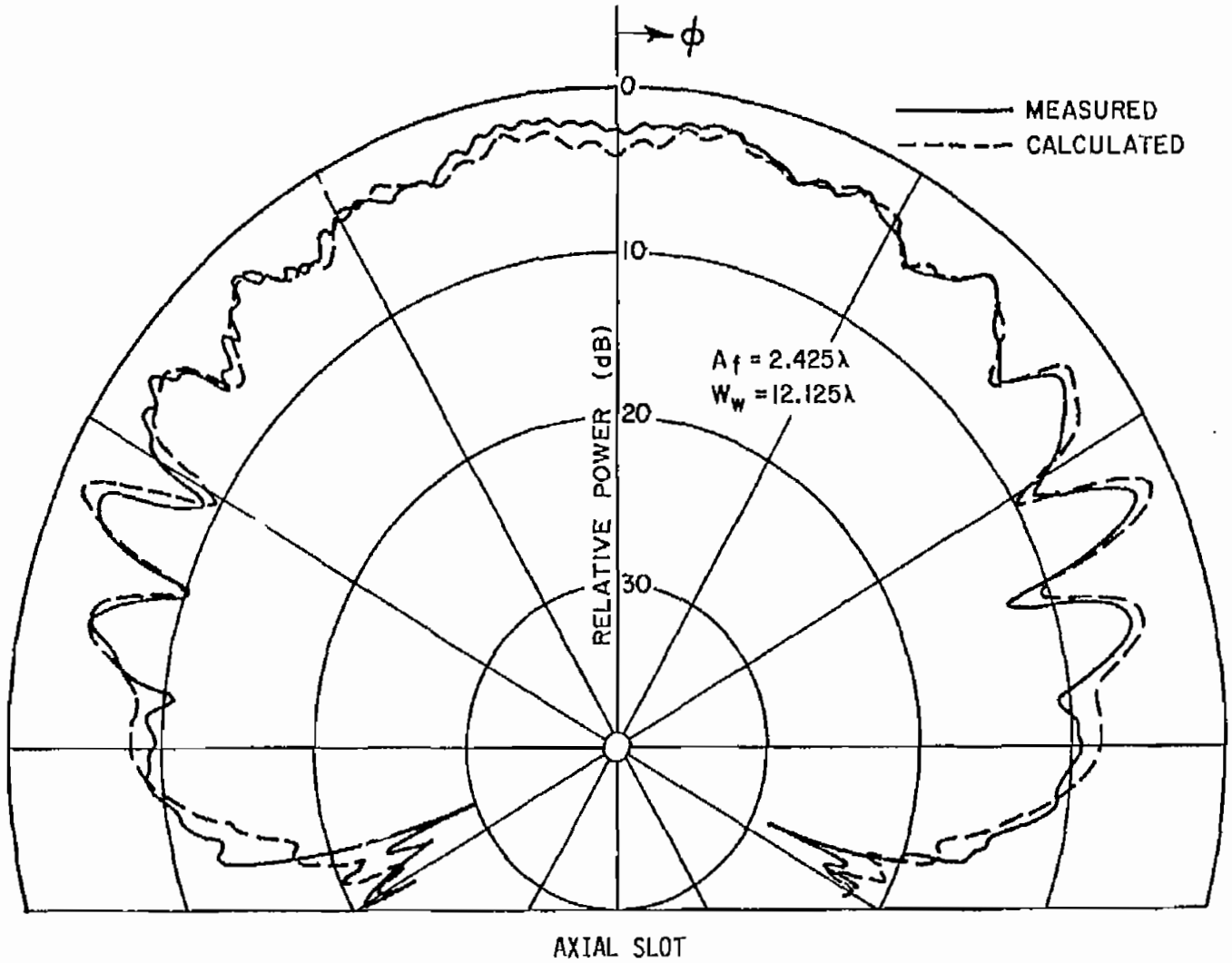

Fig. 32. Roll plane patterns.

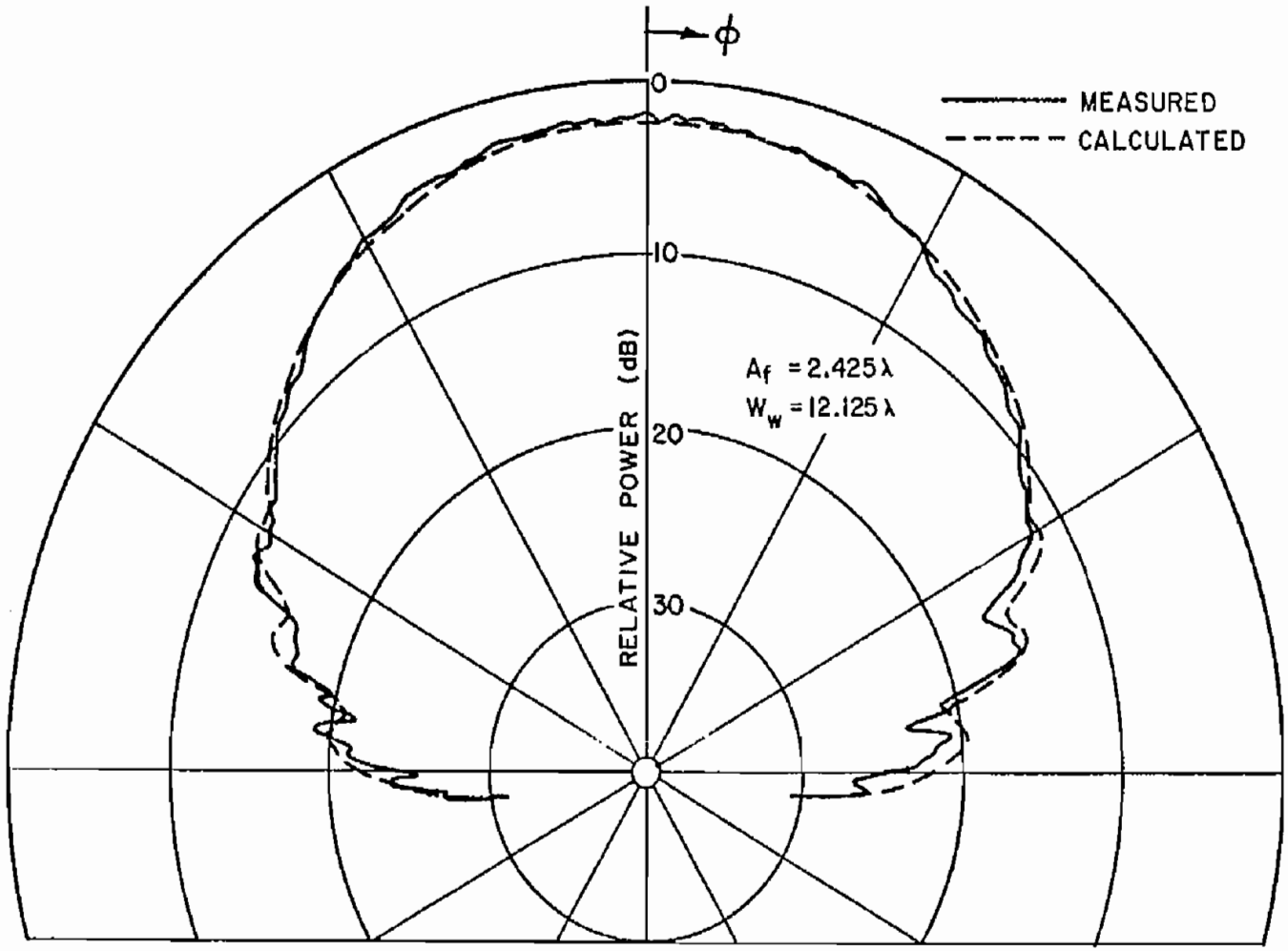

Fig. 33. Roll plane pattern.

The effect of the engines on the roll plane pattern was analyzed using the model of Fig. 34. For all aspects out to the reflection

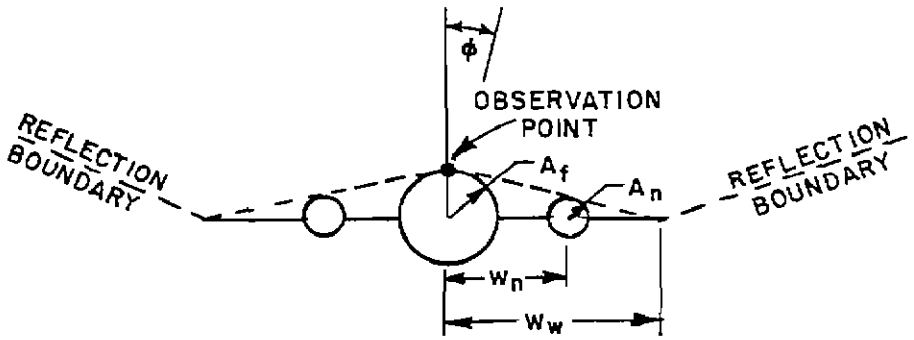

Fig. 34. Aircraft with engines.

boundaries the received fields are computed using image theory, edge diffraction from the wingtips and the modal solution for the scattering from the cylinders which represent the engines. As before, beyond the reflection boundaries only the direct ray (where it exists) and the wingtip diffractions are considered. The measured and the computed results agree very well as shown in Figs. 35-37.

The effect of a three dimensional wing, as shown on the inset of Fig. 38, was accounted for by using the geometrical theory of diffraction. As explained in Section II, a ray obliquely incident on an edge is diffracted into a cone of rays with the edge as the cone axis and the point of incidence as the apex of the cone. The point(s) on the edge(s) of the wing(s) contributing to the roll plane received field are found by iteration along the edges of the wings until the geometry is such that a ray is diffracted in the direction of the observation point. In order to determine the position of these points (if any exist) a creeping wave geometry is considered as shown in Fig. 39. When a point is located which satisfies the geometrical considerations then the incident field at the point of tangency is computed using edge diffraction theory. The creeping wave visualization of the problem, while satisfying Fermat's principle, is not used for

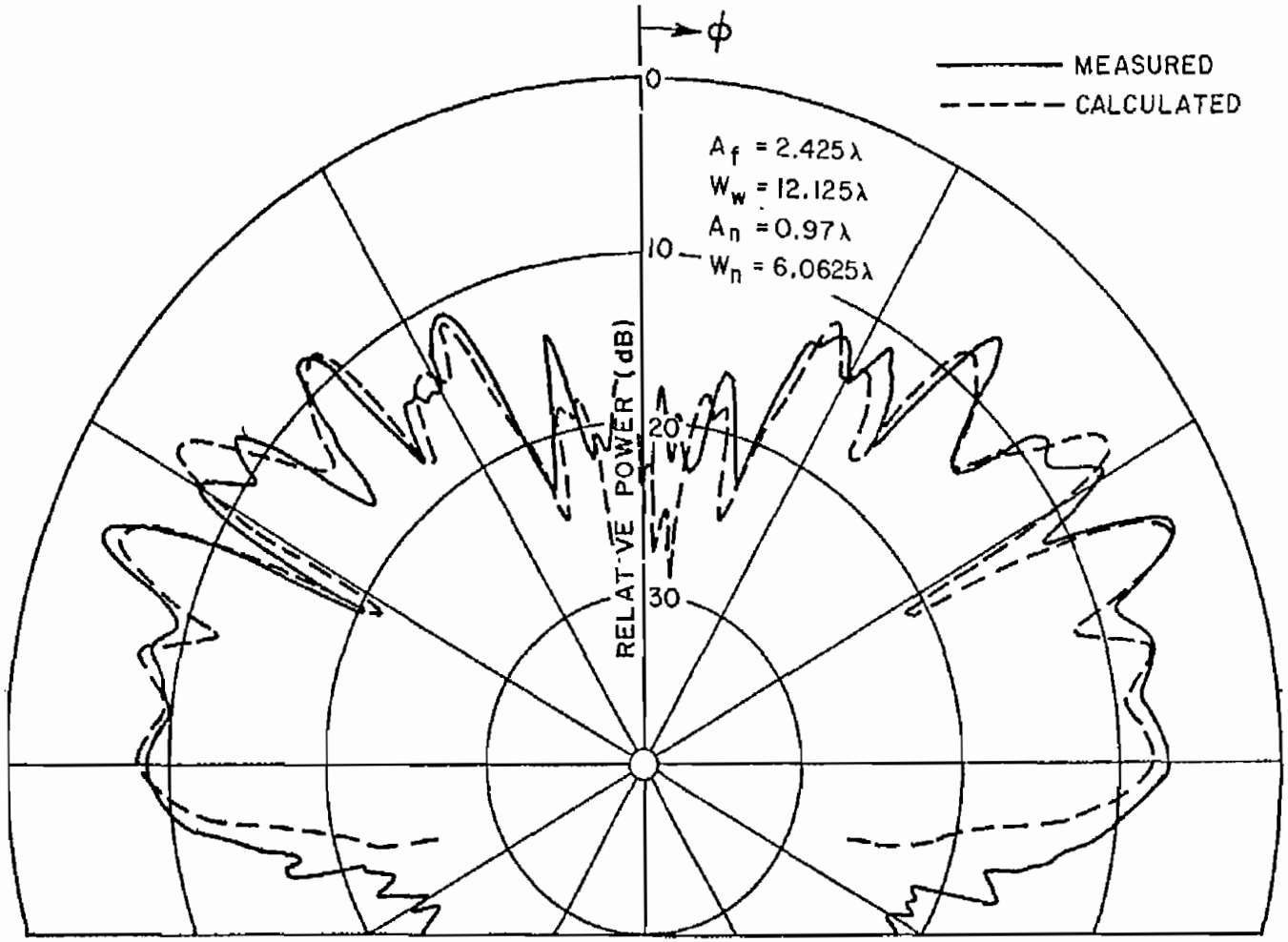

MONOPOLE

Fig. 35. Roll plane pattern.

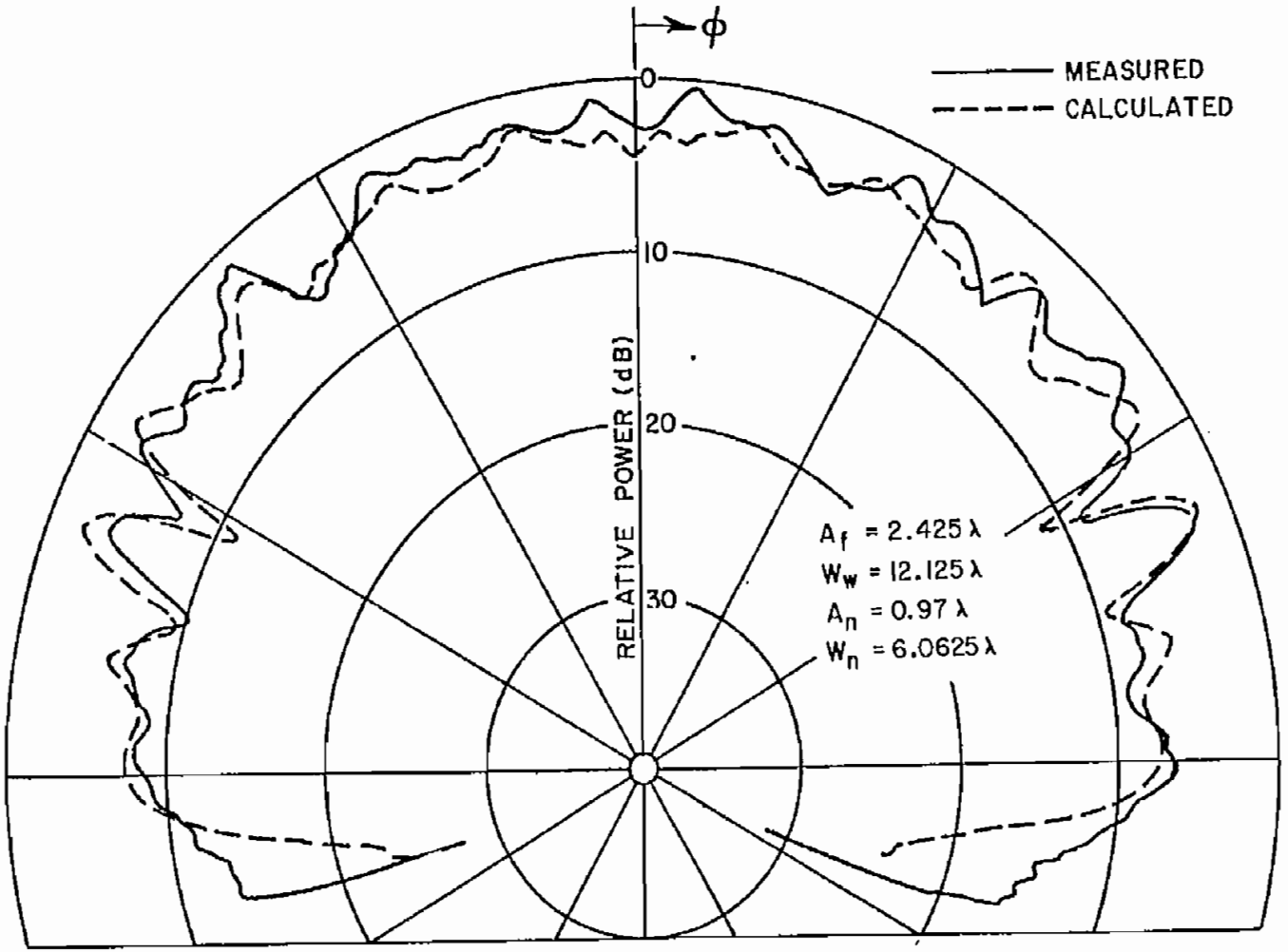

AXIAL SLOT

Fig. 36. Roll plane pattern.

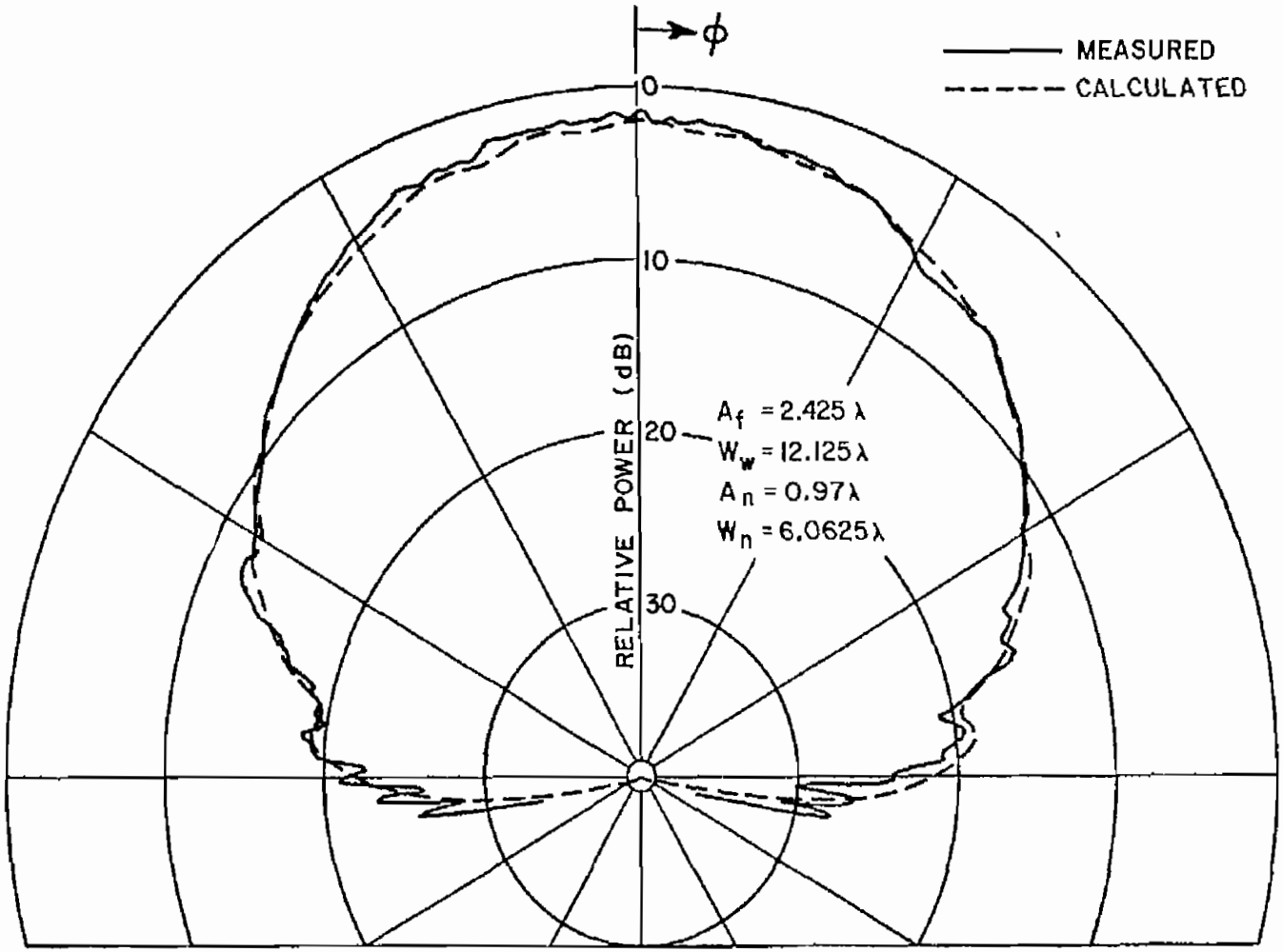

Fig. 37. Roll plane pattern.

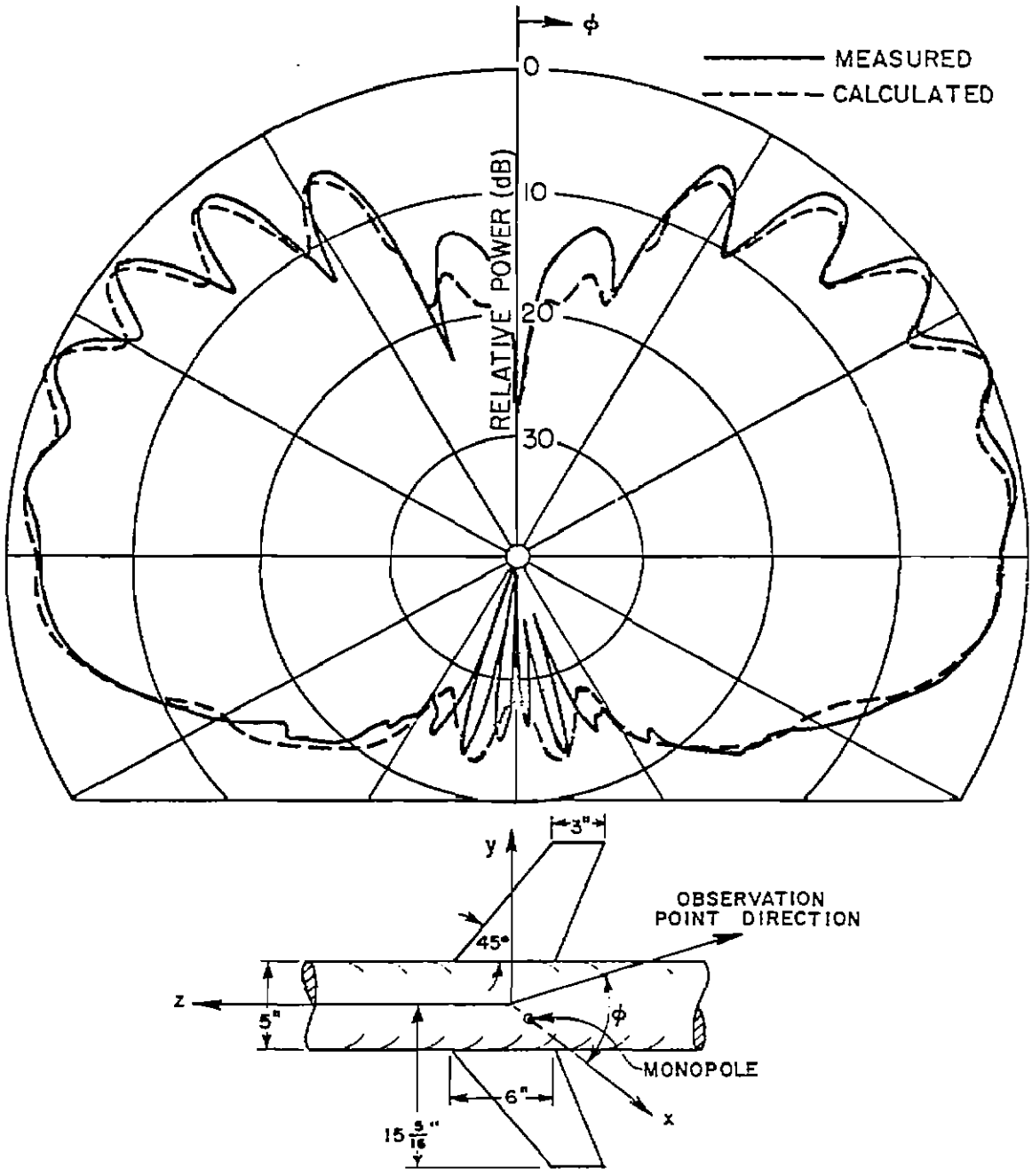

$\lambda = 1.035"$

Fig. 38. E_ϕ radiation pattern for our three dimensional roll plane model.

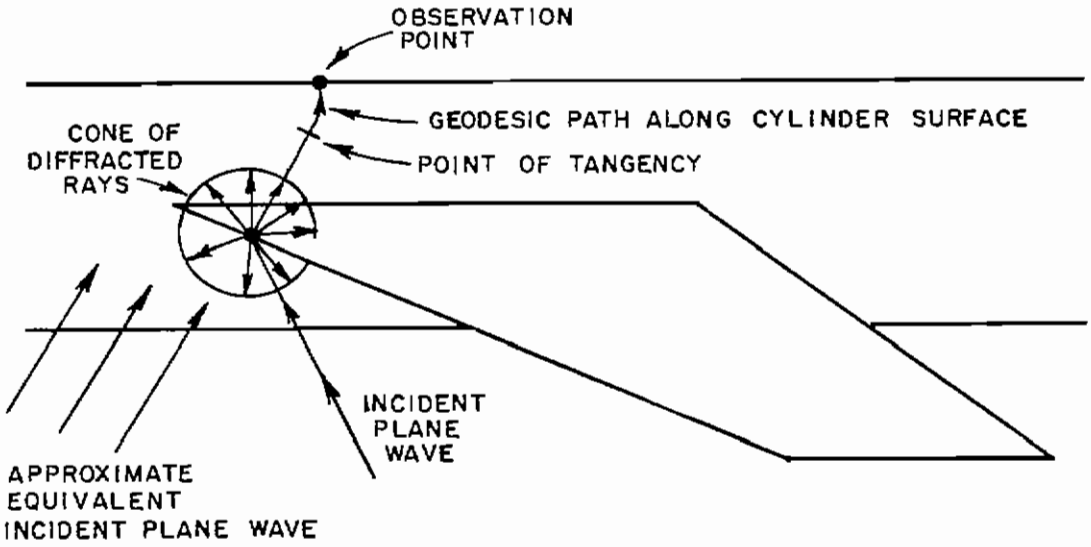

Fig. 39. Ray paths for finite wing.

computation because of the non planar geodesic path for which no theoretical results are presently available. Instead, the modal solution for the scattered fields from an infinite cylinder with an obliquely incident plane wave is used to approximate the effect of the wing edge scattered ray. The direction of incidence of the plane wave is taken as that of the line connecting the apex of the diffraction cone to the tangent point on the cylinder and amplitude and phase reference for the plane wave is taken as that predicted by edge diffraction theory at the point of tangency to the cylinder. The field at the observation point generated by the wing diffracted ray is added to the field at the observation point due to the direct ray which is calculated using the modal solutions of Reference [26]. The measured and calculated fields are plotted in Fig. 38.

Figures 40-47, showing the induced surface current and surface charge density which have been calculated from the surface fields generated by an incident plane wave for the roll plane using some of

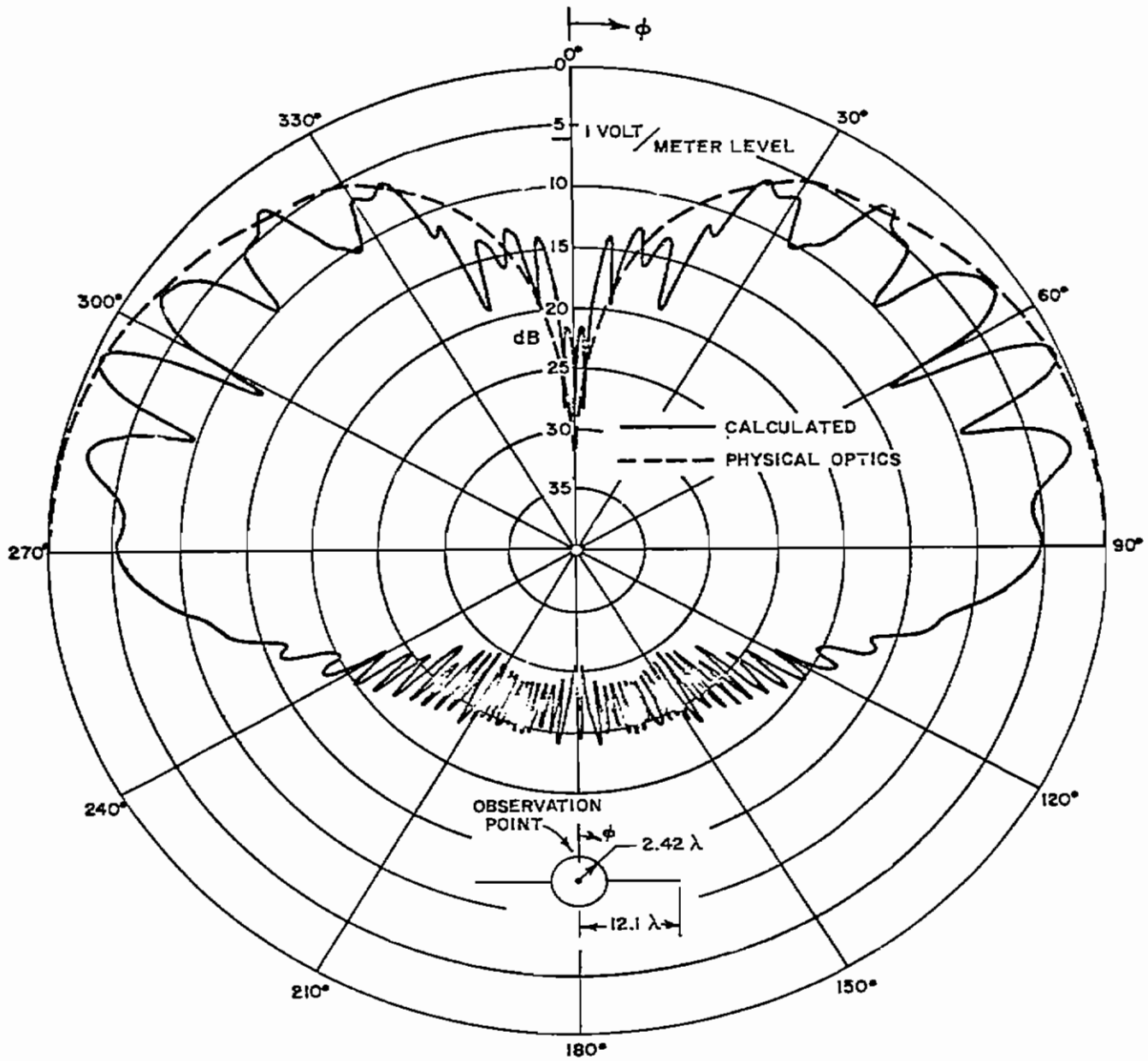

Fig. 40. Normal electric field at observation point due to plane wave incident at angle ϕ.

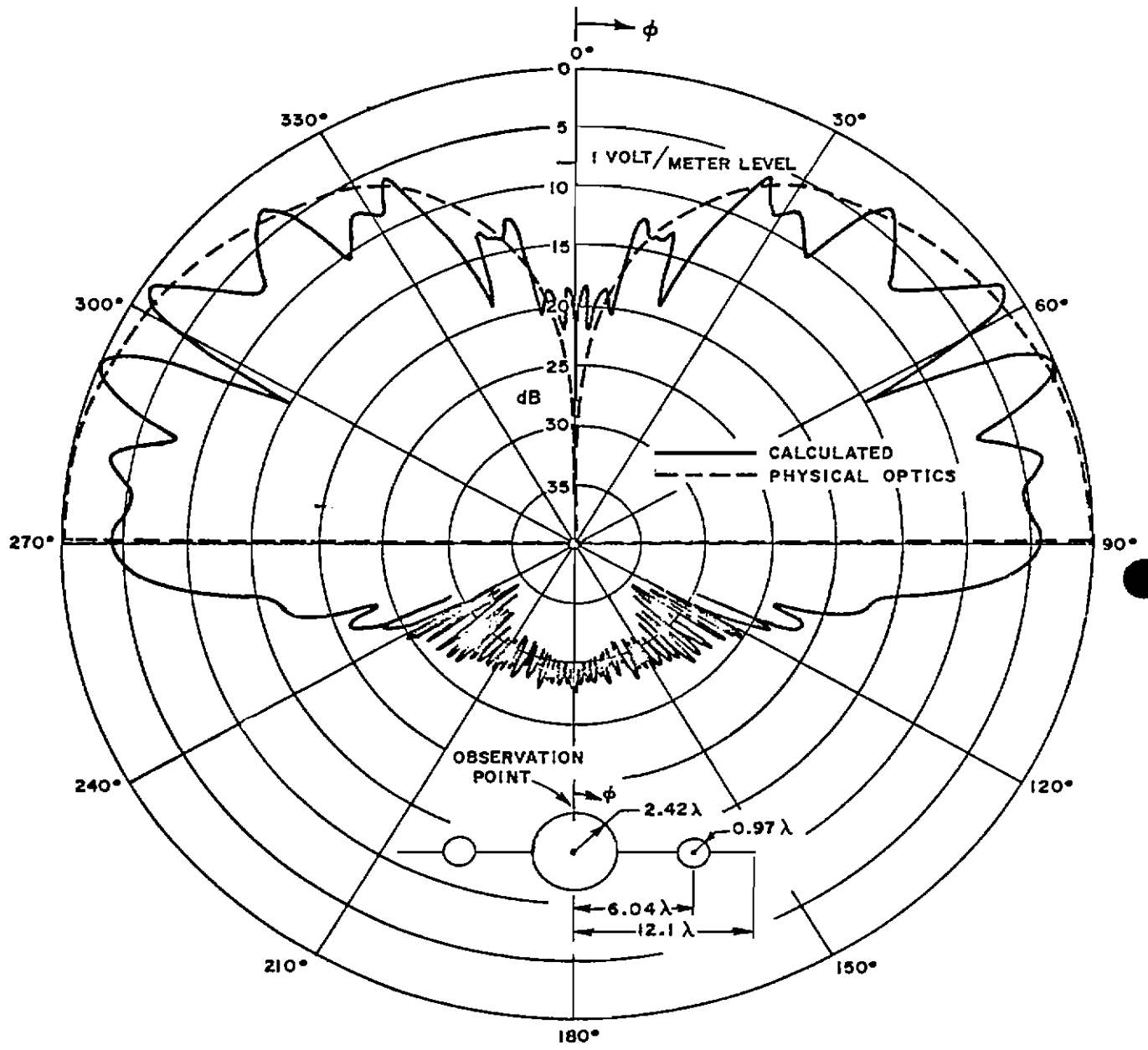

Fig. 41. Normal electric field at observation point due to plane wave incident at angle ϕ.

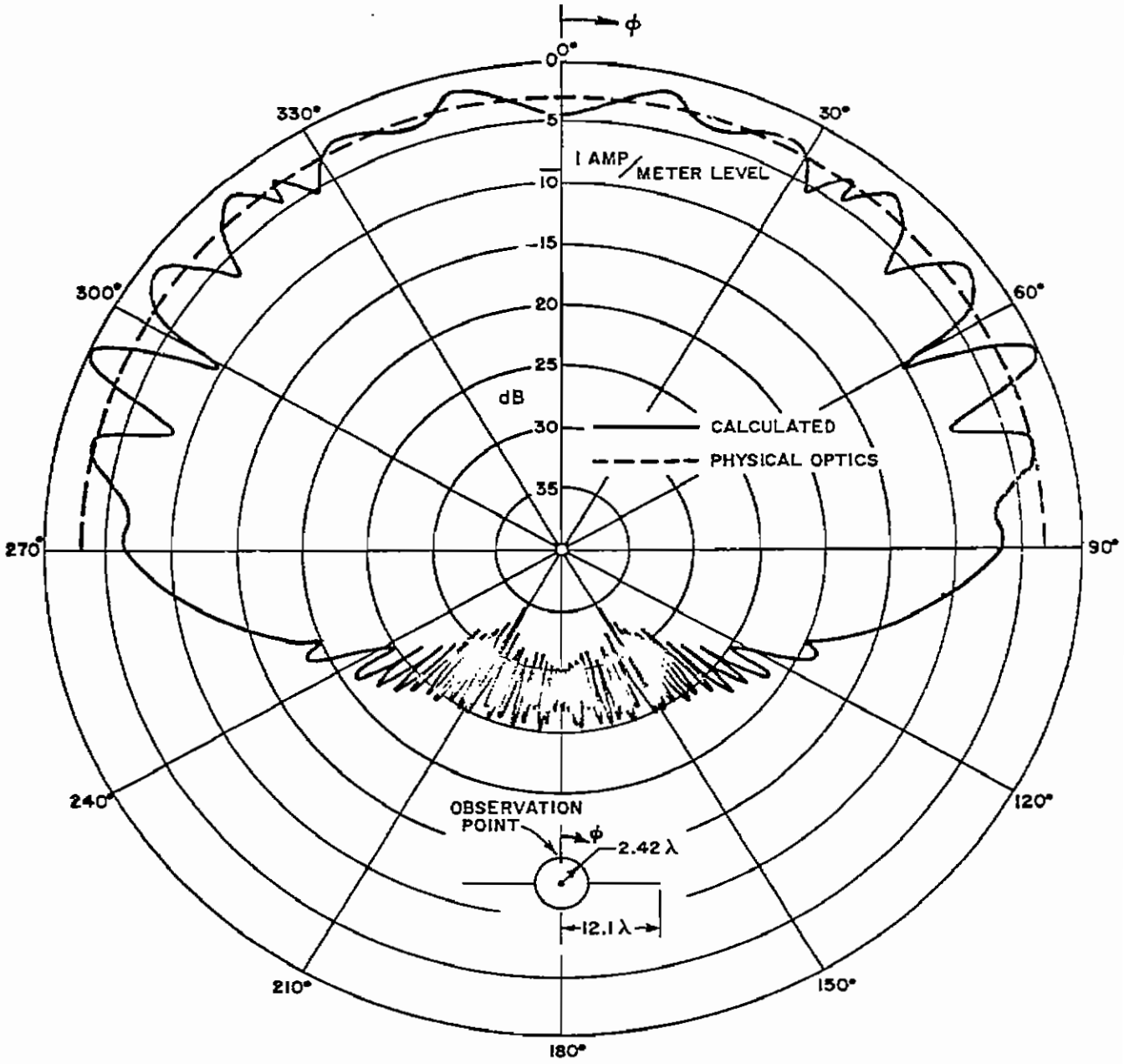

Fig. 42. Circumferential surface current due to plane wave incident at angle ϕ.

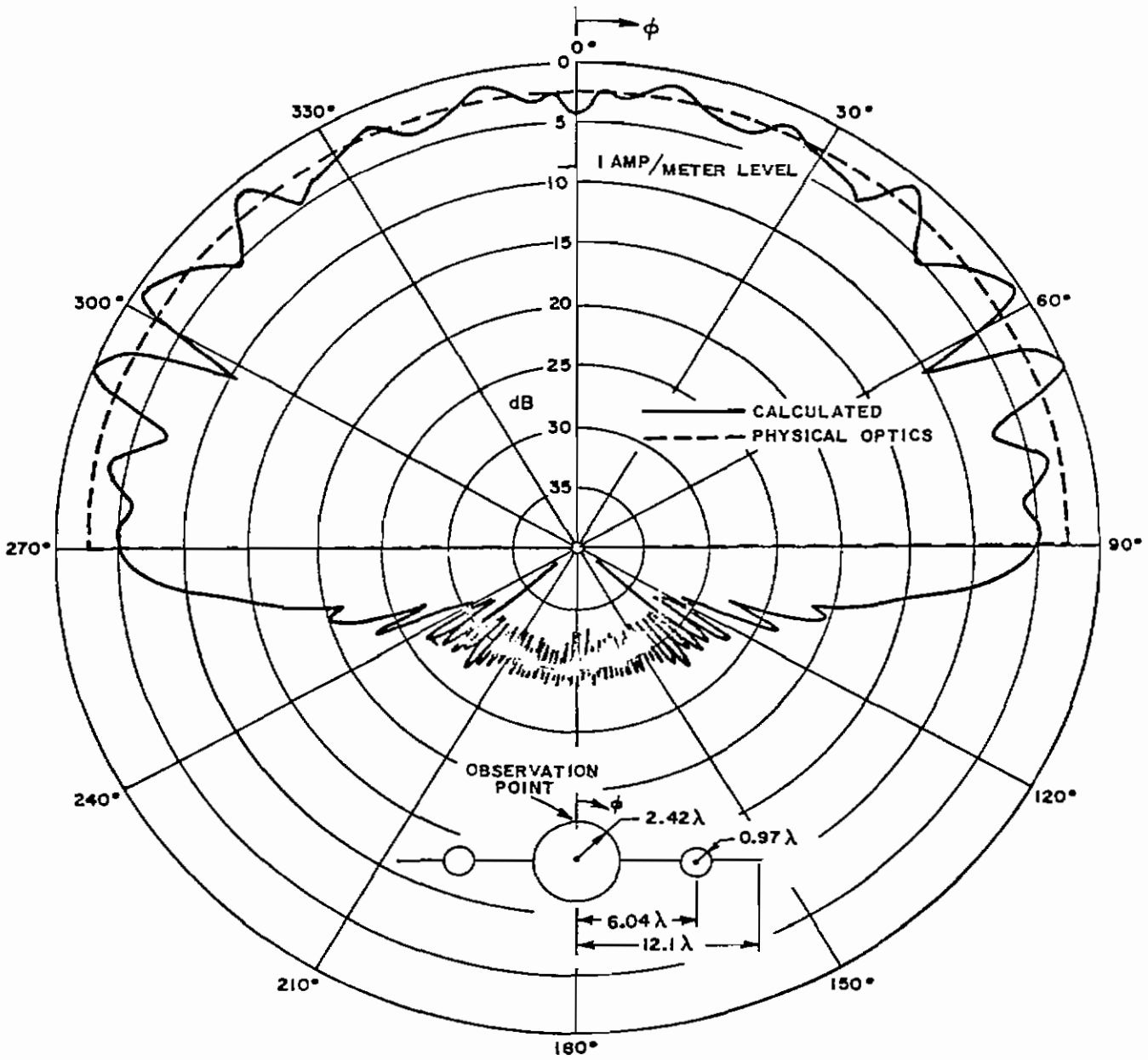

Fig. 43. Axial surface current due to plane wave incident at angle ϕ.

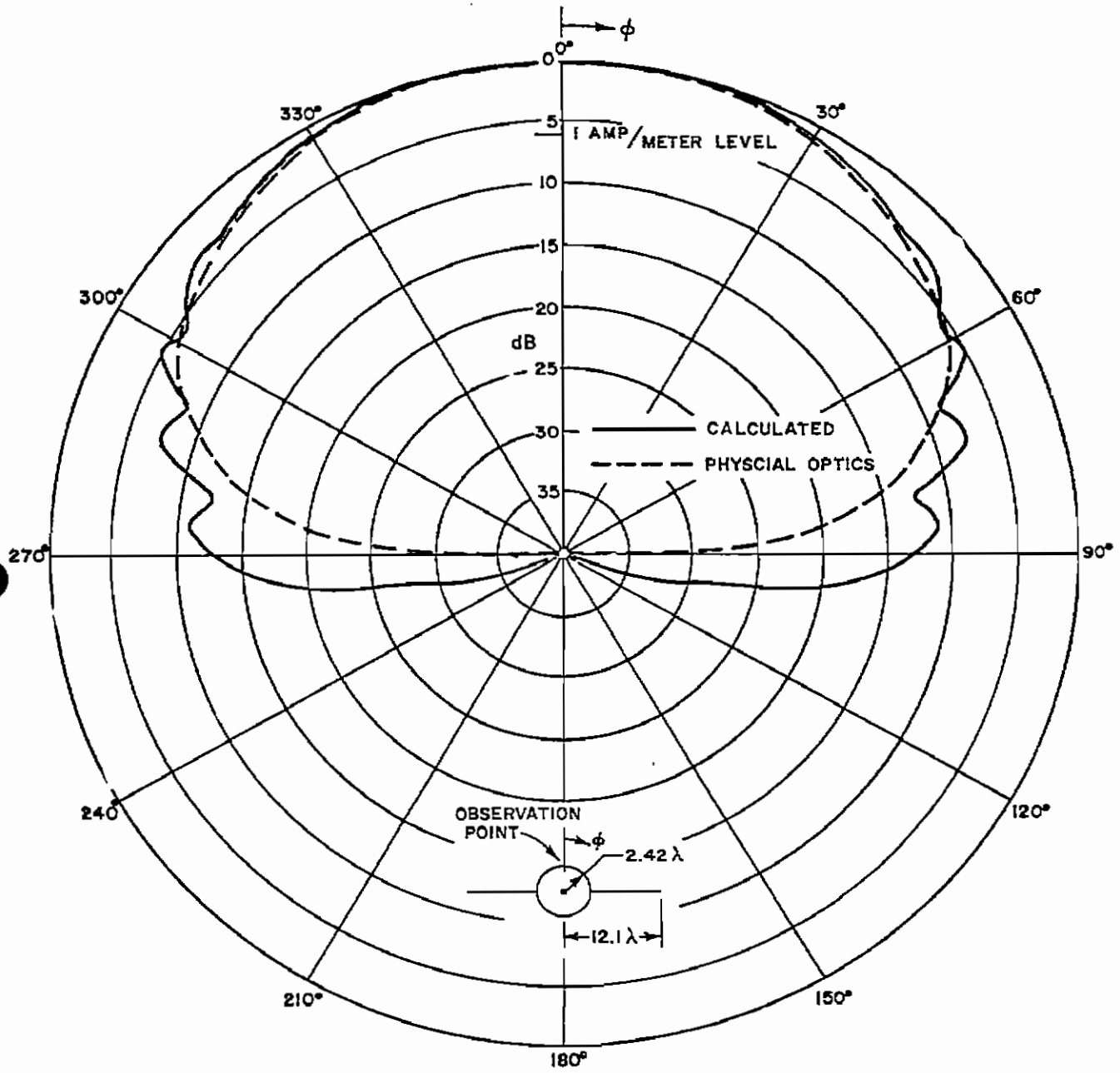

Fig. 44. Axial surface current due to plane wave incident at angle ϕ.

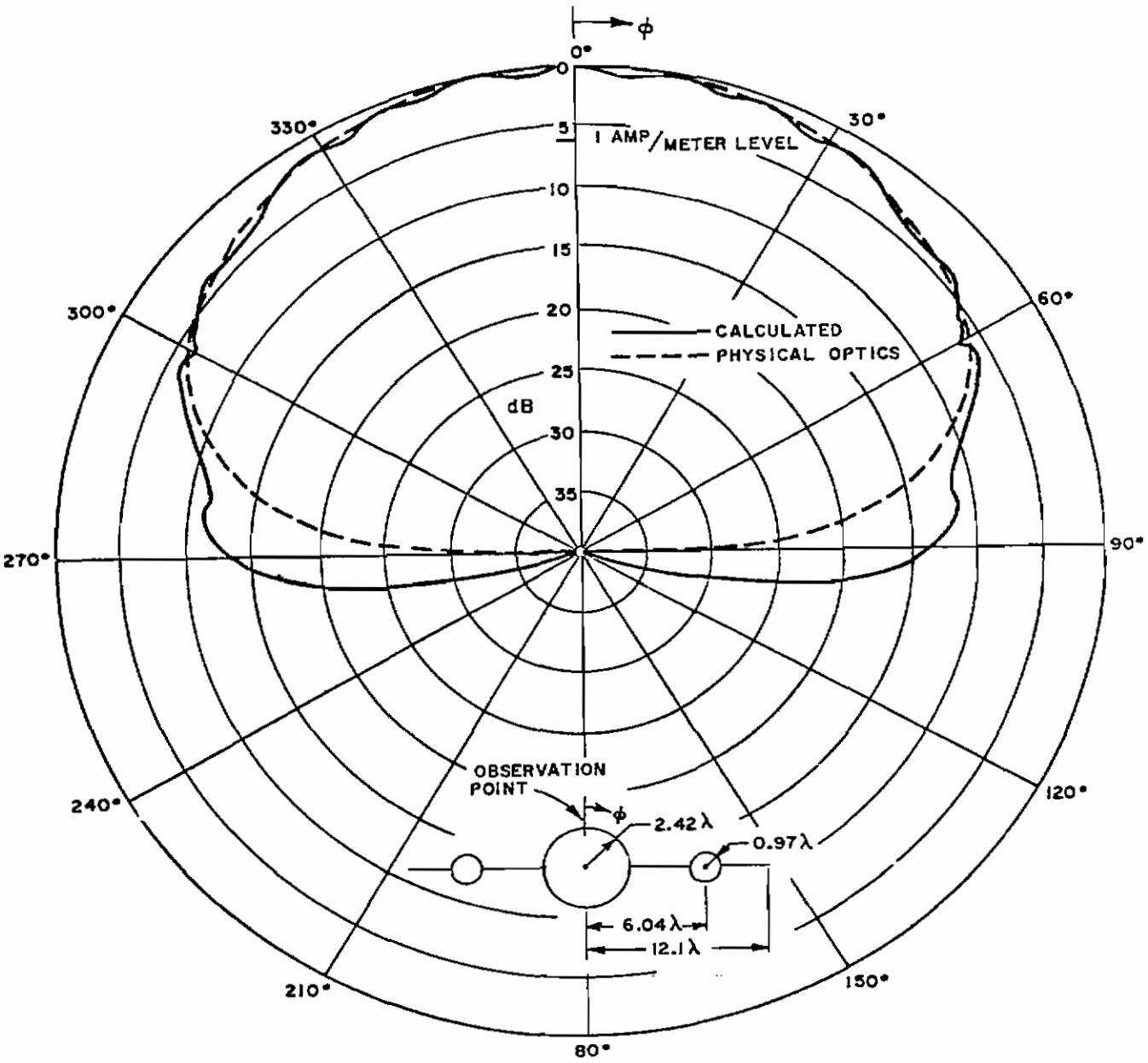

Fig. 45. Circumferential surface current due to plane wave incident at angle ϕ.

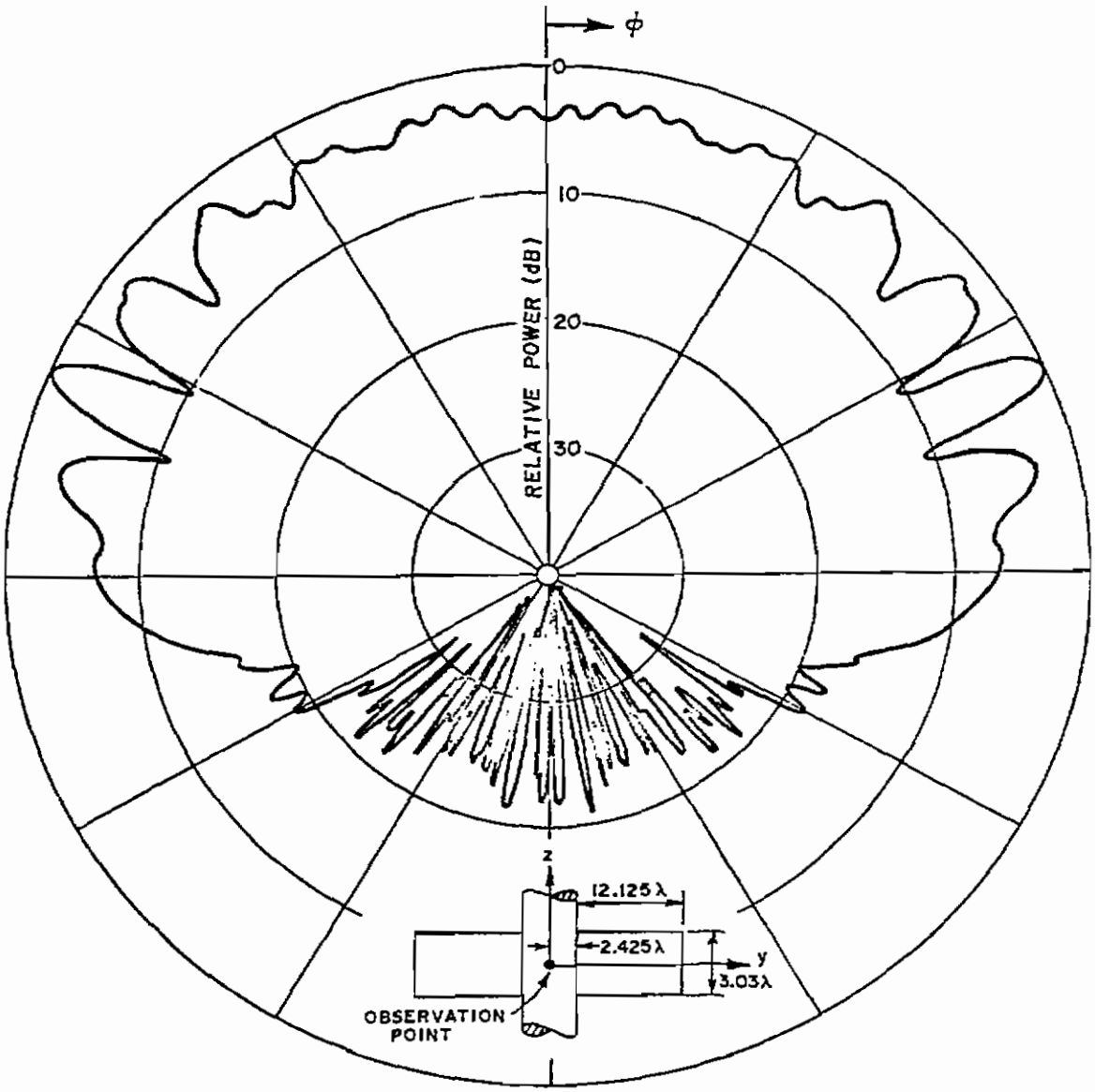

Fig. 46. Calculated circumferential surface current on fuselage with 3 dimensional wing due to plane wave incident at angle ϕ.

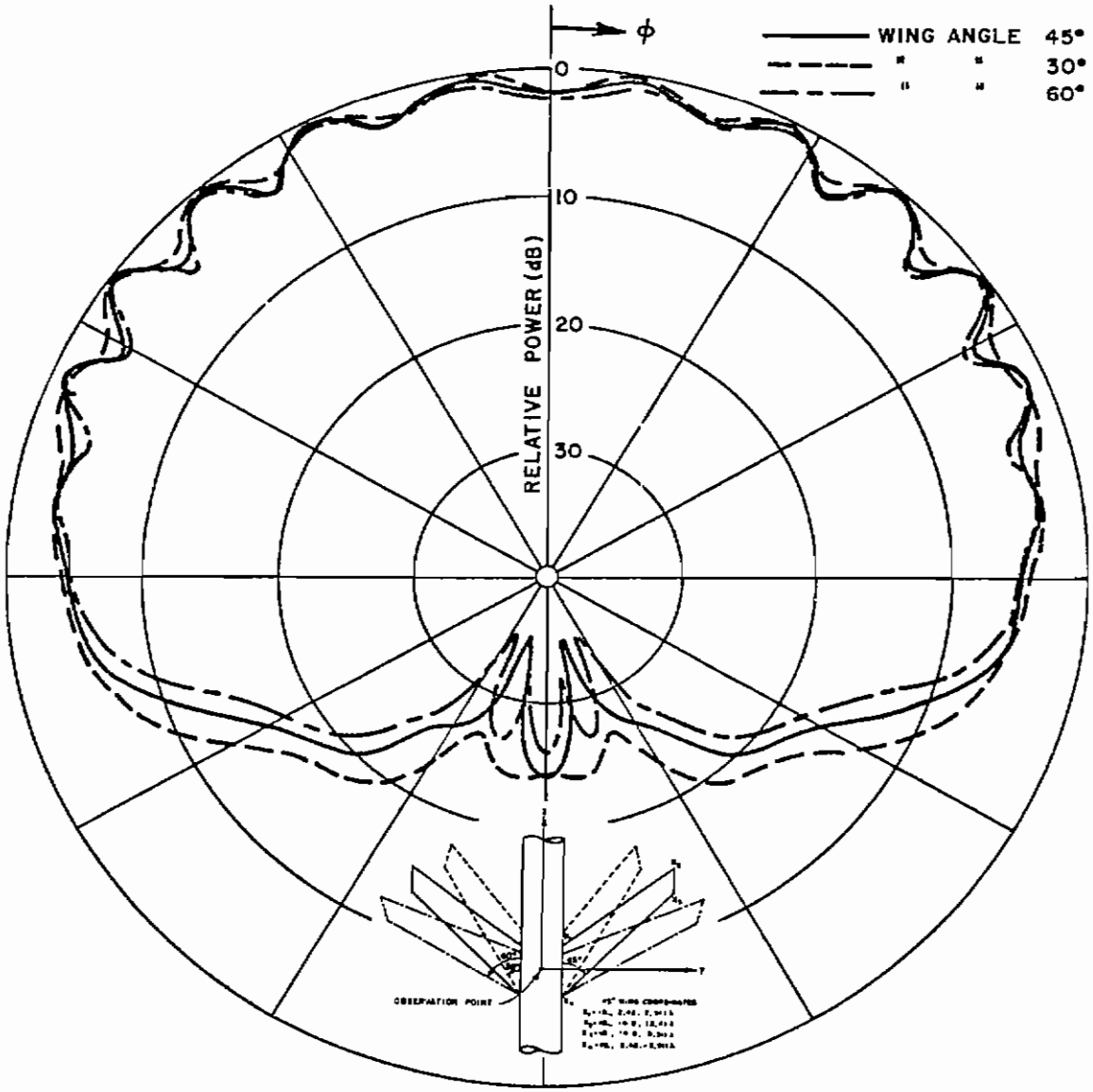

Fig. 47. Circumferential current, roll plane pattern for variable wing angle.

the aircraft-like geometries, were shown previously. The success of these programs, when compared to experiment (using, of course, finite antennas), lend credibility to the programs using infinitesimal antennas since the finite antennas are calculated using a superposition of infinitesimal antennas. The physical optics results for the surface current and surface charge density are also shown in each of the figures. The incident field has been taken to be unity. The analysis used for the azimuth and elevation plane could also be done for infinitesimal antennas. We proceed to illustrate the success of these analyses for finite antennas.

B. Azimuth Plane Analysis

The fuselage portion of the aircraft structure has the dominant effect upon the radiation pattern in this plane. Using the modal solutions similar to those of Reference [26] the fields at the surface of an infinite circular cylinder have been calculated. The engines have a secondary effect on the pattern which can be calculated by modeling the engines as finite circular cylinders with closed ends. The near zone scattering from finite cylinders was analyzed using physical optics, modal solutions, and wedge diffraction. The physical optics solution was used when the observation point was near the specular region of end cap. Whereas, wedge diffraction was used outside that specular region to account for the diffractions from the edges of the finite cylinder. Finally, the modal solution was used to determine the field in the specular region of the long cylinder portion.

Some calculated and measured patterns for the model with and without engines are shown in Figs. 48-50. In the azimuth plane the distant source is always "visible" at the observation point and is not blocked from view by the aircraft structure as in the roll plane pattern where, for instance, the fuselage may block the direct

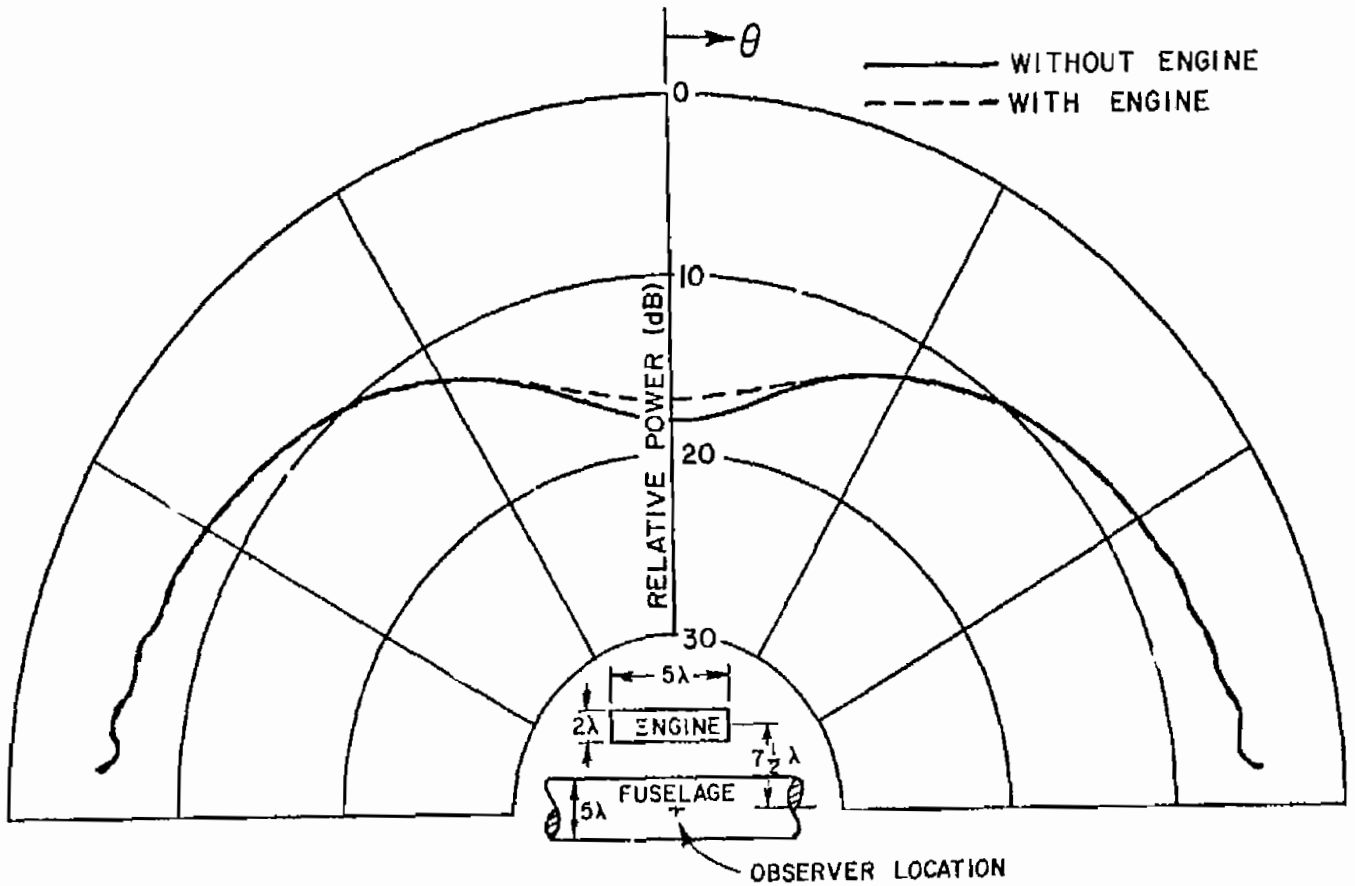

Fig. 48. Calculated azimuth plane pattern.

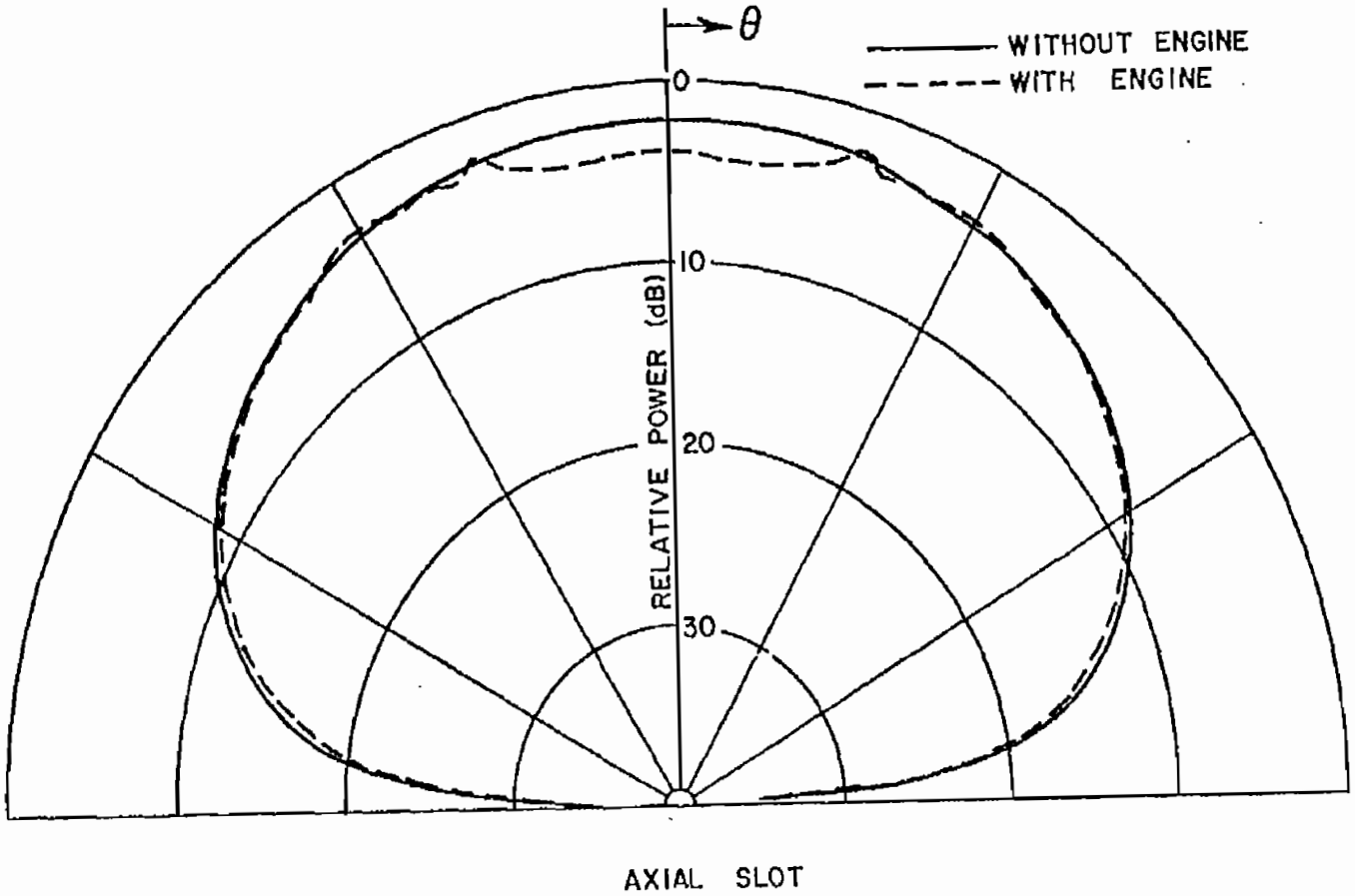

Fig. 49. Calculated azimuth plane pattern.

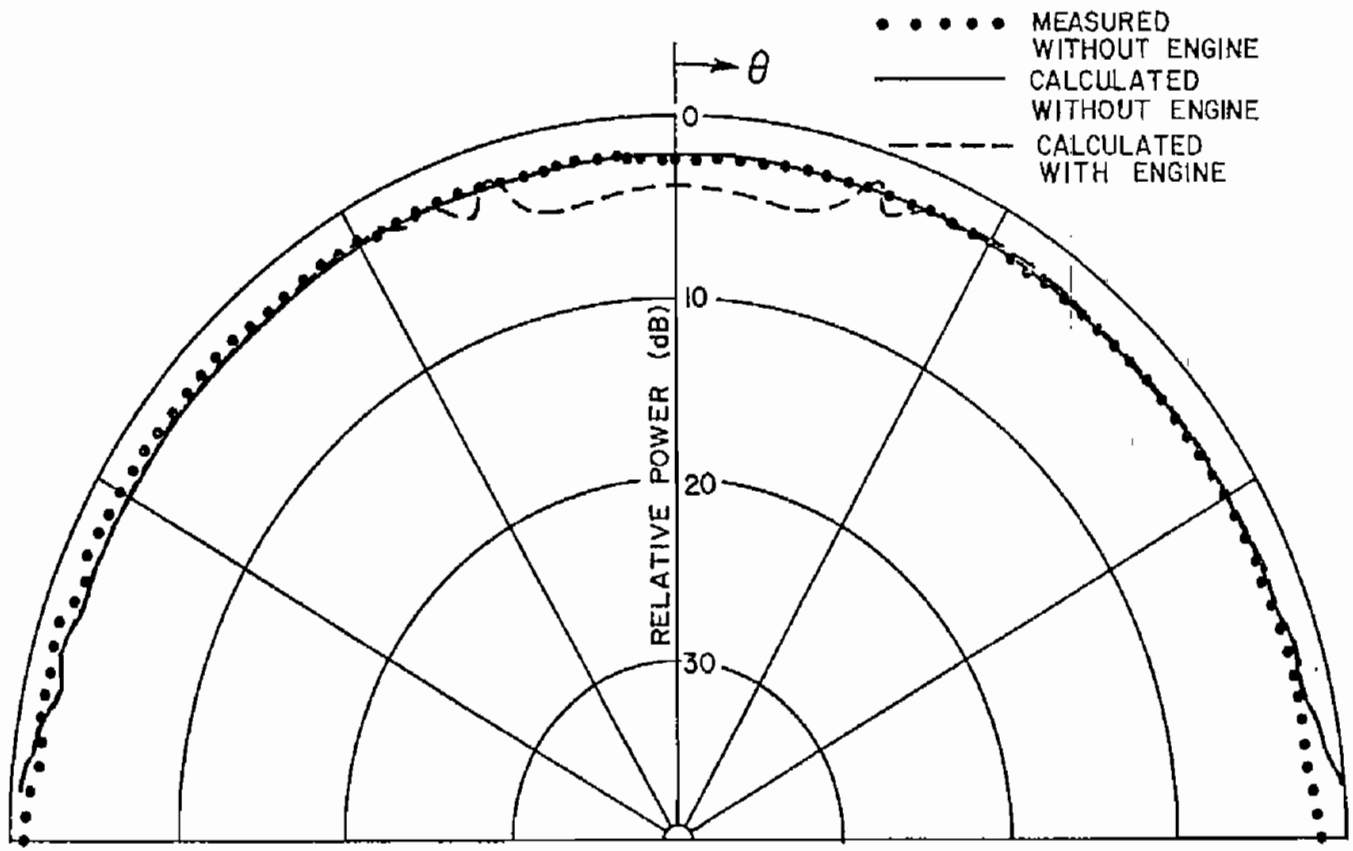

Fig. 50. Calculated azimuth plane pattern.

ray from the distant source to the observer; hence, the pattern for the normal component of the electric field is fairly uniform in this plane.

C. Elevation Plane Analysis

The solution for the elevation plane patterns were based on a two dimensional analysis which, as shown by Ryan[27], is valid for the three dimensional elevation plane patterns. Fig. 51 illustrates

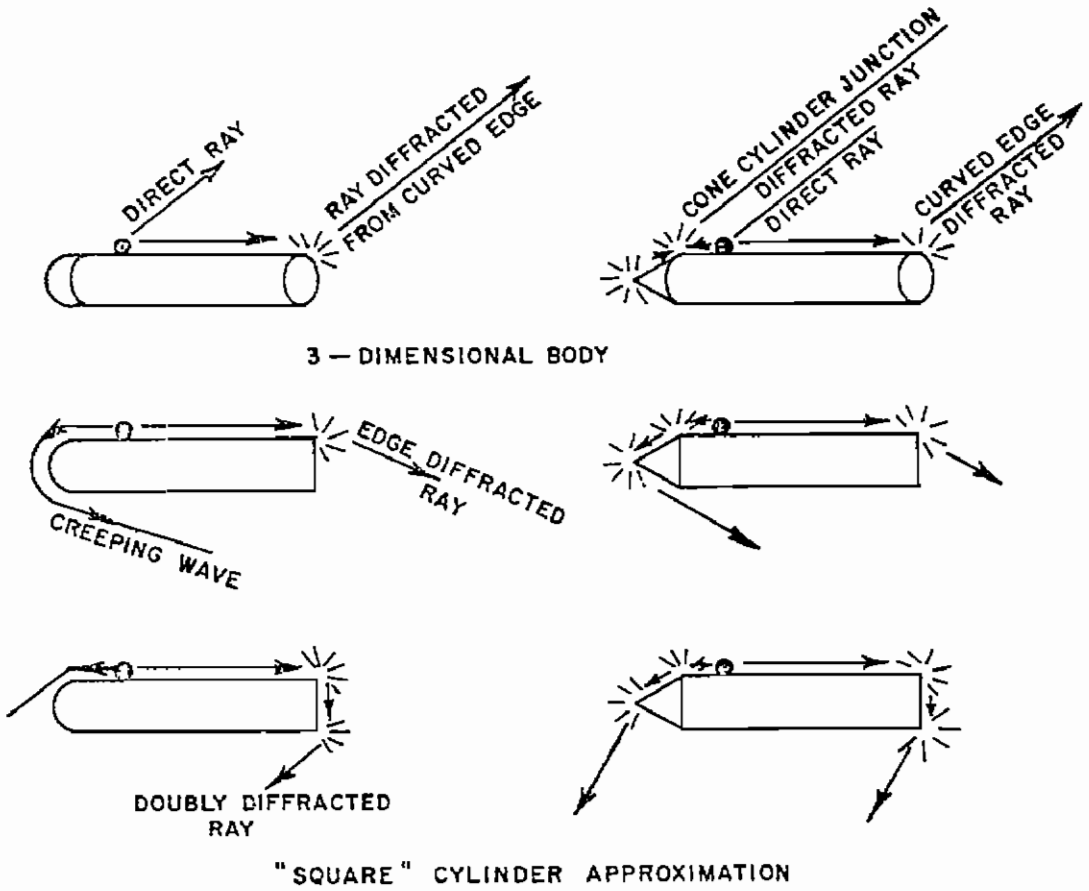

Fig. 51. Diffraction mechanisms for the elevation plane.

the dominant scattering mechanisms used in the calculation of surface fields on a hemispherically capped finite cylinder and a conically capped finite cylinder. The effect of the cone tip, as was found by Ryan[27], can be accurately modeled in this principle plane by a two dimensional wedge. Tip diffraction is unimportant except when the source is not visible to the observer.

Burnside's analysis of the transmitted fields in this plane is divided into two cases depending upon whether or not the observer has a direct ray path to the source. For aspects that permit such a direct ray path, the direct ray contribution to the observed field is computed using an infinite perfectly conducting plane as a model for the cylinder while the diffracted field contributions are computed on the basis of a three dimensional body as shown in the upper two sketches of Fig. 51. The diffraction from the curved edges are computed using the diffraction coefficient of a curved edge but the cone tip must be included using the two dimensional wedge approximation. For aspects where there is no direct ray from the source to the observer the "square" cylinder approximation is used instead of the more accurate equivalent edge currents since the edge current formulation requires lengthy computations without an equivalent improvement (see previous section, Figs. 21 and 22). The results are shown in Figs. 52-54.

More general two dimensional outlines have been examined using a point description of the elevation plane cross-section of a convex fuselage. In this analysis only the direct ray and creeping wave contributions to the radiated field are computed. The creeping wave propagation and diffraction coefficients are computed using the local radius of curvature of the body. This is termed section matching.

A fuselage cross-section consisting of two back to back ellipses has been studied using the geometrical theory of diffraction. The

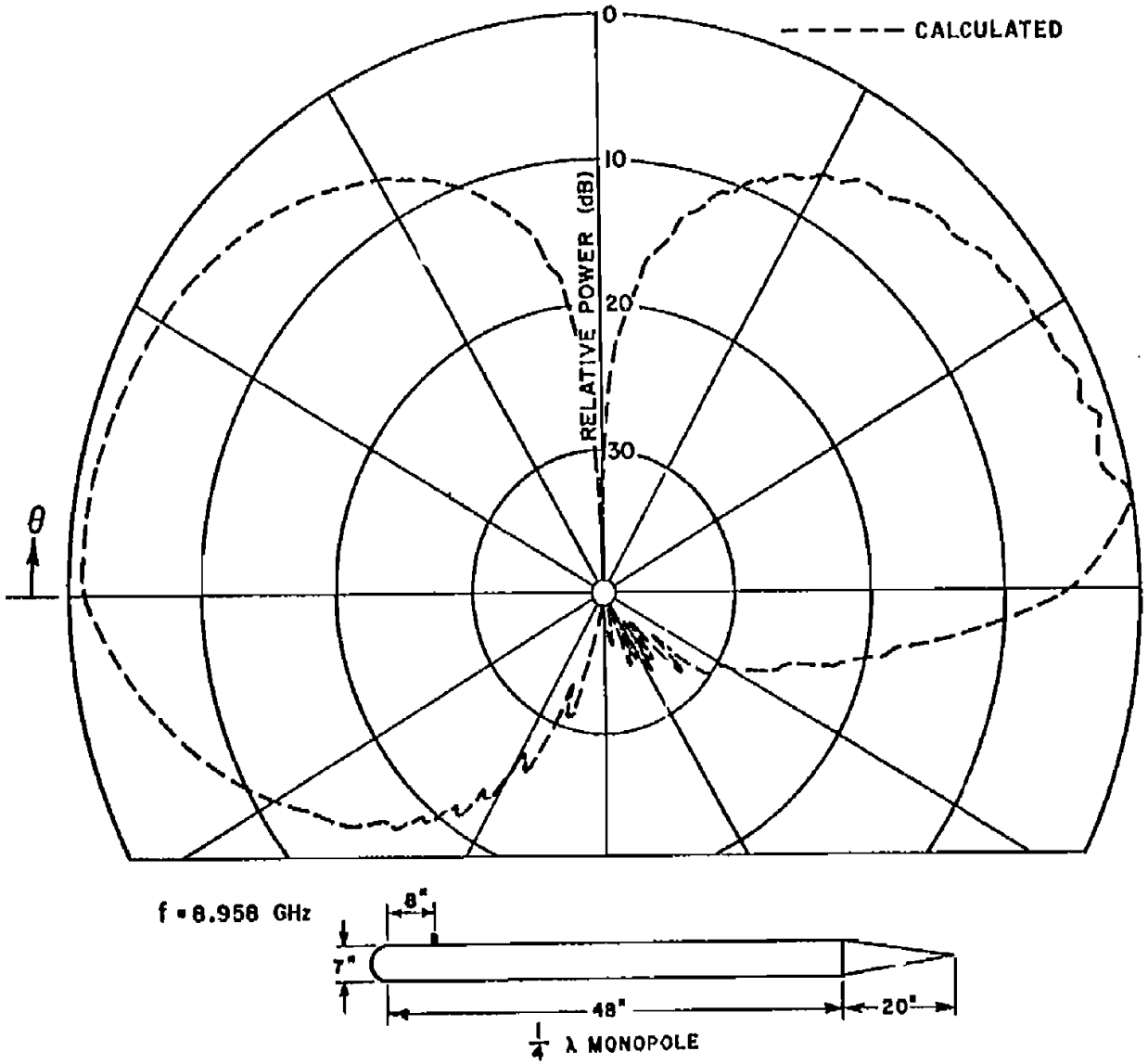

Fig. 52. Elevation plane pattern.

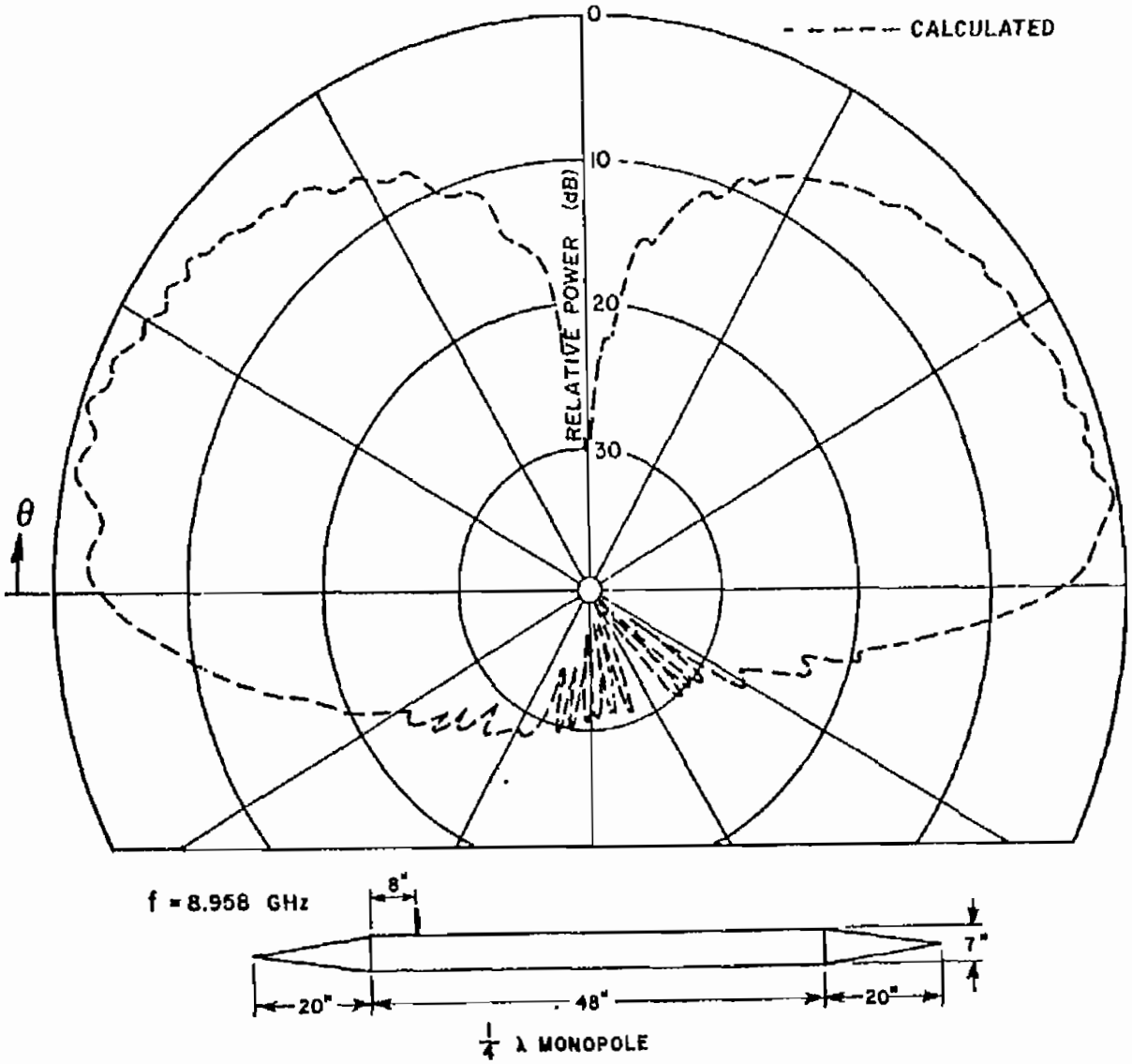

Fig. 53. Elevation plane pattern.

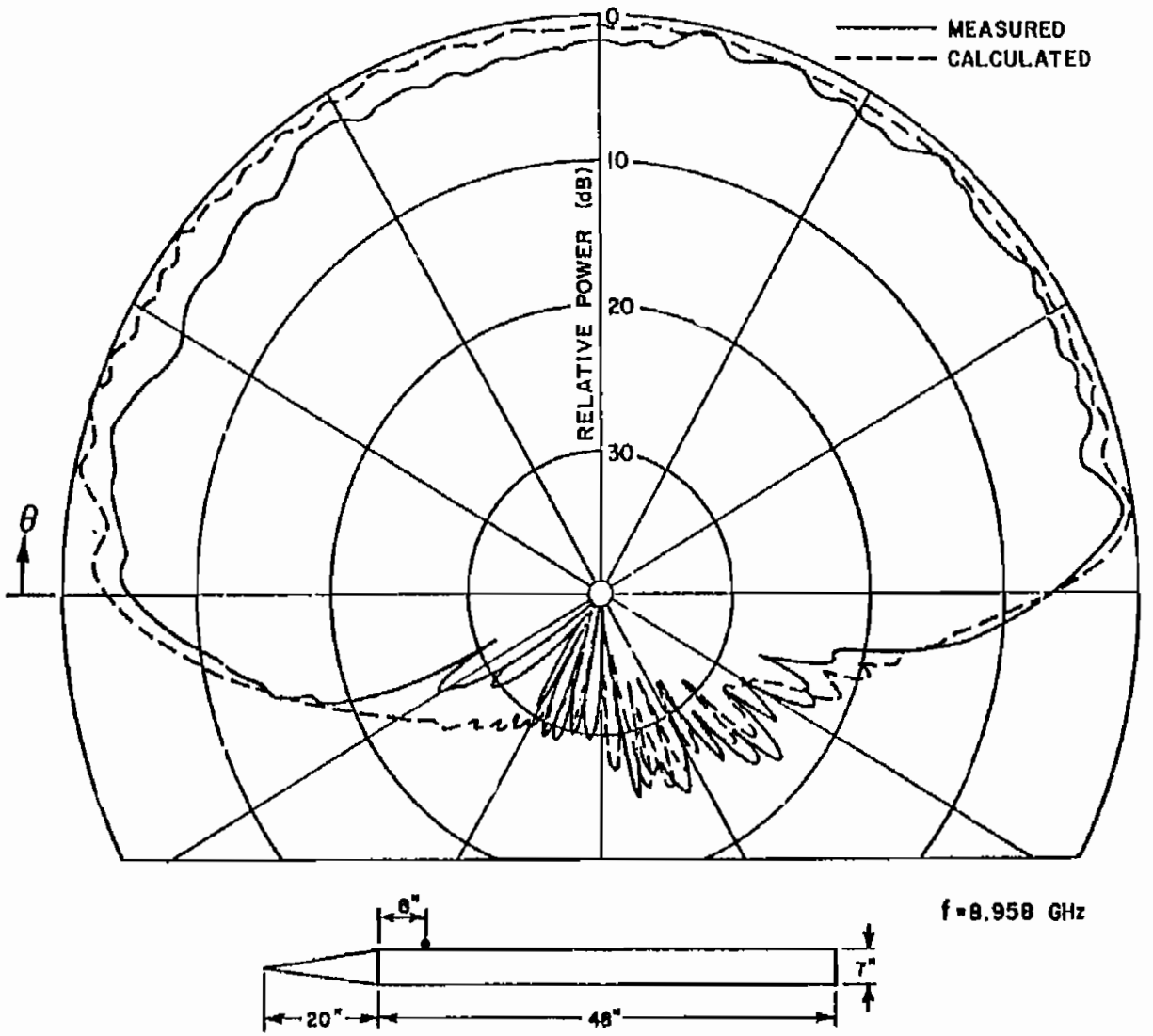

CIRCUMFERENTIAL SLOT

Fig. 54. Elevation plane pattern.

computed patterns using the geometrical theory of diffraction with and without the section matching technique (wherein the outline is described by a set of points) are compared in Figs. 55-57 for varying locations of the observation point.

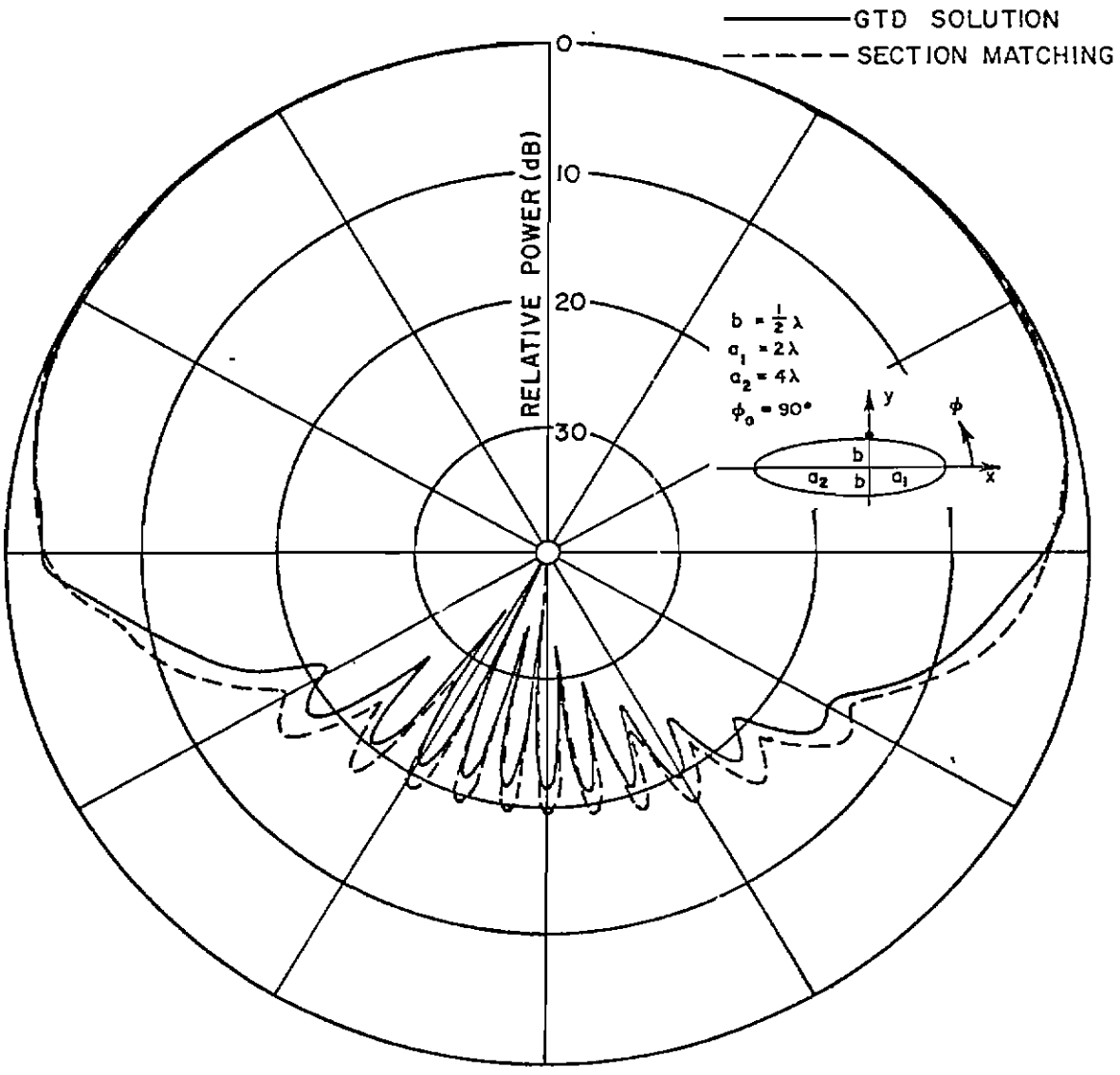

(a)

Fig. 55. Elevation plane pattern of a circumferential slot mounted on a composite-ellipse model.

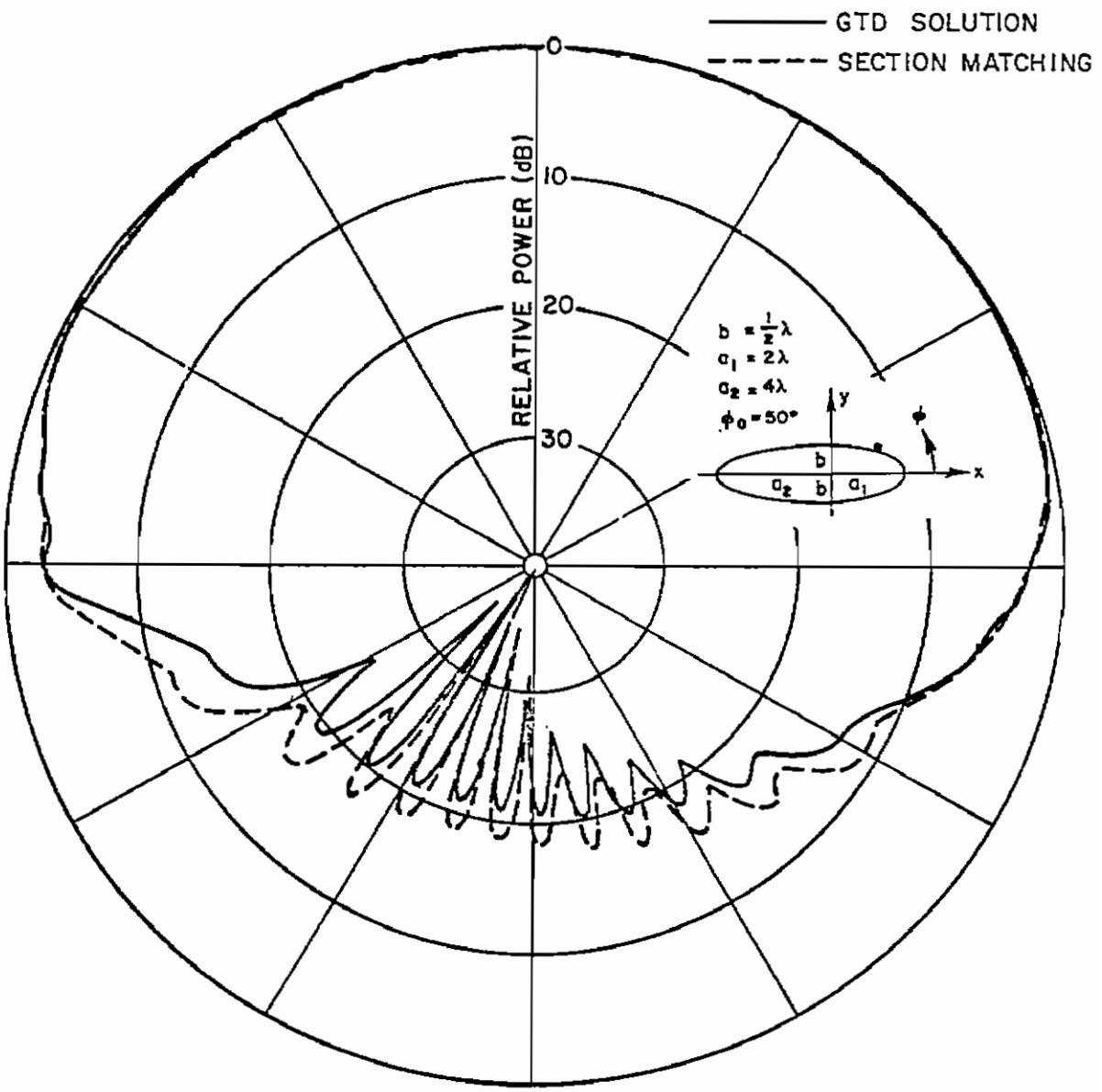

(b)

Fig. 56. Elevation plane pattern of a circumferential slot mounted on a composite ellipse model.

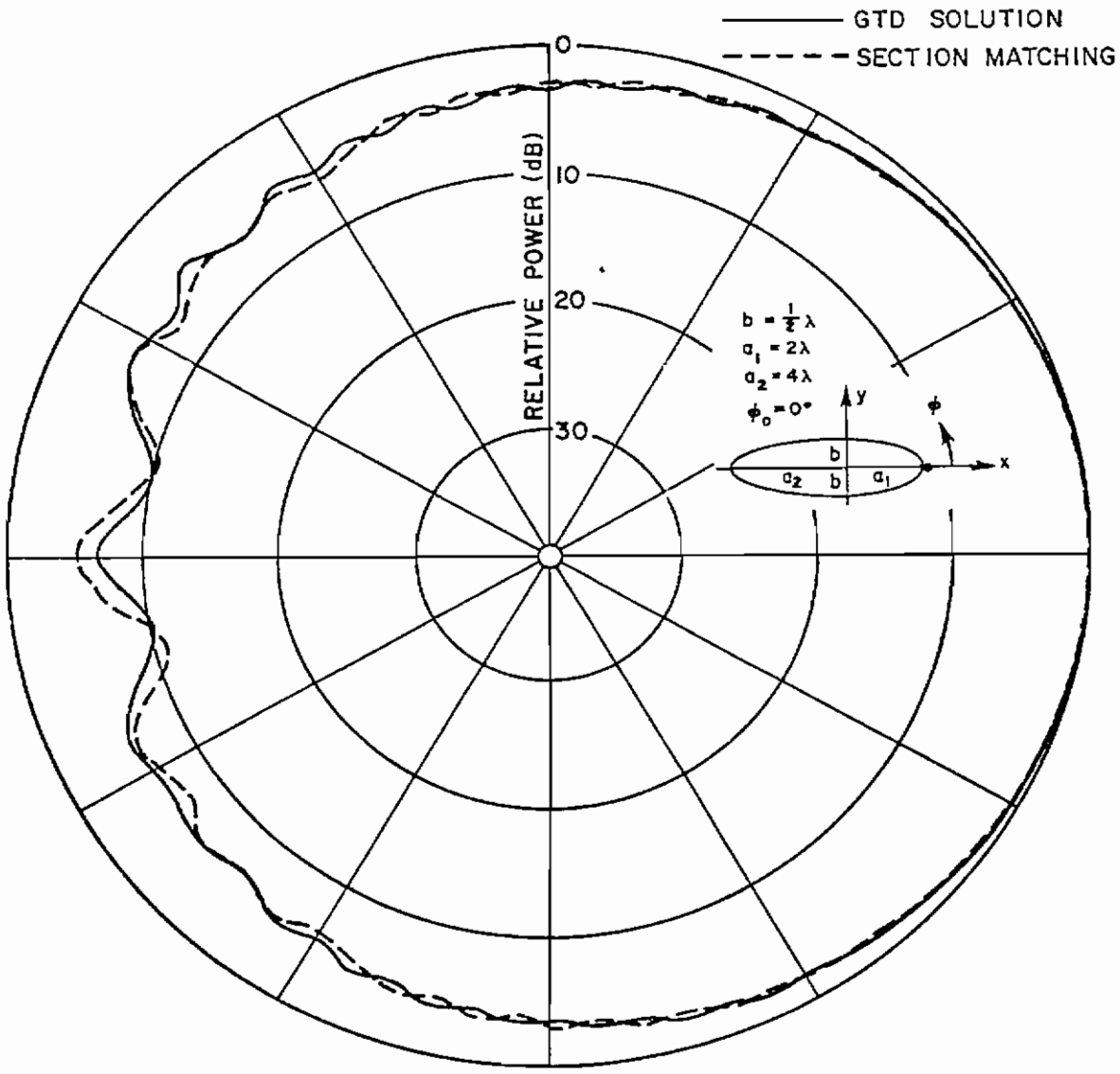

(c)

Fig. 57. Elevation plane pattern of a circumferential slot mounted on a composite ellipse.

D. Comparison of GTD and Physical Optics Results

In the preceding sections, the physical optics surface charge and current densities

$$\bar{J} = 2\hat{n} \times H^i \tag{42}$$

and

$$\rho = 2\varepsilon_o \hat{n} \cdot E^i \tag{43}$$

have been suggested for calibration of conventional thin slot and short monopole antenna patterns to obtain $\bar{J}$, ρ at the pattern maximum. Use of reciprocity would then give the $\bar{J}$, ρ for any angle of incidence. The purpose of this section is to demonstrate that these simple formulas can be used to reasonably approximate $\bar{J}$, ρ when the observation point is in the "lit" region and the scattering body is large enough in terms of wavelengths. Consequently some typical results obtained in the preceding sections are compared with those computed from Eqs. (42) and (43).

In Figs. 58-65 the physical optics result is plotted along with computed and measured data for several different bodies. The physical optics results do not predict any currents in the shadowed regions of a body. One criterion then for the applicability of physical optics is a very low level of surface current in the non-illuminated region of a body. The sphere gives another useful criterion for the applicability of physical optics. The physical optics approach fails for backscattering for spheres of radius one wavelength or less. One can go further and say, as a rule of thumb, that when a body has scattering centers with radii of curvature less than one wavelength then physical optics will fail to predict the scattering and the surface currents. This can be seen in Fig. 66

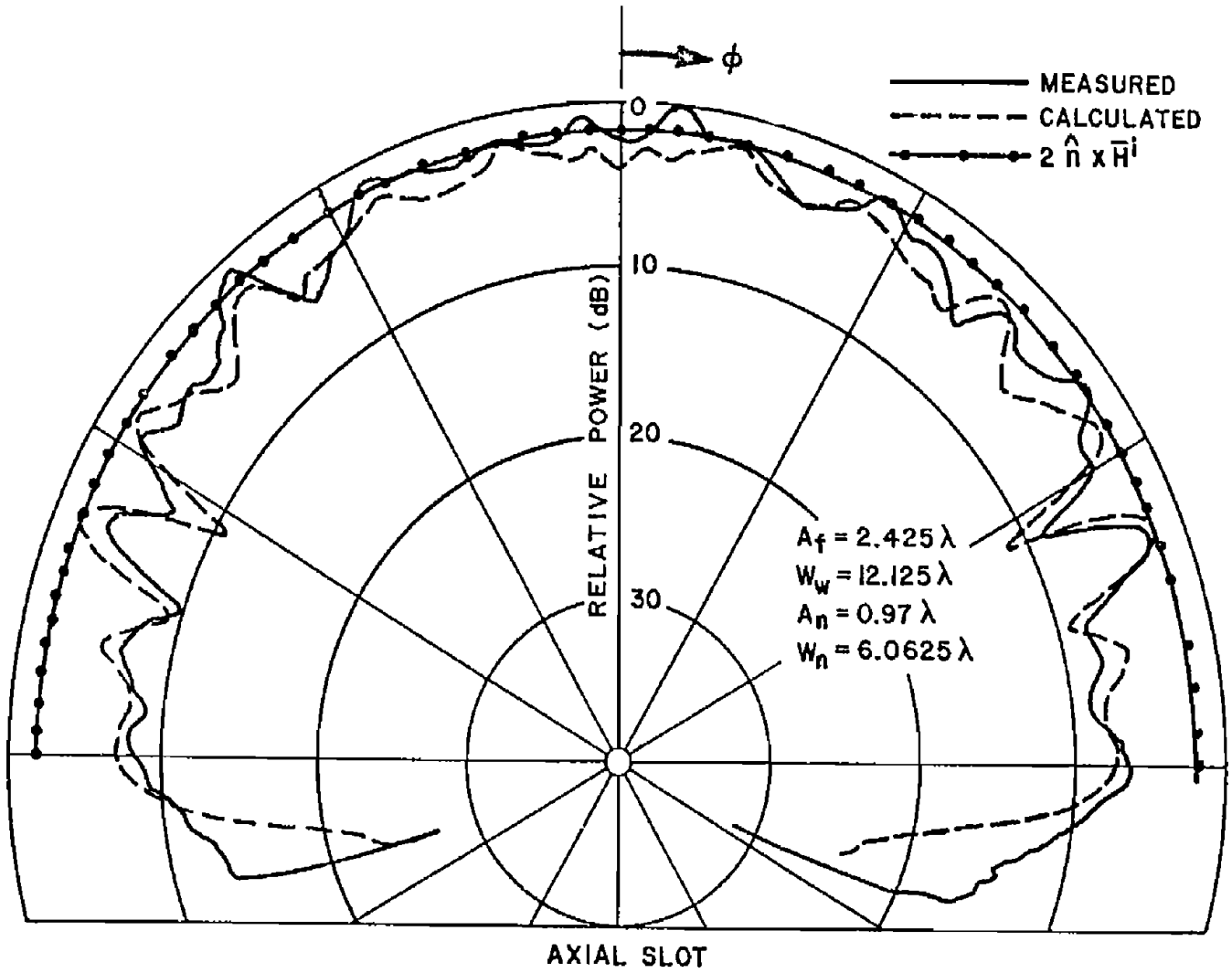

Fig. 58. Roll plane pattern.

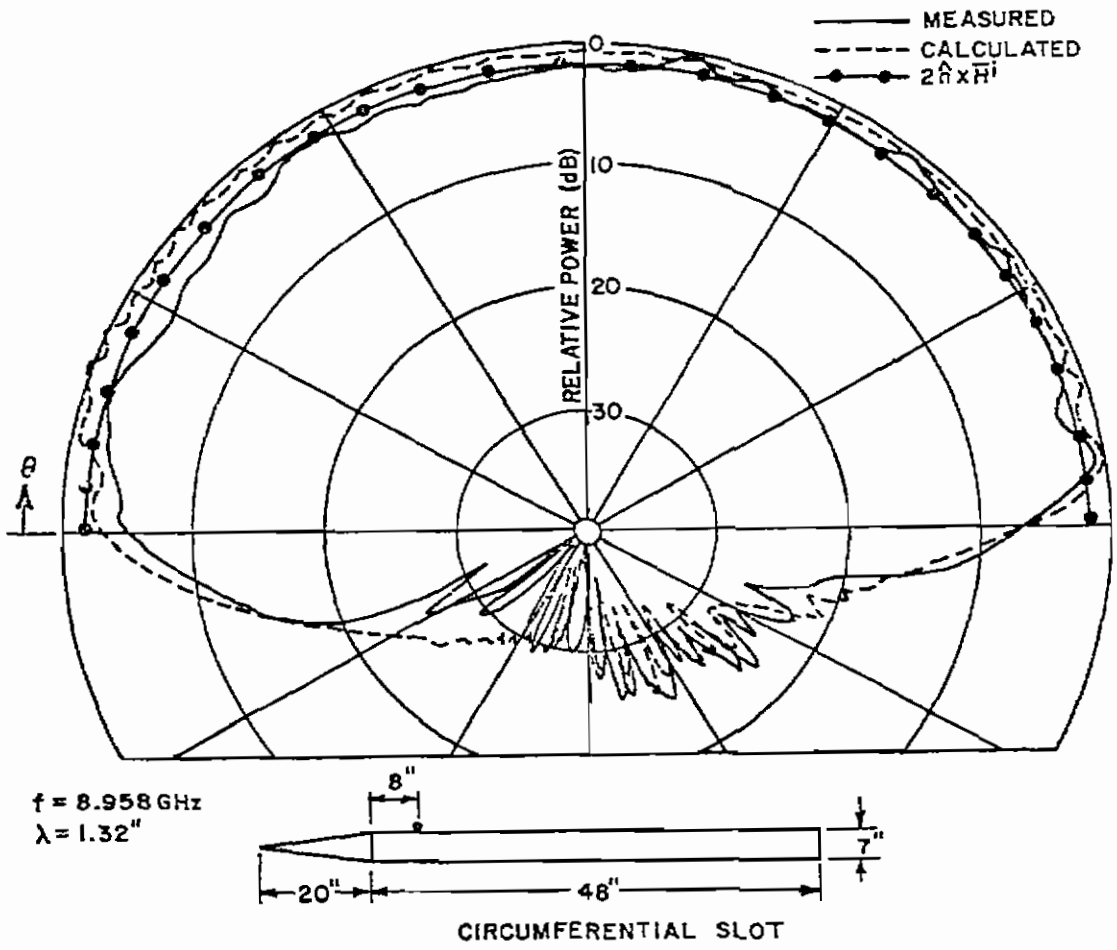

Fig. 59. Elevation plane pattern.

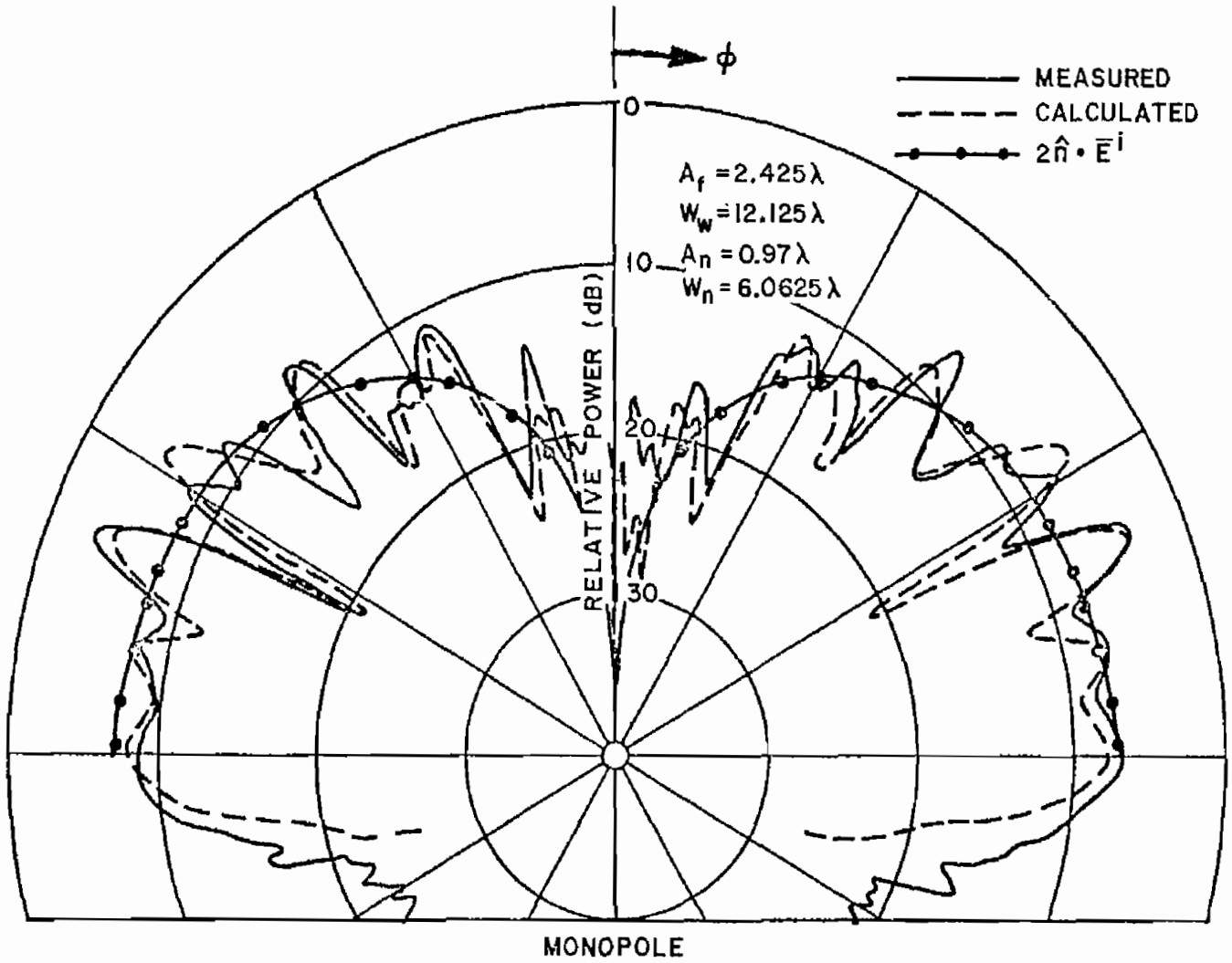

Fig. 60. Roll plane pattern.

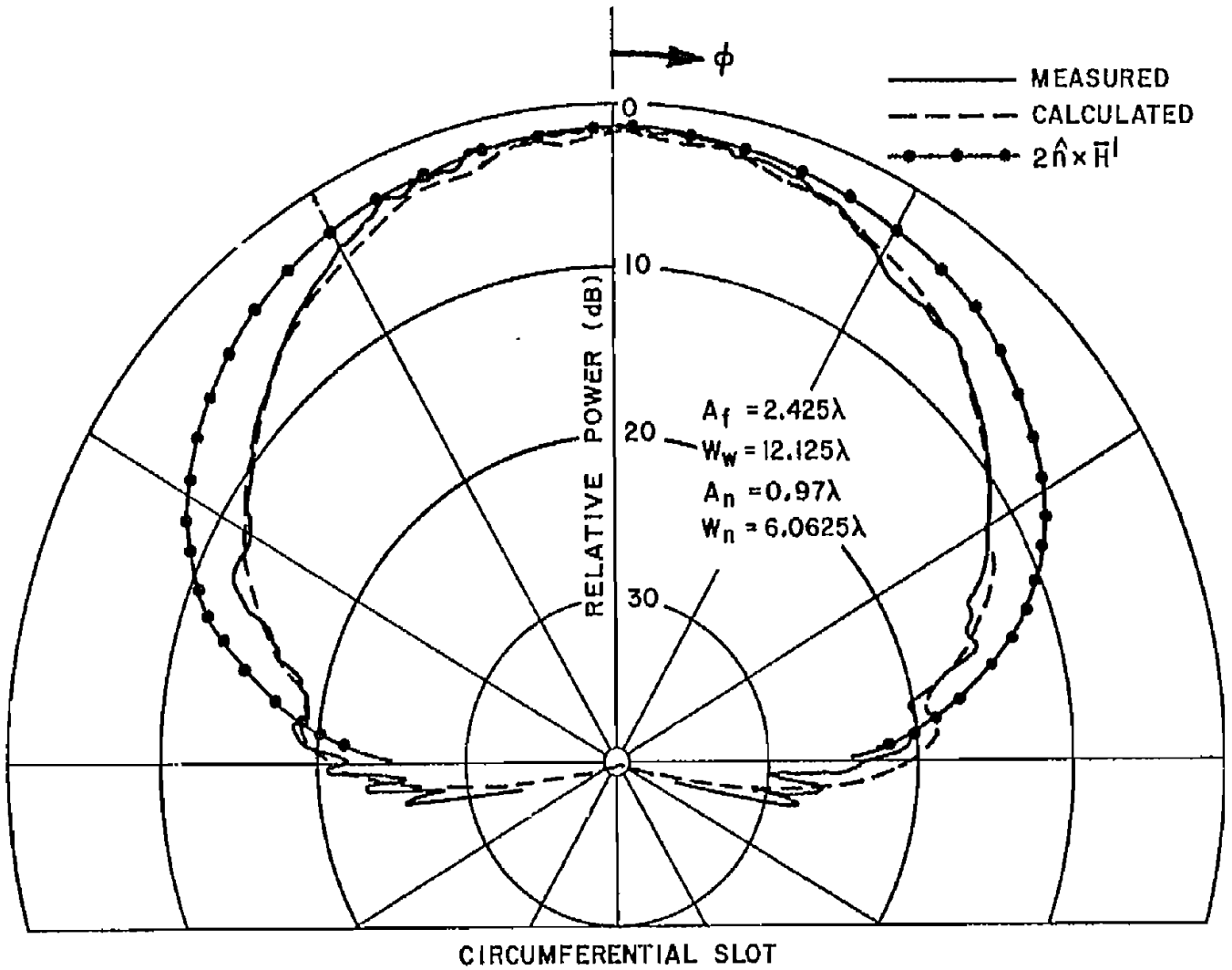

Fig. 61. Roll plane pattern.

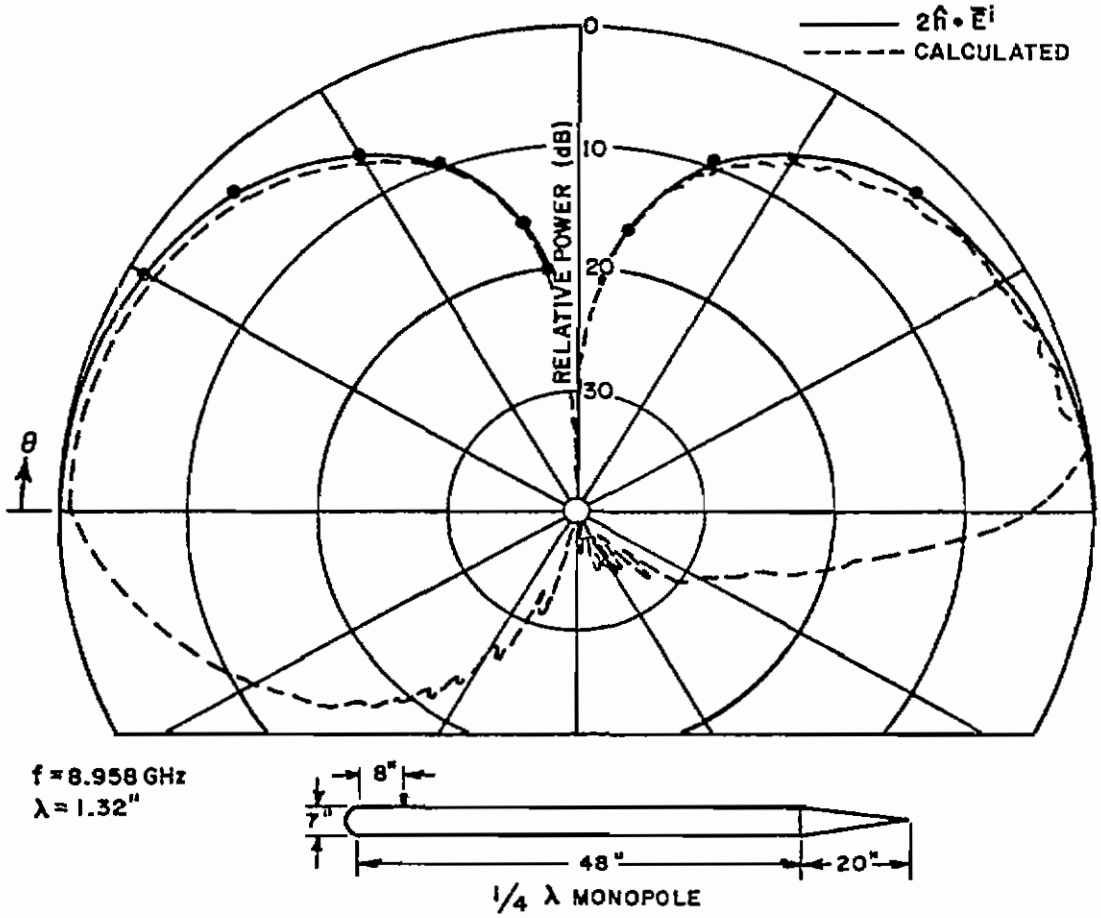

Fig. 62. Elevation plane pattern.

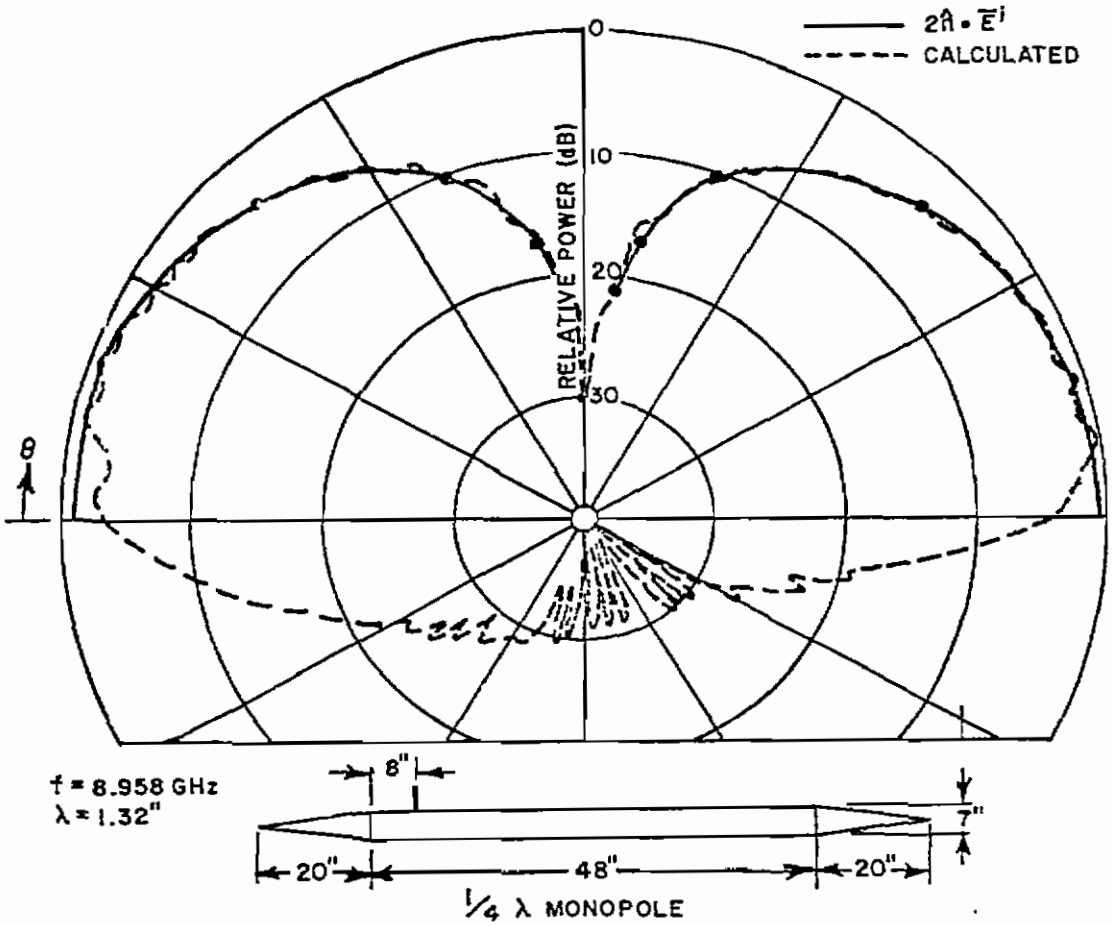

Fig. 63. Elevation plane pattern.

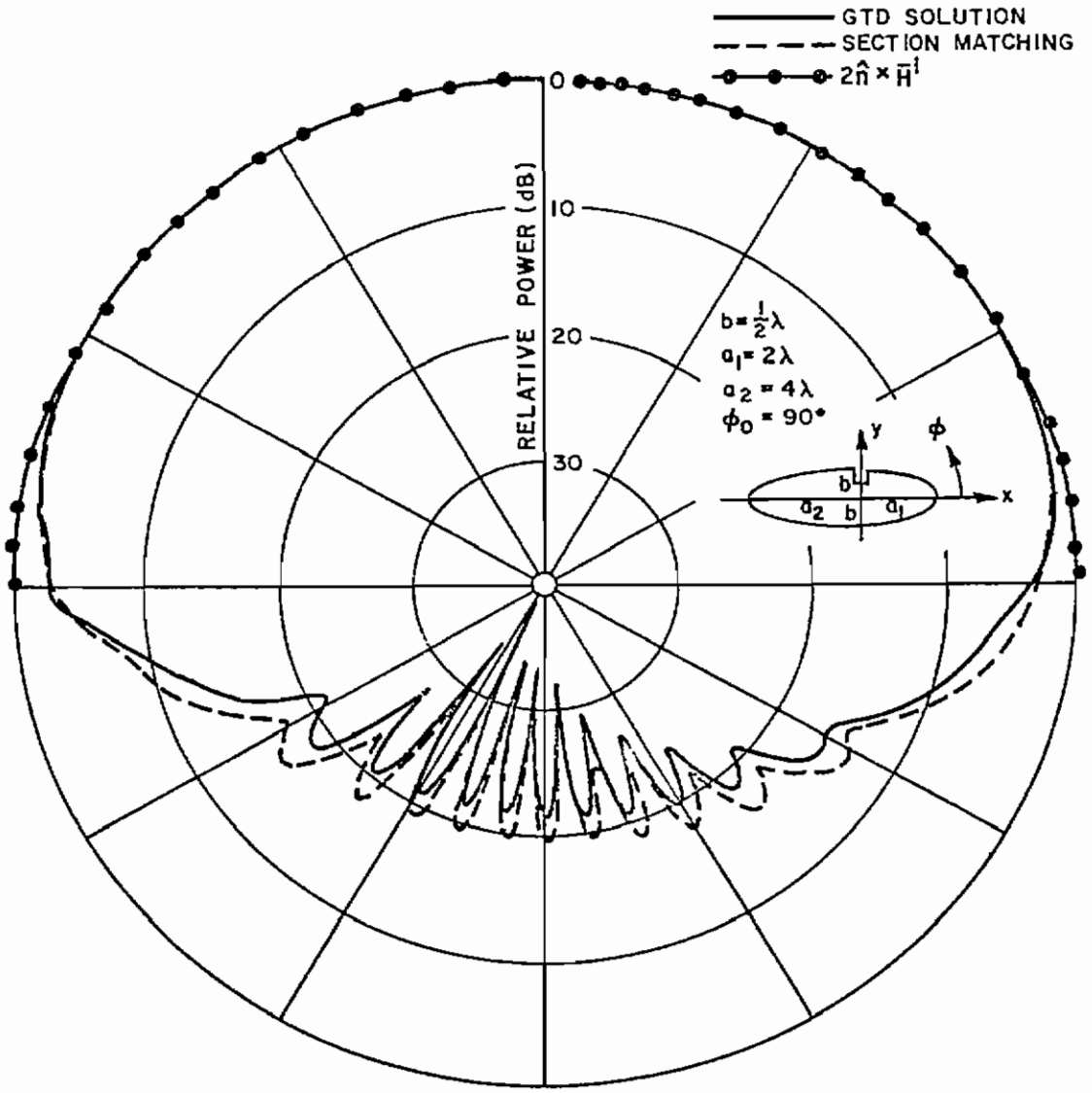

Fig. 64. Elevation plane pattern with a circumferential slot mounted on a composite ellipse model.

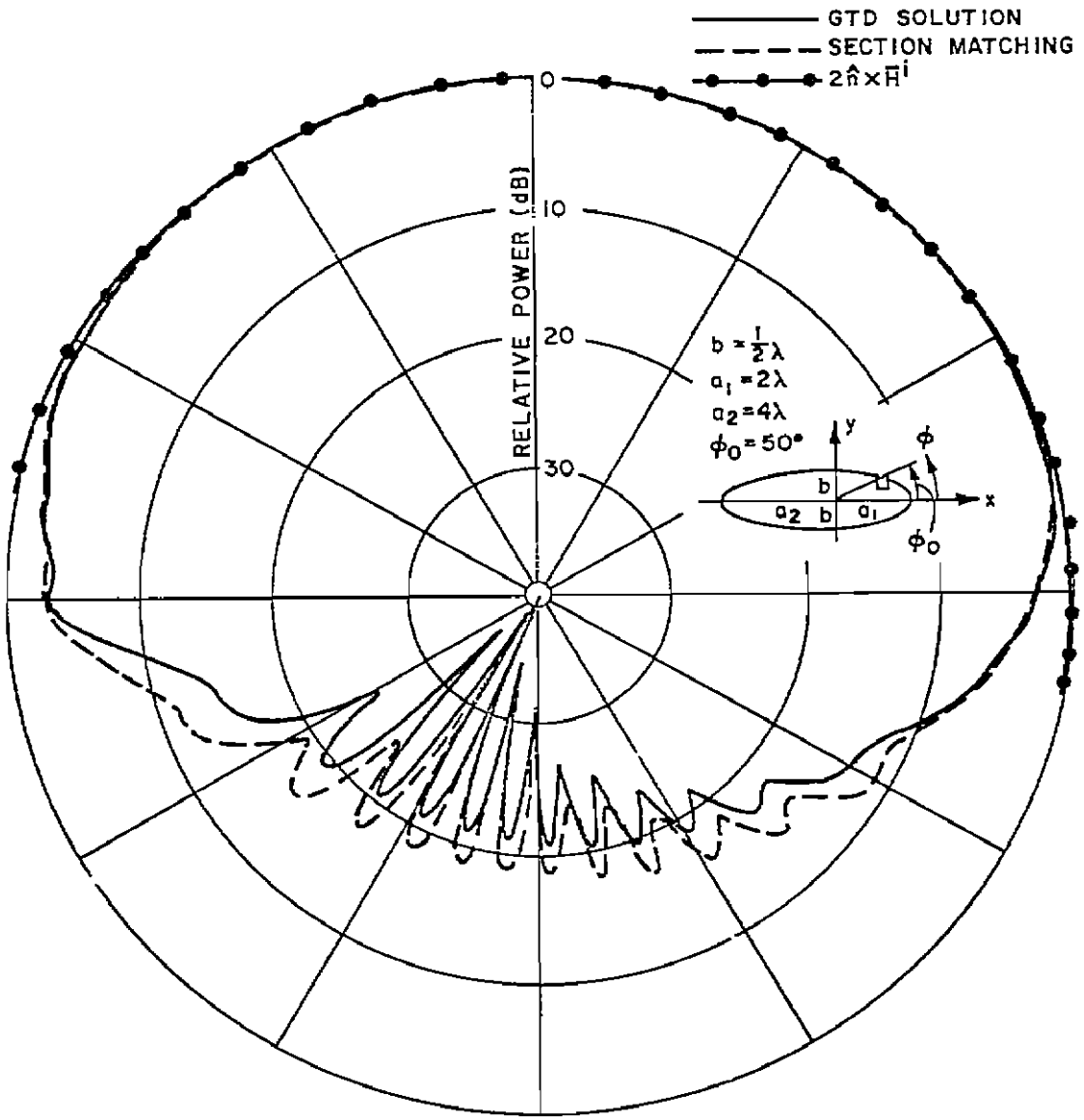

Fig. 65. Elevation plane pattern with a circumferential slot mounted on a composite ellipse model.

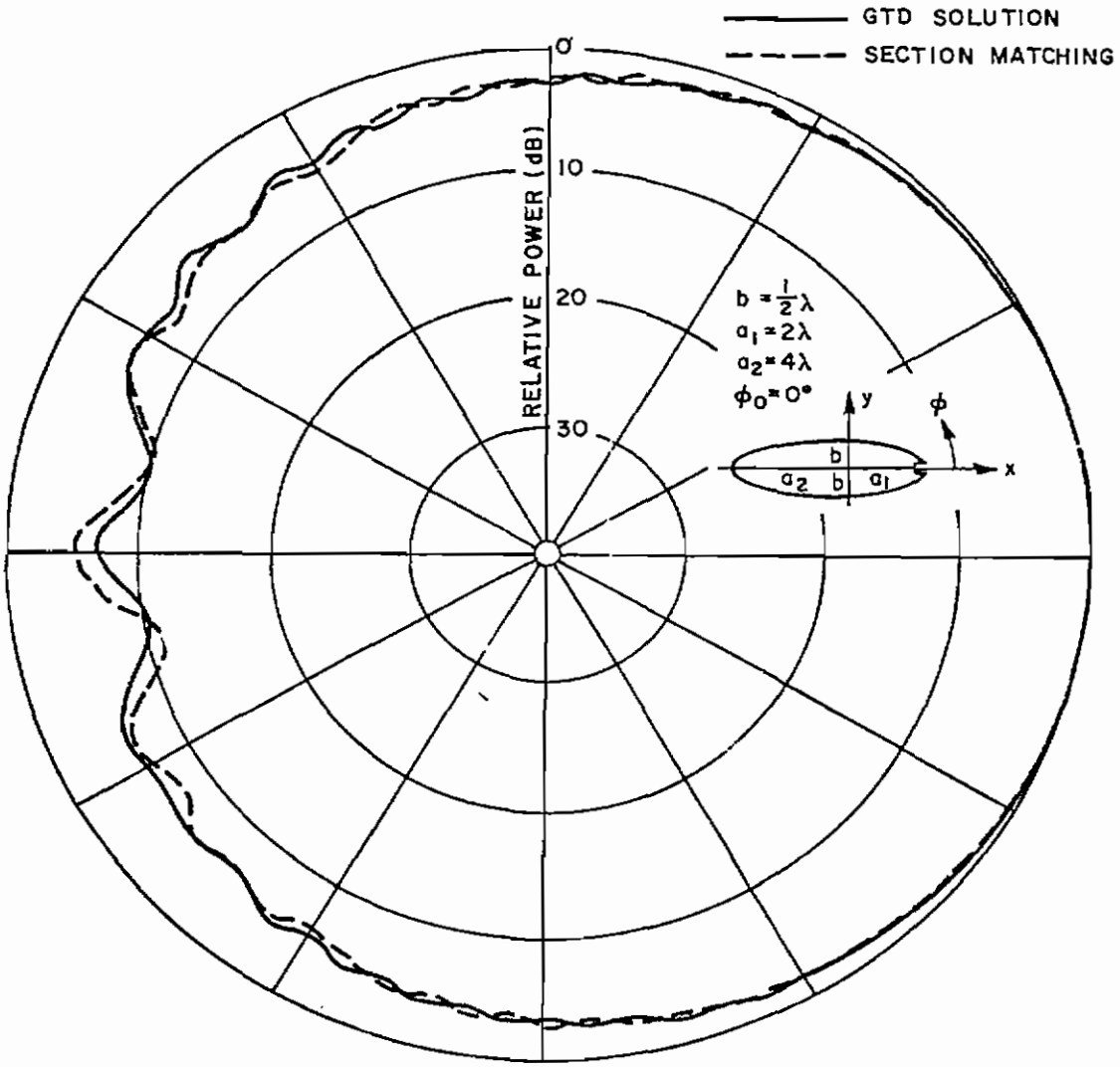

Fig. 66. Elevation plane pattern with a circumferential slot mounted on a composite ellipse model. (Case where physical optics will fail.)

where the radius of curvature at the slot location (observation point) is less than one wavelength. Note that physical optics would predict zero current for an incoming planewave from $\phi = 180°$, yet the more accurate computations indicate that the current is down only $\sim$5 dB from the maximum ($\phi = 0°$). On the other hand note that in Fig. 65 where the radius of curvature is greater than one wavelength the fields are down by $\sim$20 dB when the observation point is in the shadow region. This also means that the calibration of the calculated curves by physical optics, as suggested earlier, would fail for the slot position of Fig. 66.

The surface charge and current density decay rapidly as the observation point moves further into the shadow region. Since the spectrum of the EMP is also low at frequencies where optical calculations are valid, it would appear that inclusion of current and charge densities in the deep shadow may be of academic interest. This is fortunate since this is the region where the GTD computations will be least accurate.

In summary, for each of the principle patterns studied, a model was chosen which was representative of a wide variety of modern aircraft structures. The analysis of these models allow, within limits, for arbitrary locations and size of the various structural components. The location of the observation point is confined to or near the plane of symmetry which includes the vertical stabilizer. Whenever possible the solutions have been verified by measurements. It should be clear that the methods used to calculate the effects of the wings can be used to calculate the effects of the tail section.

IV. RECENT THEORETICAL DEVELOPMENTS

This section deals with a brief review of some recent analytical results which serve to further extend the applicability of the GTD. These extensions are relevant to some of the problems discussed in Section III; however, these results were not incorporated therein as they were available after the measurements and analyses discussed in Section III were completed. Some other work extending the applicability of GTD may be found in References [28] and [29].

First, we shall briefly discuss some extensions to the wedge diffraction results presented earlier in Section II.B. A useful feature of the form of D_s of Eq. (25b) which appears in the expression of the dyadic wedge diffraction coefficient, $\bar{\bar{D}}_E$ of Eq. (25a), is that it offers clues for readily obtaining a dyadic diffraction coefficient for a curved conducting surface bounded by a curved edge. This extension is of course based on the fact that diffraction at high frequencies is a local phenomenon, and the curved edge is locally wedge shaped at the point of diffraction. It is motivated by the fact that most junctions in vehicles occur between curved surfaces. The usefulness of this extension results from the fact that the total field can be made continuous at the shadow and reflection boundaries (just as for the perfectly conducting wedge, as discussed in Section II) even though the radii of curvatures of the incident, reflected, and diffracted wavefronts are markedly different for the curved edge on an otherwise smooth curved surface. The continuity in the total field is made possible by a proper choice of the distance parameter, L (L for the wedge is given in Eq. (30)) appearing in the arguments of the transition function, $F(ka^{\pm}(\beta))$ of Eq. (27). For the sake of brevity the details involved in deducing the correct form of the parameter L will not be dealt with in this report; these details form the subject of a paper which is currently in preparation[30]. We shall briefly discuss a specific application of this new result. Consider the geometry of Fig. 67(a) which depicts an infinitesimal electric current moment

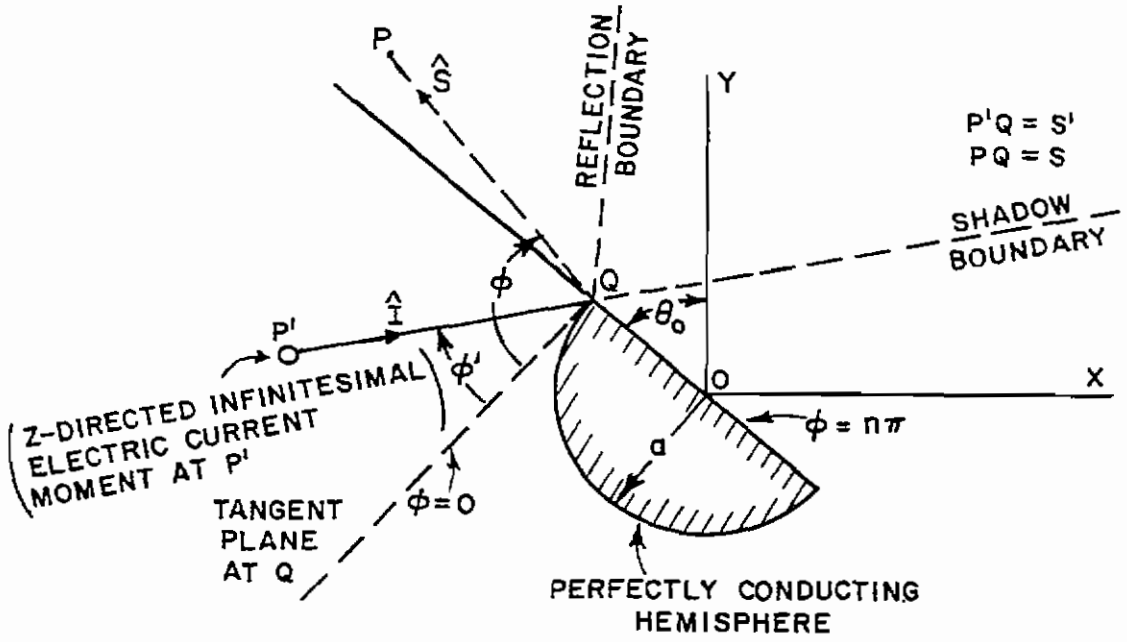

(a)

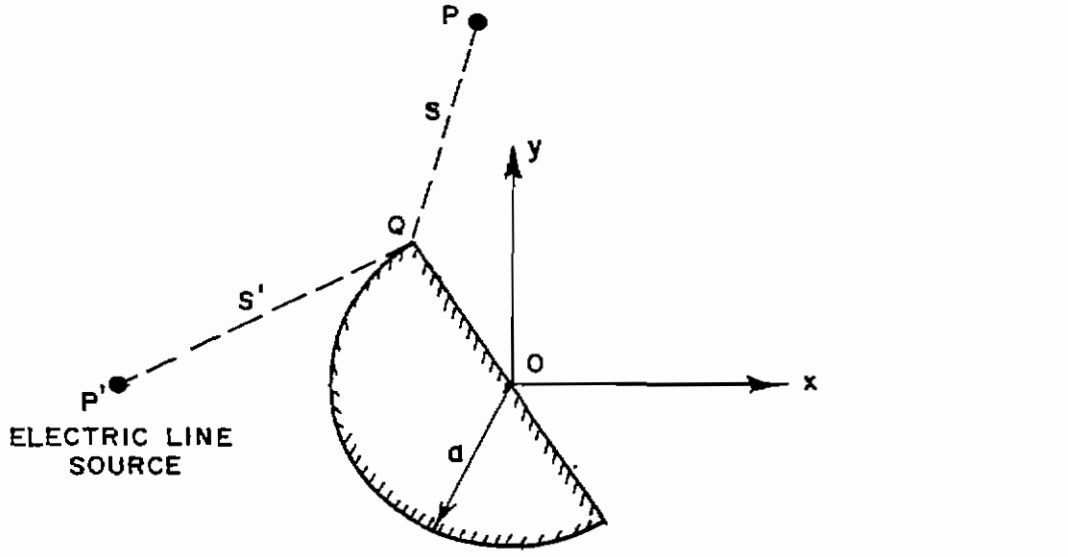

(b)

Fig. 67. Geometry of hemisphere and half cylinder.

illuminating a perfectly conducting hemisphere. The current moment is $\hat{Z}$-directed, and the analysis is restricted to the X-Y plane for convenience. The point Q on the edge is a point of diffraction. One may form an effective right angle wedge at Q with the faces $\phi = 0$ and $\phi = n\pi$ as indicated. $(n = 3/2)$; the face $\phi = 0$ is a plane tangent to the hemisphere at Q (where Q lies in the X-Y plane). P and P' are the observation and source points, respectively. The direction of observation is indicated by the angle measured clockwise from the $\phi = 0$ face. For aspects near the shadow and reflection boundaries, $\phi > \phi'$. The reflection boundary occurs when $\phi + \phi' = \pi$ whereas the shadow boundary occurs at $\phi - \phi' = \pi$. Referring to Eq. (25) it is seen that the transitions functions $F[\kappa a^-(\beta^+)]$ and $F[\kappa a^-(\beta^-)]$ serve to keep the diffracted field finite at the reflection and shadow boundaries, respectively (since $d^-(\beta^+)$ and $d^-(\beta^-)$ are unbounded at the reflection and shadow boundaries, respectively). However, to ensure a continuity of the total field across the transition boundaries for the geometry in Fig. 67(a), one must extend the results of Eq. (30) to incorporate a proper distance parameter, L in the arguments of $F[\kappa a^-(\beta^\pm)]$. (Note that $\kappa = kL$, k being the free space wave number.) It can be shown[30] that for the geometry in Fig. 67(a), and for field points in the far zone of the target,

$$(44) \qquad L = \frac{\rho_1 \rho_2}{\rho_c}, \quad \text{for the } F[kLa^-(\beta^+)] \text{ term,}$$

and

$$(45) \qquad L = \frac{(s')^2}{\rho_c}, \quad \text{for the } F[kLa^-(\beta^-)] \text{ term } (s' = P'Q),$$

in which ρ_c is different in Eqs. (44) and (45) (see Eq. (46) below). Explicit forms for the L parameters appearing in $F[\kappa a^+(\beta^-)]$ and $F[\kappa a^+(\beta^+)]$ terms can also be determined easily; however, for the present problem these transition functions are approximately equal to one (as their arguments $\kappa a^+(\beta^-)$ and $\kappa a^+(\beta^+)$ exceed the value

10.0; and $F[\kappa a] \to 1$ as $\kappa a \to 10$ according to Fig. 7). For the general case, the L parameters for the $F[\kappa a^{+}(\beta^{\pm})]$ terms are chosen in a manner consistent with the reciprocity principle. The caustic distances ρ_1 and ρ_2 are associated with the wavefront reflected from the hemispherical surface, whereas the caustic distance ρ_c is associated with the wavefront diffracted from Q. The caustic distance ρ_1 and ρ_2 are easily determined via Eqs. (15) and (16) respectively. (Note that P'O of Eqs. (15) and (16) is identical to P'Q of Fig.67(a), and $R_1 = R_2 = a$.) The caustic distance ρ_c is given by Kouyoumjian[19]

$$(46) \qquad \frac{1}{\rho_c} = \frac{1}{P'Q} - \frac{\hat{n}_e \cdot (\hat{I} - \hat{S})}{R \sin^2 \beta_o},$$

where $\hat{n}_e$ = unit vector normal to the edge at Q' and directed away from the center of edge curvature.

R = radius of curvature of the edge (= a, in Fig. (a))

$\hat{I}$ = unit vector along the incident ray P'Q

$\hat{S}$ = unit vector along the diffracted ray QP.

β_o is illustrated in Fig. 5; $\beta_o = \pi/2$ in the above discussion.

The unit vector $\hat{S}$ changes direction as one moves from the reflection to the shadow boundary. Hence, ρ_c for Eqs. (44) and (45) are different as is evident from Eq. (46). In particular, ρ_c in Eq. (44) is calculated at the reflection boundary whereas, for Eq. (45), it is calculated at the shadow boundary. The field of the ray incident at Q may be taken as

$$(47) \qquad A_o \frac{e^{-ik(P'Q)}}{(P'Q)} \quad ,$$

according to the geometrical optics representation. The reflected field may be found from geometrical optics via Eq. (14). The total field consists of the sum of the geometrical optics field and the

diffracted field. (Note that for $y > 0$, the reflected field vanishes when $\phi > \pi - \phi'$ and the incident field vanishes when $\phi > \pi + \phi'$.) If instead of the 3-D geometry of Fig. 67(a) one considers the 2-D geometry of Fig. 67(b) which involves a half cylinder (of the same radius as the hemisphere in Fig. 67(a)) excited by a uniform electric current line source, the L parameters are given by

(48) $\quad L = \rho_1 \ , \quad$ for $F[kLa^-(\beta^+)]$ term,

and

(49) $\quad L = s' = P'Q \ , \quad$ for $F[kla^-(\beta^-)]$ term.

(Note that $\rho_c = s'$ and is the same at the reflection and shadow boundaries. Also $\rho_2 \to \infty$ in the 2-D problem of Fig. 59(b).) The $F[kLa^+(\beta^+)]$ and $F[kLa^+(\beta^-)]$ terms are approximately one. The problem of Fig. 67(b) is easier to analyse than the one in Fig. 67(a) since a caustic of the diffracted rays can occur behind the hemisphere, and the field near the caustic must be treated via the method of equivalent-currents (discussed in Section II.C). We have employed the ray-optic procedure for calculating the total fields surrounding the half-cylinder of Fig. 67(b) for the dimensions indicated in Fig. 68. The results indicate an excellent agreement with the numerical solution of the integral equation for the same configuration, thereby indicating the accuracy of the new results which have been described.

We shall next consider some extensions to the GTD results for curved conducting surfaces. Consider the case when the point source in Fig. 8(a), in Section II, moves from P' to the point Q' on the smooth, curved, perfectly conducting surface. The point source may be an infinitesimal tangential magnetic current moment, or an infinitesimal electric current moment directed normal to the surface.

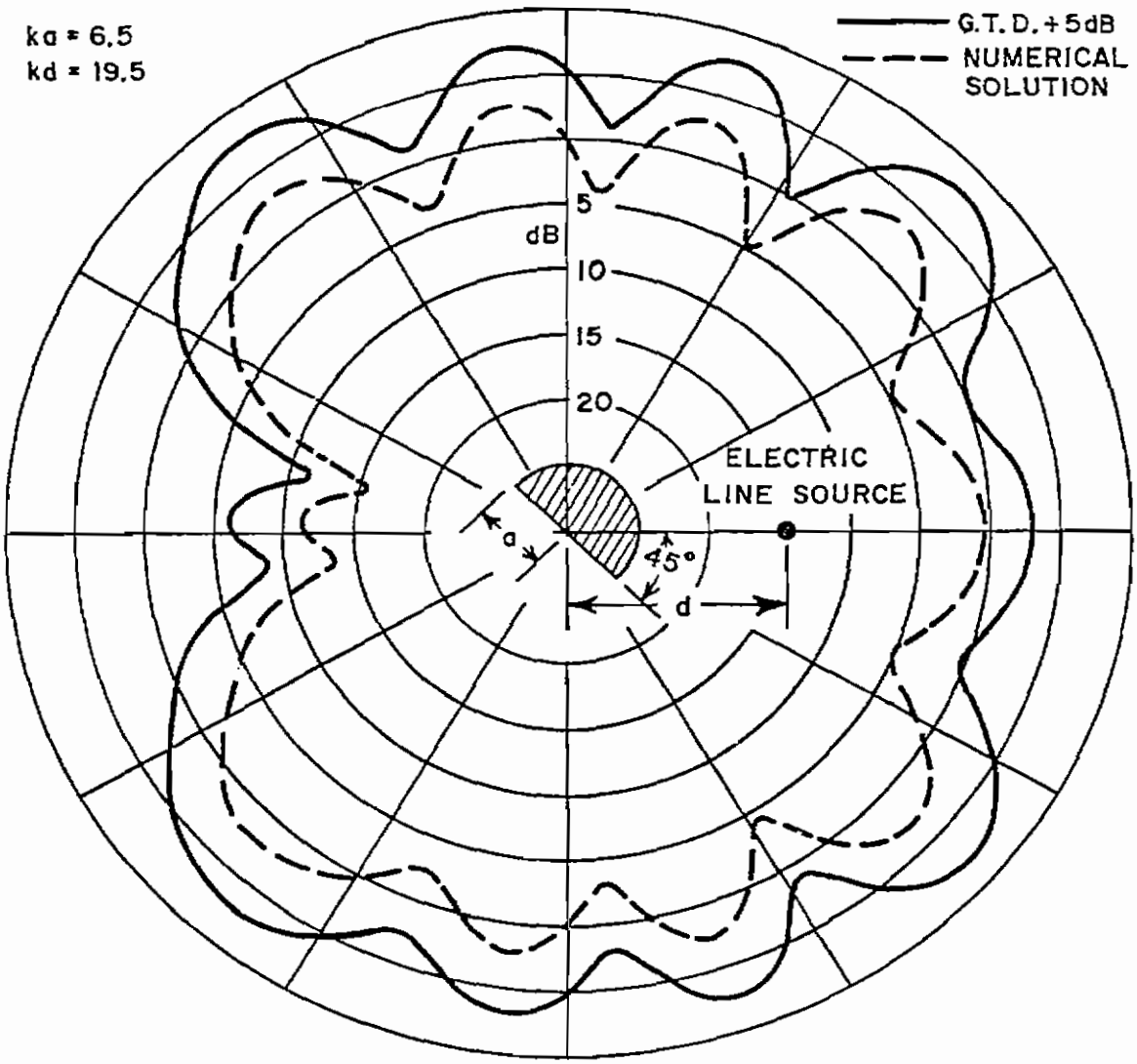

Fig. 68. The pattern of an electric line current illuminating a half cylinder.

For the sake of definiteness, let the source at Q' represent a tangential magnetic current moment of strength $d\bar{p}_m$ (Q'). The shadow boundary divides the space surrounding the curved surface into the illuminated and shadow regions as indicated in Fig. 8(a). On either side of the shadow boundary is the transition region.

Geometrical optics is used to describe the direct radiation from the source at Q' (via the direct ray from Q' to the observation point) in the illuminated region, whereas the surface ray modes of GTD describe the diffracted field in the shadow region. In the transition region, the creeping wave solution involving Fock type functions is utilized. These solutions blend smoothly so that a continuous total field is obtained in the entire region of space surrounding the curved surface. Let a point Q_o lie on the surface between the points Q' and Q as indicated in Fig. 69. The electric

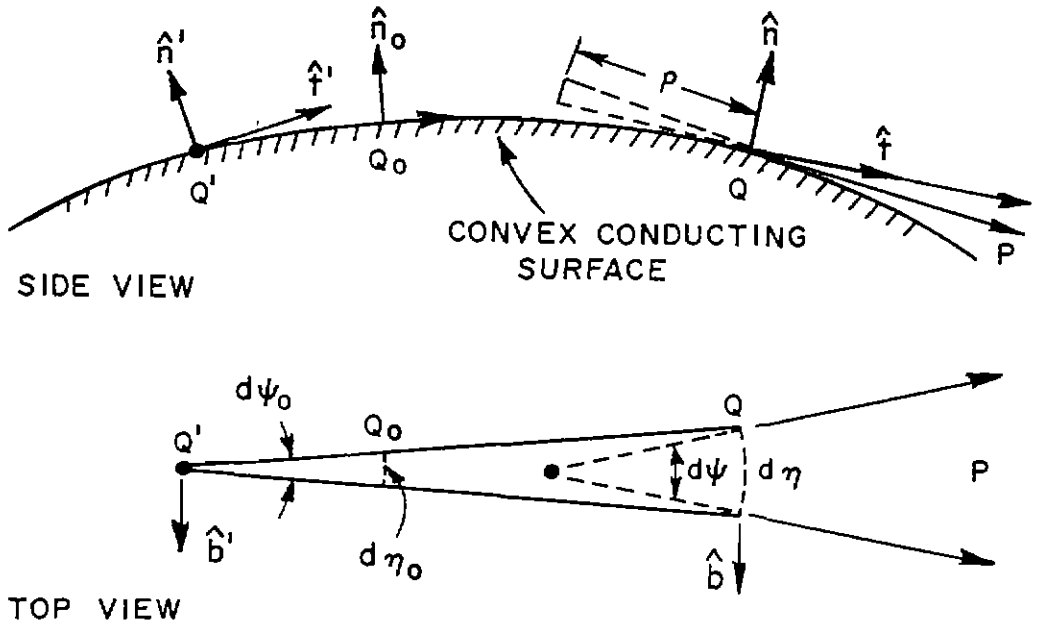

$$Q'Q_o = t_o\ ,\quad Q'Q = t,\quad QP = s$$

Fig. 69. Ray geometry for diffraction by convex conducting surface.

field, $\bar{E}(P)$ at a point P in the shadow region may be written in terms of a reference field at Q_o in a manner similar to that of Eq. (35) as

$$(50) \qquad \bar{E}(P) \sim \sum_{p=1}^{\infty} \bar{E}(Q_o) \cdot \left[\sqrt{\frac{d\eta_o}{d\eta}} \left\{ \hat{n}_o \hat{n}\, D_p^h(Q)\, e^{-\int_{Q_o}^{Q} \alpha_p^h\, ds} + \hat{b}_o \hat{b}\, D_p^s(Q)\, e^{-\int_{Q_o}^{Q} \alpha_p^s\, ds} \right\} e^{-jkQQ_o} \sqrt{\frac{\rho}{s(\rho+s)}}\; e^{-jks} \right].$$

The present analysis is restricted to geodesics Q'Q for which $\hat{b} = \hat{b}_o$, i.e., to geodesics without torsion. The quantities t_o, $d\psi_o$, $d\psi$, $d\eta_o$, $d\eta$, and ρ are shown in Fig. 69.

If we let Q_o approach Q' which is a caustic of the diffracted ray system, then $\bar{E}(Q_o)$ becomes unbounded. However,

$$\lim_{Q_o \to Q'} \bar{E}(Q_o) \sqrt{d\eta_o}$$

exists, since $\bar{E}(P)$ is independent of the location of the reference point Q_o. $d\eta_o = t_o\, d\psi_o$ so that we may write

$$(51) \qquad \lim_{\substack{Q_o \to Q' \\ t_o \to 0}} \bar{E}(Q_o) \cdot \hat{n} \sqrt{\frac{t_o\, d\psi_o}{d\eta}} = C_p^h \sqrt{\frac{d\psi_o}{d\eta}},$$

and

$$(52)\qquad \lim_{\substack{Q_o \to Q' \\ t_o \to 0}} \bar{E}(Q_o) \cdot \hat{b} \sqrt{\frac{t_o \, d\psi_o}{d\eta}} = C_p^s \sqrt{\frac{d\psi_o}{d\eta}}$$

Thus,

$$(53)\qquad \bar{E}(P) \sim \sum_{p=1}^{\infty} \left[\sqrt{\frac{d\psi_o}{d\eta}} \left\{ \hat{n}\, C_p^h(Q')\, e^{-\int_{Q'}^{Q} \alpha_p^h \, ds} D_p^h(Q) + \hat{b}\, C_p^s(Q')\, e^{-\int_{Q'}^{Q} \alpha_p^s \, ds} D_p^s(Q) \right\} e^{-jk(Q'Q)} \right] \sqrt{\frac{\rho}{s(\rho+s)}}\, e^{-jks}.$$

$C_p^h(Q')$ represents the coupling from the source at Q' to the surface ray modes of GTD and is therefore proportional to the strength of the source; the constant of proportionality is defined as

$$\frac{-jk}{2\pi} L_p^h,$$

where L_p^h is the "Launching Coefficient"[31]. Thus,

$$(54)\qquad C_p^h(Q') \equiv \frac{-jk}{2\pi} L_p^h(Q')\, \hat{b} \cdot d\bar{p}_m(Q'),$$

and

$$(55)\qquad C_p^s(Q') \equiv \frac{-jk}{2\pi} L_p^s(Q')\, \hat{t}' \cdot d\bar{p}_m(Q').$$

The subscript and superscript on L_p^h have the same meaning as before. L_p^h may be viewed as a transfer function relating the actual surface

field to the field of the surface ray modes (GTD representation). Note that $\hat{b} \cdot \bar{E}(Q_o)$ is non-zero, i.e., the tangential electric field of the surface rays (GTD) is not the true surface field but represents a boundary layer field; this indicates the importance of introducing the Launch coefficients. Re-writing Eq. (53) more compactly for the computation of the surface ray fields,

$$\bar{E}(P) \sim \frac{-jk}{2\pi} \, d\bar{p}_m(Q') \cdot [\hat{b}\,\hat{n}\,F(Q'Q) + \hat{t}'\,\hat{b}\,G(Q'Q)] \sqrt{\frac{\rho}{s(\rho+s)}}\, e^{-jks}, \tag{56}$$

where

$$F(Q'Q) = \sqrt{\frac{d\psi_o}{dn}} \sum_{p=1}^{\infty} L_p^h(Q')\, D_p^h(Q)\, e^{-jkQ'Q}\, e^{-\int_{Q'}^{Q} \alpha_p^h \, ds}, \tag{57}$$

and

$$G(Q'Q) = \sqrt{\frac{d\psi_o}{dn}} \sum_{p=1}^{\infty} L_p^s(Q')\, D_p^s(Q)\, e^{-jkQ'Q}\, e^{-\int_{Q'}^{Q} \alpha_p^s \, ds}. \tag{58}$$

The Launching coefficients are obtained via asymptotic solutions to appropriate canonical problems. The Launching coefficients are given in terms of Airy Functions similar to those occuring in $D_p^{h,s}$ as shown in Tables A and B; they also depend on the local radius of curvature, and it's derivatives ith respect to arc length (at Q'). Explicit forms for $L_p^{h,s}$ and their determination form the subject of a paper currently being prepared under another project; hence, the details are omitted for the sake of brevity.

The series representations for F(Q'Q) and G(Q'Q) of Eqs. (57) and (58) are replaced by their equivalent integral representations as P moves into the transition region. These integral representations are rapidly convergent in the transition region and correspond to the

creeping waves of Fock. In the illuminated region, F and G are replaced by 1 and cosθ, respectively. (θ = angle made by the normal at Q' with the direction of observation in the far-zone.) Some applications of this new formulation are illustrated in Figs. 70-76.

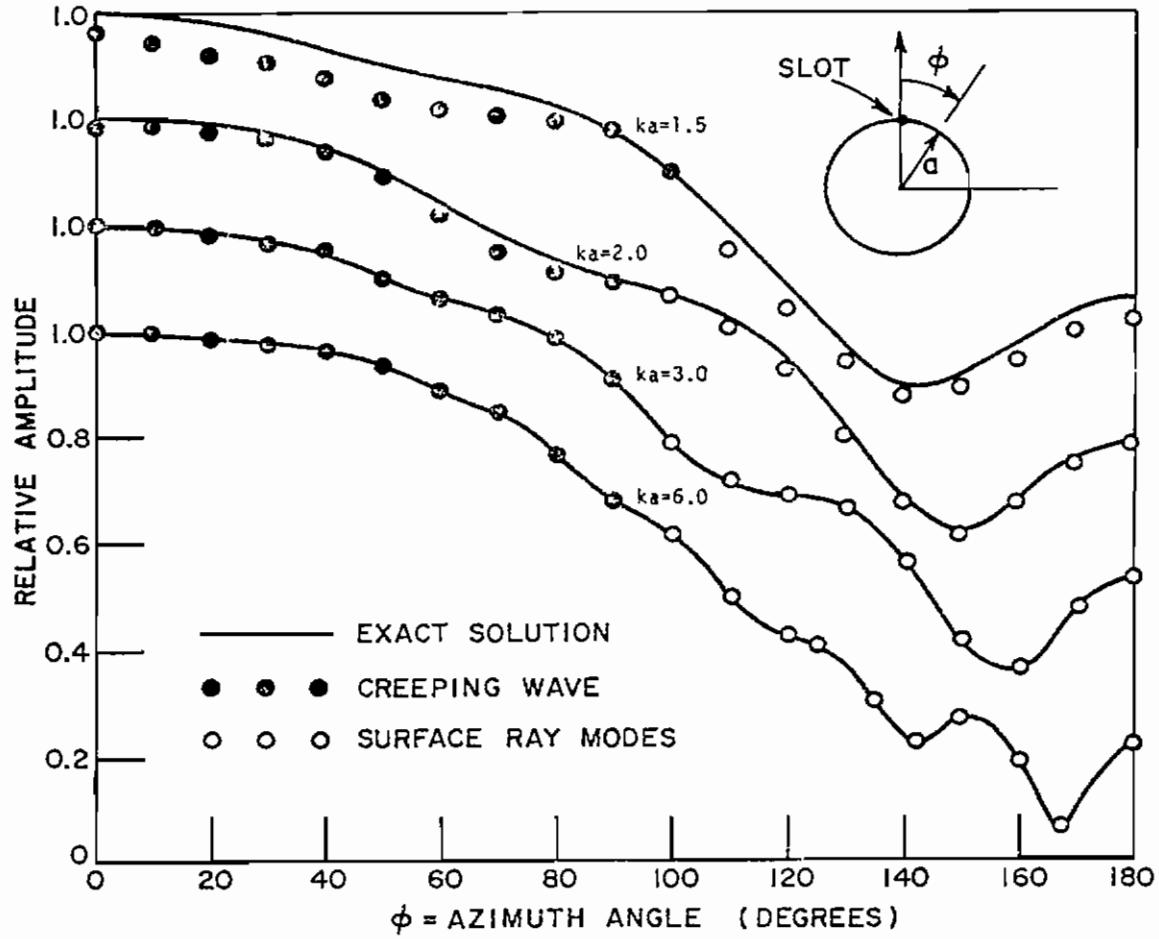

Fig. 70. Radiation Patterns of a thin axial slot in a perfectly conducting circular cylinder.

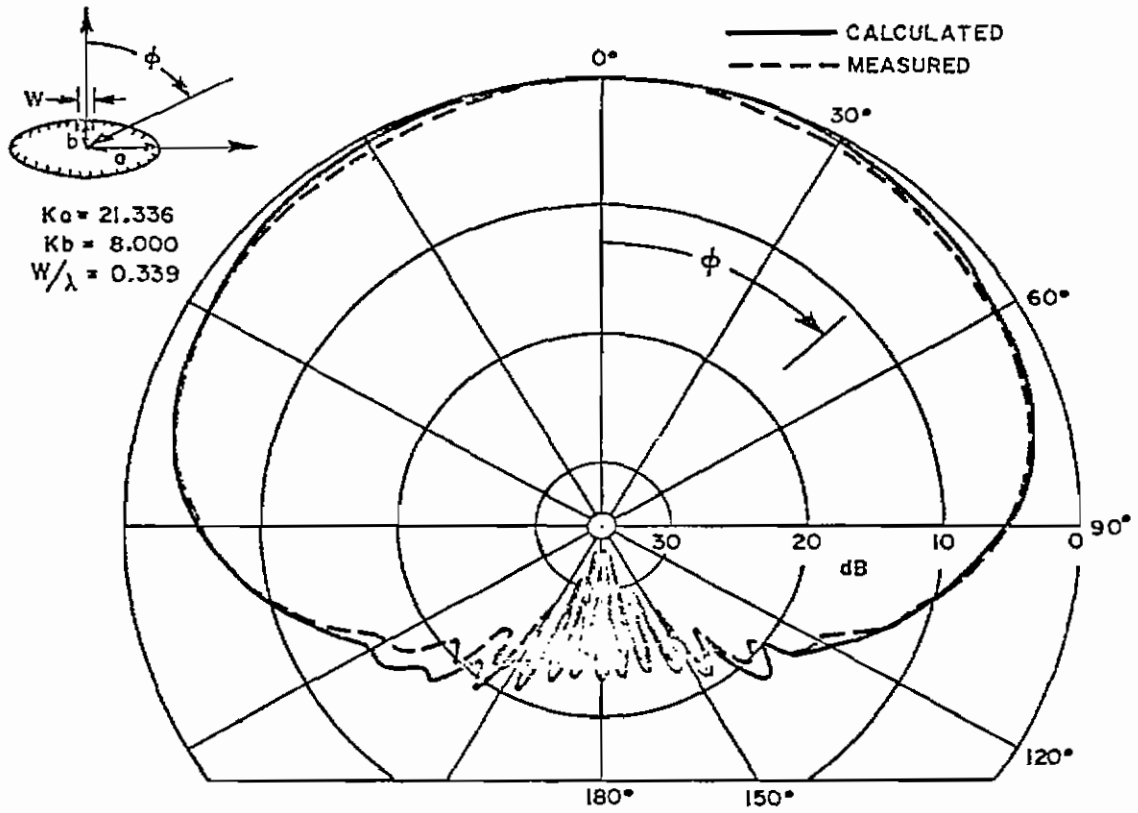

Fig. 71. Pattern of an axial slot on an elliptic cylinder.

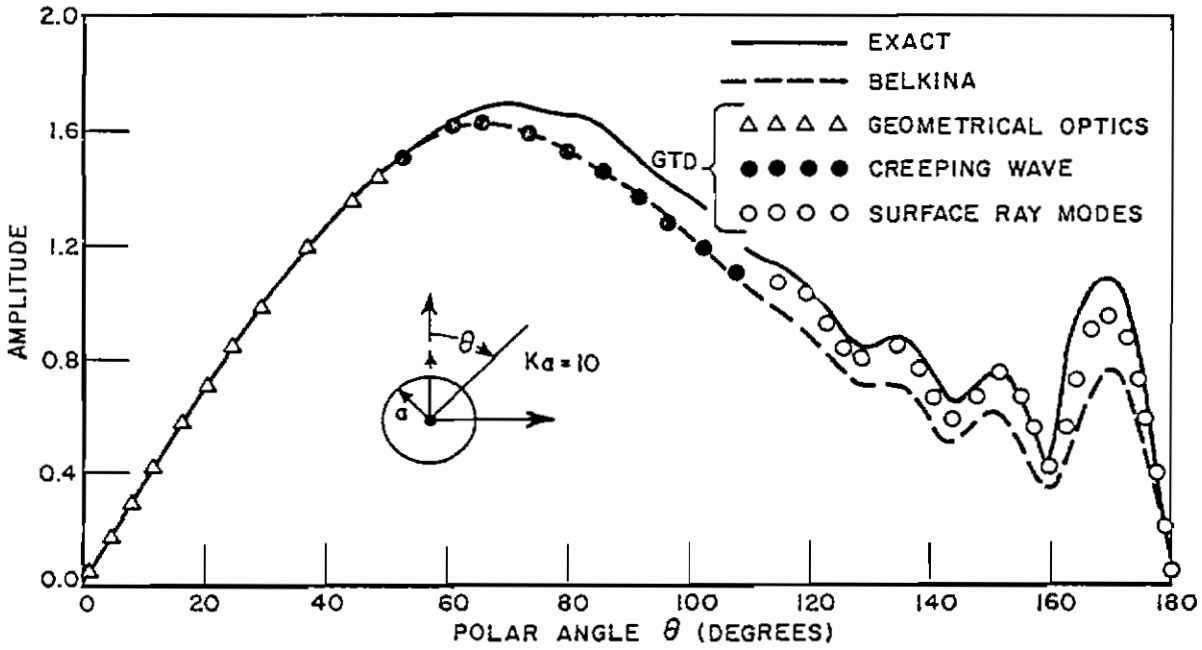

Fig. 72. Slide pattern of a radial electric dipole on a sphere.

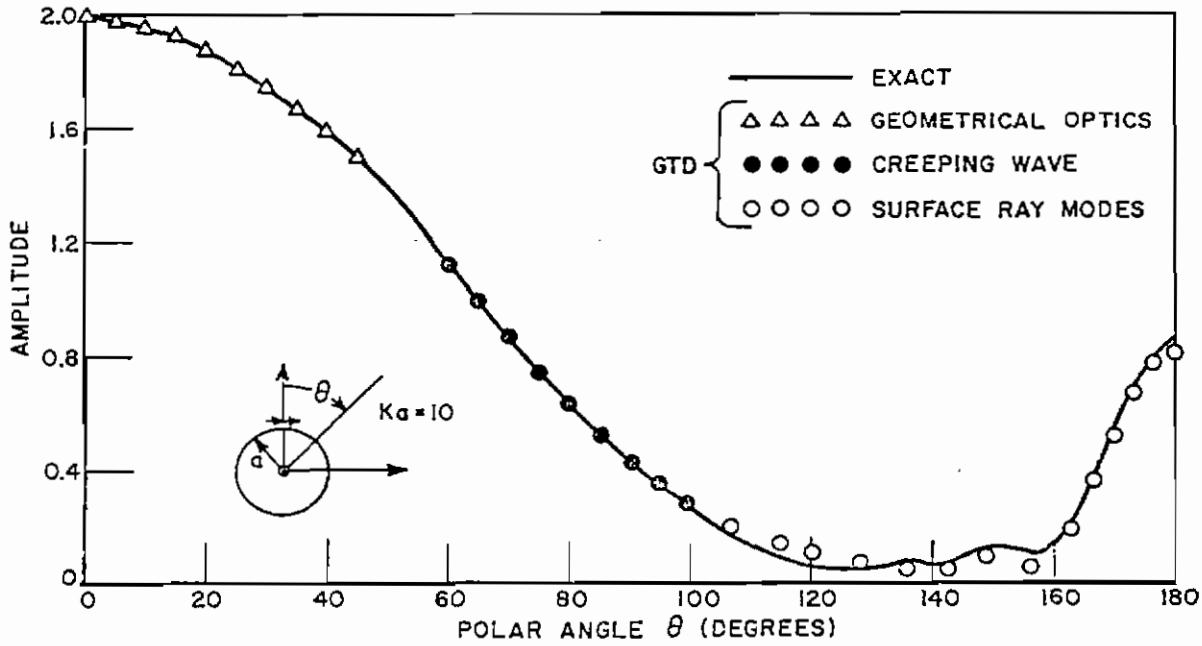

Fig. 73. Pattern of an infinitesimal slot on a sphere in a plane parallel to the slot.

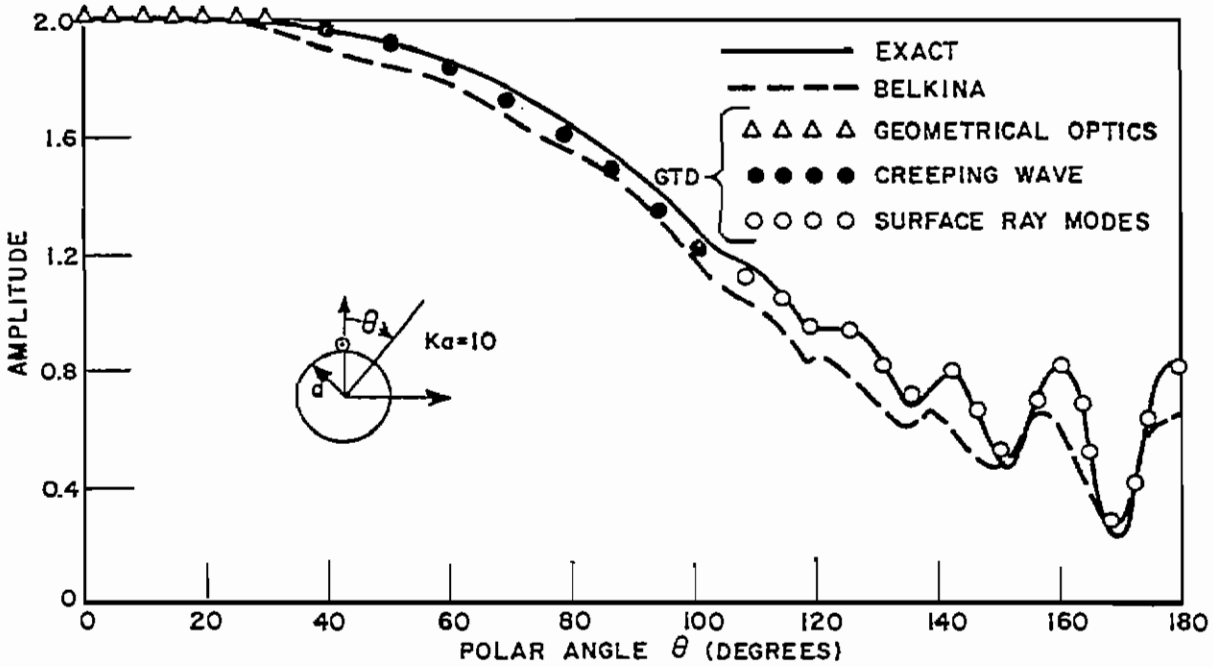

Fig. 74. Pattern of an infinitesimal slot on a sphere in a plane perpendicular to the slot.

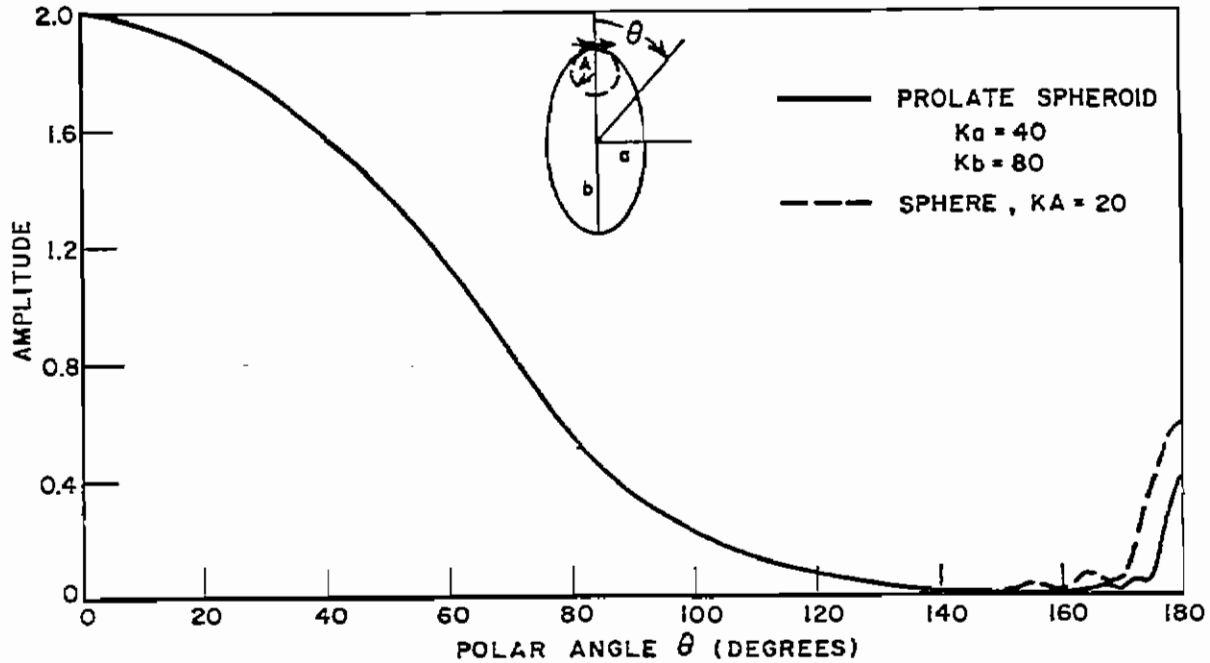

Fig. 75. Pattern in plane parallel to the slot.

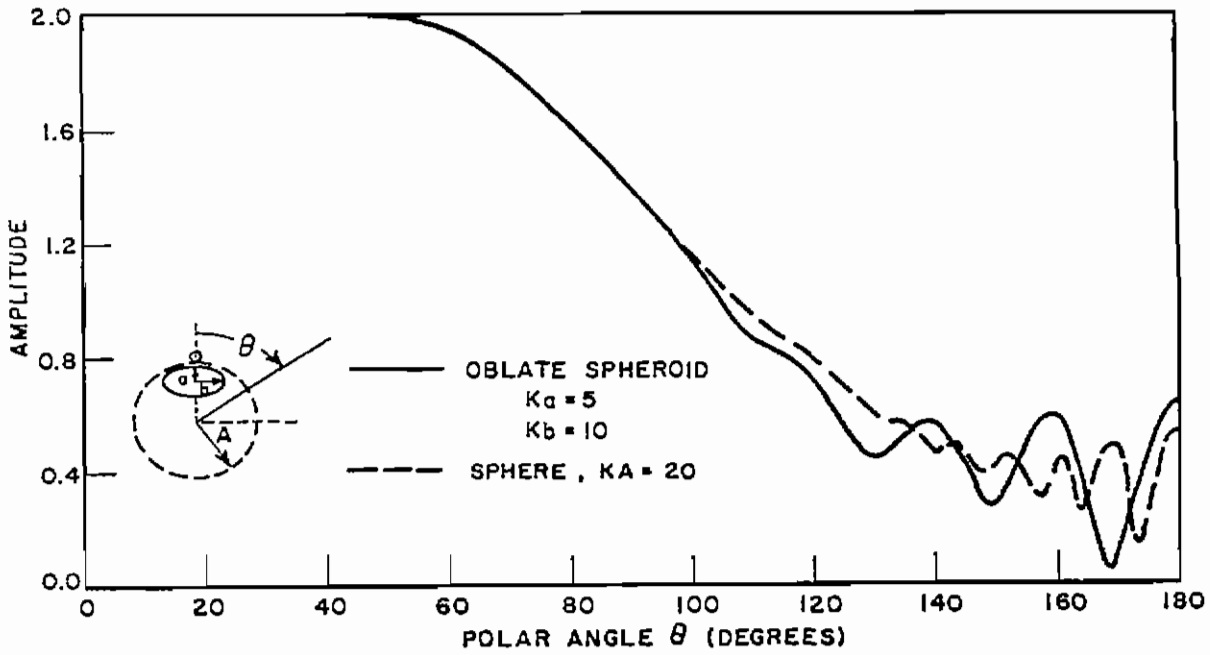

Fig. 76. Pattern in plane ⊥ to the slot.

Figure 70 indicates the radiation patterns of a thin axial slot on perfectly conducting circular cylinders calculated via ray-optics formulation just discussed, and the results are compared against the exact solutions. It is remarkable that the ray-optical solution is very good even for cylinders as small as three wavelengths in circumference. Corrections to geometrical optics (via second and third terms of the Luneberg-Kline series[32]) field would improve the accuracy of the result for cylinders of even smaller sizes. Figure 71 illustrates the radiation pattern of an axial slot on a perfectly conducting elliptic cylinder computed via ray-optics and compared with experimental results. The descrepencies between the two halves (on either side of $\phi = 0$) of the measured patterns are approximately the same as the descrepancies between measurements and calculations; hence, the overall agreement appears to be very good. Figure 72 indicates the radiation pattern of a vertical electric dipole on a perfectly conducting sphere.

Figures 73 and 74 indicate the radiation patterns of an infinitesimal slot on a sphere computed in the principal planes. Again, the calculated results in Figs. 72, 73 and 74 compare very well with the exact solutions as shown. Figures 75 and 76 indicate the radiation patterns of infinitesimal slots on prolate and oblate spheroids, respectively. These patterns are compared against patterns for spheres of the same local radii of curvatures as those of the spheroids at the slot location. The fields surrounding the antennas on cylinder, spheres and spheroids are everywhere continuous via the new formulation which overcomes the discontinuity problem encountered in a previous technique described in Section II.C.

V. SUMMARY AND CONCLUSIONS

Methods for computing the surface charge and current density induced on the surface of aircraft-like bodies have been presented which are valid for frequencies above the resonance region. This material has been presented from three points of view; 1) summary of previous work, 2) method currently used for computation and 3) new extensions of GTD. Much of the material associated with the previous work of computing radiation patterns is directly applicable and is used here as a vehicle for outlining the concepts in use. The current computational techniques are of prime interest in that they incorporate modal analysis and GTD techniques. This leads to a model that is applicable to bodies that are just beyond the sizes that could be treated using integral equation techniques, i.e., fuselage length and wing span in excess of a wavelength with a fuselage diameter that is small in terms of wavelength. For such small diameter fuselages, the previous creeping wave analysis of Keller would yield questionable results. However, the second order terms developed by Voltmer and Kouyoumjian should yield valid results for diameters as small as 0.1λ. Perhaps, the main problem may be the specular term

for small diameter targets. The eigenfunction solution circumvents this difficulty. The eigenfunction solution is, of course, not applicable to fuselages of general shape but the surface currents and charge densities for observation points on the plane of symmetry should not be significantly changed by minor changes in fuselage shape.

The techniques have all been developed for a symmetrically located point on relatively simple aircraft-like shapes. There are a number of extensions that can be incorporated in the computer solution. These include a) use of improved creeping wave coefficients b) computation of current and charge densities at points off the plane of symmetry c) computation of effect of electrically small perturbations to an electrically large aircraft such as short thin wings. There are several theoretical problems that need to be solved to reduce the frequency at which the surface charge and current densities can be computed. These are associated with the treatment of the fields diffracted by bodies with both a small (wing width) and a large dimension (wing length).

It can also be concluded for the high frequency range that the surface charge density is highest at the specular point or at the point at which normal incidence occurs and for principle radii greater than several tenths of a wavelength is approximately $2\hat{n} \times \bar{H}^i$. The surface charge density is quite approximately given by $\rho = 2\varepsilon_o \bar{E}^i \cdot \hat{n}$ in the visible region. This value may be off by the order of a factor of two for tangential incidence if there is a discontinuity in the surface along the ray path between the distant source and an observer on the surface and the actual charge density in the visible region will oscillate about the value given by the above equation.

REFERENCES

1. Keller, J.B., "Geometrical Theory of Diffraction," J. Opt. Soc. Am., Vol. 52, No. 2, February 1962, pp. 116-130.

2. Ryan, C.E., Jr., "A Geometrical Theory of Diffraction Analysis of the Radar Cross Section of a Sectionally Continuous Second-Degree Surface of Revolution," Report 2430-4, March 1968, ElectroScience Laboratory, Department of Electrical Engineering, The Ohio State University; prepared under Contract F-19628-67-C-0318 for Department of the Air Force, Laurence G. Hanscom Field, (AD 669 372)

3. Rudduck, R.C., "Application of Wedge Diffraction to Antenna Theory," Report 1691-13, 30 June 1965, ElectroScience Laboratory, Department of Electrical Engineering, The Ohio State University; prepared under Grant No. NsG-448 for National Aeronautics and Space Administration. Also published as NASA Report CR-372.

4. Ryan, C.E., Jr. and Rudduck, R.C., "A Wedge Diffraction Analysis of the Radiation Patterns of Parallel-Plate Waveguides," IEEE Trans. on Ants. and Prop., Vol. AP-16, No. 4, July 1968.

5. Burnside, W.D., Pelton, E.L., and Peters, L., Jr., "Analysis of Finite Parallel-Plate Waveguide Arrays," to be published as a Communication in IEEE Trans. on Ants. and Prop.

6. Sinclair, G., "The Patterns of Antennas Located Near Cylinders of Elliptic Cross Section," Proceedings of the I.R.E., June 1951, pp. 660-668.

7. Kouyoumjian, R.G., "Asymptotic High Frequency Methods," Proc. IEEE, Vol. 53, August 1965, pp. 864-876.

8. Kay, I. and Keller, J.B., "Asymptotic Evaluation of the Field at a Caustic," J. Appl. Physics, Vol. 25, July 1954, PP. 876-883.

9. Ludwig, D., Uniform Asymptotic Expansions at a Caustic, Comm. Pure Appl. Math., 19, 1966, pp. 215-250.

10. Pathak, P.H. and Kouyoumjian, R.G., "The Dyadic Diffraction Coefficient for a Perfectly-Conducting Wedge," Report 2183-4, 5 June 1970, ElectroScience Laboratory, Department of Electrical Engineering, The Ohio State University; prepared under Contract AF 19(628)-5929 for Electronics Systems Division, Air Force Systems Command. (AFCRL-69-0546)

11. Keller, J.B., "Diffraction by an Aperture," J. Appl. Physics, Vol. 28, April 1957, pp. 426-444.

12. Voltmer, D.V., "Diffraction by Doubly Curved Convex Surfaces," Ph.D. Dissertation, The Ohio State University, 1970.

13. Voltmer, D.V. and Kouyoumjian, R.G., "Higher Order Terms in the Diffraction by Curved Surfaces," paper to be published.

14. "On-Aircraft Antennas," Final Report 3188-3, January 1972, ElectroScience Laboratory, Department of Electrical Engineering, The Ohio State University; prepared under Contract N62269-71-C-0296 for Naval Air Development Center, Warminster, Pa.

15. Balanis, C.A. and Peters, L., Jr., "Analysis of Aperture Radiation from an Axially Slotted Circular Conducting Cylinder Using Geometrical Theory of Diffraction," IEEE Trans. on Ants. and Prop., Vol. AP-17, No. 1, January 1969, pp. 93, 97.

16. Balanis, C.A., "Radiation from Slots on Cylindrical Bodies Using Geometrical Theory of Diffraction and Creeping Wave Theory," Ph.D. Dissertation, ElectroScience Laboratory, Department of Electrical Engineering, The Ohio State University, 1969.

17. Balanis, C.A. and Peters, L., Jr., "Equatorial Plane Pattern of an Axial-TEM Slot on a Finite Size Ground Plane," IEEE Trans. on Ants. and Prop., Vol. AP-17, No. 3, May 1969, pp. 351-354.

18. Ryan, C.E., Jr., "Analysis of Radiation Patterns of Antennas on Finite Circular Cylinders and Conically-Capped Cylinders," Report 2805-2, 25 September 1970, ElectroScience Laboratory, Department of Electrical Engineering, The Ohio State University; prepared under Contract DAAA21-69-C-0535 for Department of The Army, Picatinny Arsenal, Dover, New Jersey.

19. Kouyoumjian, R.G., "A Note on the Caustic Distance Associated With a Curved Edge," paper to be published. (Also see Eq. (46) of this report).

20. Kouyoumjian, R.G. and Burnside, W.D., "Diffraction by a Cylinder-Tipped Half-Plane," IEEE Trans. on Ants. and Prop., Vol. AP-18, No. 3, May 1970, pp. 424-426.

21. Keller, J.B., "How Dark is the Shadow of a Round Ended Screen?," J. Appl. Physics., Vol. 30, September 1959, pp. 1452-1454.

22. Yu, C.L. and Burnside, W.D., "Elevation Plane Analysis of On-Aircraft Antennas," Report 3188-2, January 1972, ElectroScience Laboratory, Department of Electrical Engineering, The Ohio State University; prepared under Contract N62269-71-C-0296 for Naval Air Development Center.

23. Marhefka, R.J., "Roll Plane Analysis of On-Aircraft Antennas," Report 3188-1, December 1971, ElectroScience Laboratory, Department of Electrical Engineering, The Ohio State University; prepared under Contract N62269-71-C-0296 for Naval Air Development Center. Also presented as Thesis.

24. Sinclair, G., "The Patterns of Antennas Located Near Cylinders of Elliptical Cross Section," Proc. IRE, Vol. 39, No. 6, June 1951.

25. Carter, P.S., "Antenna Arrays Around Cylinders," Proc. IRE, Vol. 31, December 1943, pp. 671-693.

26. Van Bladel, J., Electromagnetic Fields, McGraw-Hill, 1964, pp. 376-379.

27. Ryan, C.E., Jr., op. cit.

28. Senior, T.B.A. and Desjardins, G.A., "Modified Biconical Antennas," Sensor and Simulation Notes No. 147.

29. Senior, T.B.A., "The Diffraction Matrix for a Discontinuity in Curvature," Sensor and Simulation Notes No. 132.

30. Pathak, P.H. and Kouyoumjian, R.G., "The Dyadic Diffraction Coefficient for a Perfectly-Conducting Edge Structure," presented at the fall 1971 URSI Meeting at Los Angeles, California.

31. Kouyoumjian, R.G. and Pathak, P.H., "The Radiation from Apertures in Curved Surfaces," presented at the Fall 1971 URSI Meeting at Los Angeles, California.

32. Kline, M. and Kay, I., Electromagnetic Theory and Geometrical Optics, New York, Interscience 1965.